

Nonlinear dynamics and stability analysis of locally-active Mott memristors using a physics-based compact model

Wei Yi

HRL Laboratories, LLC., 3011 Malibu Canyon Rd, CA 90265, United States of America

E-mail: wyi@hrl.com

September 2023 (Revised June 2024)

Abstract. Locally-active memristors are a class of emerging nonlinear dynamic circuit elements that hold promise for scalable yet biomimetic neuromorphic circuits. Starting from a physics-based compact model, we performed small-signal linearization analyses and applied Chua's local activity theory to a one-dimensional locally-active vanadium dioxide Mott memristor based on an insulator-to-metal phase transition. This approach allows a connection between the dynamical behaviors of a Mott memristor and its physical device parameters as well as a complete mapping of the locally passive and edge of chaos domains in the frequency and current operating parameter space, which could guide materials and device development for neuromorphic circuit applications. We also examined the applicability of local analyses on a second-order relaxation oscillator circuit that consists of a voltage-biased vanadium dioxide memristor coupled to a parallel reactive capacitor element and a series resistor. We show that global nonlinear techniques, including nullclines and phase portraits, provide insights on instabilities and persistent oscillations near non-hyperbolic fixed points, such as a supercritical Hopf-like bifurcation from an unstable spiral to a stable limit cycle, with each of the three circuit parameters acting as a bifurcation parameter. The abruptive growth in the limit cycle resembles the Canard explosion phenomenon in systems exhibiting relaxation oscillations. Finally, we show that experimental limit cycle oscillations in a vanadium dioxide nano-device relaxation oscillator match well with SPICE simulations built upon the compact model.

Keywords: local activity, edge of chaos, memristor, vanadium dioxide, Mott transition, Hopf bifurcation, limit cycle

1. Introduction

Recent years have witnessed a surge of interest in exploiting nonlinear dynamical phenomena in emerging devices for novel circuit applications such as neuromorphic computing. A subject that has been intensively studied is one-port (two-terminal)

passive memristors that exhibit a pinched hysteresis which always passes through the origin in their current-voltage (I–V) loci, thus having a non-volatile memory effect [1,2]. Passive memristors promise a scalable and energy-efficient venue to emulate biological synapses and realize computationally efficient neuromorphic learning rules [3–6].

Although a canonical memristor is a passive circuit element, any one-port device that exhibits a pinched hysteresis is an extended memristor [7], which includes a class of one-port devices that exhibit a non-monotonicity in their experimental quasi-direct current (quasi-DC) I–V curves — a negative differential resistance (NDR). These devices typically exhibit a pronounced I–V hysteresis when driven by a voltage stimulus, however the hysteresis *collapses* at a finite voltage, therefore they only have a transient (volatile) memory effect. Importantly, these passive one-port devices are *locally active* within the NDR region and thus offers a gain of alternating-current (AC) signals — a must-have capability for information processing and communication that has been dominated by transistors. Figure 1 compares typical quasi-DC I–V curves measured from a passive memristor and a locally-active memristor. Such a measurement varies V or I stimulus slowly and measures time-averaged device responses, which could capture the resistance states before and after a resistance switching event (see arrows), but not the ultrafast switching dynamics that could occur within femtoseconds. Figure 1(a) shows a bipolar tantalum oxide ($\text{TaO}_y\text{-Ta}_2\text{O}_5$) passive memristor which switches from a low-resistance state (LRS) to a high-resistance state (HRS) if a sufficiently-large positive voltage is applied (Reset), and switches from the HRS back to the LRS if a sufficiently-large negative voltage is applied (Set). Both Reset and Set operations are nonvolatile, i.e., resistance changes are retained after powered off. In contrast, figure 1(b) shows a unipolar vanadium dioxide (VO_2) locally-active memristor, which abruptly switches from a HRS to a LRS if a sufficiently-large voltage is applied, regardless of its polarity. As voltage is reduced below a smaller threshold level, the device switches from the LRS back to the HRS — resistance changes are volatile and get lost after powered off. Be mindful that the exemplary characteristics in figure 1 are by no means exhaustive. Passive memristors can have either bipolar or unipolar non-volatile resistance switching behaviors, determined by intertwined ionic and electronic transport mechanisms within the nanoscale device volume [8,9]. They may also exhibit a fading memory effect with its asymptotic behavior solely determined by the state dynamics irrespective of the initial condition [10,11].

We now turn our attention to those one-port devices that possess the peculiar I–V characteristics in figure 1(b). In fact, on-port devices with such switching characteristics have long been studied and put into engineering practice. They have been made out of many materials based on a variety of operating mechanisms. A familiar category is electro-thermal threshold switches such as ovonic threshold switches (OTS), which show rapid changes in resistance due to nonlinear interactions among local temperature, metastable structural change, and electrical conductivity [13,14]. Being a one-port device, locally-active memristors (LAMs) and passive memristors share the same level of $4F^2$ (F: half pitch in lithography) scalability in a crossbar device geometry [15],

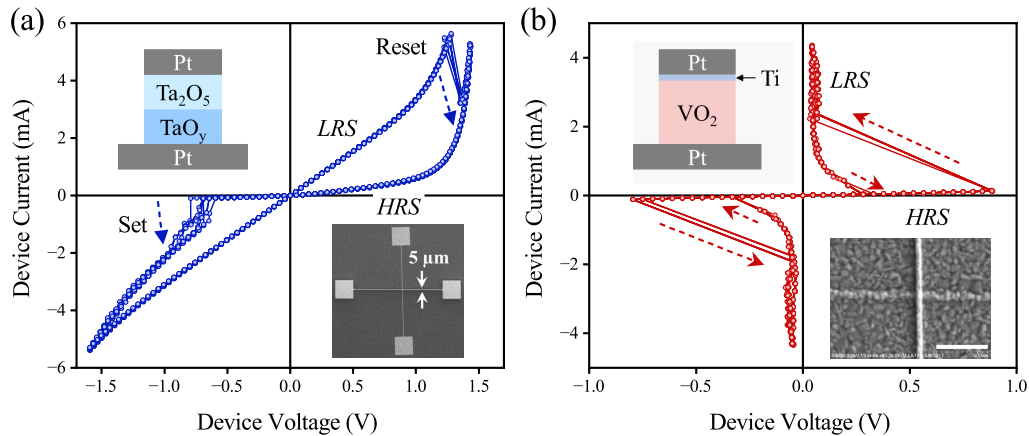


Figure 1: Experimental quasi-DC I–V curves for (a) a $\text{TaO}_y\text{-Ta}_2\text{O}_5$ bilayer passive memristor, and (b) a VO_2 locally-active memristor, fabricated and characterized by HRL Laboratories, LLC. Resistance switching events are indicated by dashed arrows. Insets of (a): layer structure and optical image of the $5 \times 5 \mu\text{m}^2$ $\text{TaO}_y\text{-Ta}_2\text{O}_5$ ($y < 2$) crossbar device. Insets of (b): layer structure and scanning electron micrograph of the $50 \times 50 \text{ nm}^2$ VO_2 nano-crossbar device (scale bar: 500 nm). Memristor crossbars are tested in a four-terminal Kelvin connection (see [22] for details). The external voltage is swept at $\sim 1 \text{ V/s}$ rate in the sequence of $0 \rightarrow +V_p \rightarrow 0 \rightarrow -V_n \rightarrow 0$ (repeated 10 times). $V_p(V_n) = 2.5(2) \text{ V}$ in (a) and $V_{p,n} = 1.45 \text{ V}$ in (b). The metal electrodes contribute a series resistance of 600–800 Ω .

resolving the trade-off between scalability and biological fidelity.

LAMs may be generally classified into two types, current-controlled (S-type) and voltage-controlled (λ -type), where the letter “S” and “ λ ” resembles the characteristic shape of NDR in the I–V curve plotted with voltage as the x axis [16]. S-type LAMs are “normally-off” devices with a HRS when powered off. λ -type LAMs such as resonant tunneling diodes are “normally-on” devices with a LRS when powered off [17]. Therefore S-type LAMs are superior choices than λ -type LAMs with respect to the standby power consumption. Hereafter we focus our discussions on current-controlled LAMs.

A particularly interesting class of current-controlled LAMs is based on the insulator-to-metal phase transition (IMT) phenomena in strongly correlated materials that arise from a coupling between structural distortions (Peierls transition) and electronic instabilities (Mott transition) [18]. They possess several attractive features for circuit applications, such as ultralow (femtojoule) switching energy [19], ultra-fast (tens of femtosecond) switching speed [20], and electroforming-free operations [21]. We term all these IMT based LAMs “Mott memristors” without discerning the subtle differences in their phase transition mechanisms. Vanadium dioxide (VO_2) and niobium dioxide (NbO_2) are two intensively-studied Mott memristor materials among many others [18].

For neuromorphic computing applications, circuits of self-excited oscillators and spiking neuron emulators have been built with one or more LAMs that are coupled with reactive elements (capacitors) [23–27]. An illustrative example is a scalable spiking neuron, which constitutes two oppositely energized (“polarized” in neuroscience

glossary) LAMs to mimic the voltage-gated potassium and sodium cell membrane ion channels. Coupled with parallel membrane capacitors and series load resistors, the composite circuit emulates a single-compartment nerve cell initiating all-or-nothing action potentials upon a suprathreshold stimulus [21, 28], or acting as a delayed buffer that allows bidirectional distortion-free propagation of action potentials if daisy chained [29, 30]. Such a circuit topology bears some resemblance to a biologically-plausible Hodgkin-Huxley (HH) axon model [31], as well as the early 1960s proposals of “neuristor” axons utilizing non-scalable components such as inductors [32–34]. Experimental spiking neurons built with VO₂ Mott memristors showed two dozens of biological neuronal temporal dynamics, including all three classes of neuronal excitability [21]. Arguably, LAM-based neurons and passive memristor-based synapses form a self-sufficient basis to construct a transistorless neural network [22].

Despite the wealth of experimental demonstrations, predictive modeling and analysis of LAM elements and circuits is nontrivial and remains a handicap for technology development. The difficulties are partially by virtue of fundamental mathematical challenges about nonlinear differential systems. One illustrious example is the second part of Hilbert’s 16th problem that questions whether there exists a finite upper bound for the number of limit cycles of planar polynomial differential systems. It remains unsolved today even for quadratic polynomials (degree $n = 2$) [35]. Qualitative local analysis, on the contrary, are facilitated by small-signal linearization techniques, which allow linear analysis to be applied to a nonlinear system near a *hyperbolic* fixed point with all eigenvalues of the linearization having non-zero real parts [36]. A key theoretical contribution made by Chua is the local activity (LA) theorem, which provides a rigorous mathematical definition of the LA as a necessary prerequisite for the emergence of complexity in nonlinear systems [37]. Moreover, Chua provided a set of explicit and computable criteria in the parameter space, that allows identifying the *edge of chaos* (EOC) region that is both locally active and locally stable, where most of the complexity phenomena emerge.

Mathematically rigorous but unphysical toy models of nonlinear dynamical elements were frequently used in the LA analysis procedure [38, 39]. For engineering practice, such toy models could not offer a link between circuit or network level dynamics and measurable physical properties of constituent components. A recent review thoroughly elaborated the importance of applying appropriate device physics into mathematical memristor framework, and defining physically relevant model parameters to control the circuit dynamic behavior [40].

The main objective of this manuscript is to apply relevant theoretical techniques to understand the dynamics and stability of nonlinear circuits that involve locally-active Mott memristors, and to map the conditions for the LA regime within the design parameter space [41, 42]. These theoretical techniques include essential local analysis methods such as the small-signal linearization and the LA theorem, and global techniques such as the nullclines and phase portraits. For engineering relevance, we base our analyses on an analytical one-dimensional (1D) Mott memristor compact

model that is built on the laws of thermodynamics and only contains physically relevant device parameters. The model was developed by Pickett and Williams for NbO₂ Mott memristors [43]. Previously we have verified that it is also applicable to VO₂ Mott memristors after replacing the material properties [44, 45], and our SPICE simulations based on this model faithfully reproduced most of the measured neuronal dynamics in neuron circuits built with VO₂ memristors [21]. Here, we demonstrate that this physics-based compact model is mathematically tractable for applying the local and global analysis techniques, having closed-form expressions for all the important quantities involved in the analyses. It enables a connection between the system dynamics and component physical parameters to guide circuit designs and process development. The algorithmic analysis procedure we present using a VO₂ Mott memristor model is general in nature and suitable for analyzing other Mott memristor materials. Qualitatively, the predictions on the dynamics and stability by the present work are similar to those made by compact models based on different choices of state variable and kinetic function [40].

We focus on theoretical analyses and only included a cursory comparison between the model simulated and experimental characteristics of a VO₂ nano-device relaxation oscillator near the end. More detailed comparisons in the context of VO₂ Mott memristor neurons can be found in supplementary materials of [21]. It is understood that the compact model presented here has some simplifications and limitations. It is a nontrivial task to construct a computationally-efficient compact model for locally-active memristors with an appropriate balance between the dynamical fidelity and the computational complexity of solving the model equations. This is especially important for digital computer simulations of a scaled network that contains many instances of memristor elements, which could be costly in time and energy consumption.

The manuscript is organized as follows. After the introduction section, the first three sections (Section 2 – 4) are dedicated to analyses of an isolated 1D Mott memristor. First (Section 2), we introduce the physics-based compact model and analyze the stability of an isolated 1D Mott memristor by examining its power-off plot and dynamic route map under constant input currents or voltages. This exercise confirms that the metallic state of a Mott memristor is unstable without power and is asymptotically stable with a finite input current. It also reveals that varying voltage as the bifurcation parameter leads to a supercritical saddle-node bifurcation. Then (Section 3) we solve its locus of steady states (fixed points) in the three-dimensional (3D) state space and their two-dimensional (2D) projections. Note that we use both fixed point and steady state for the same concept in an interchangeable manner, but avoid the term equilibrium unless the input is zero. See subsection 2.2 for an elaboration on this topic.

In Section 4, we apply local analysis techniques on an isolated Mott memristor, including linearization and small-signal analysis, pole-zero diagram, Chua’s LA theorem, and frequency response. Its complex-domain (s -domain) equivalent circuit derived by Laplace transform contains three virtual elements — a negative nonlinear capacitor in parallel with a negative nonlinear resistor, both in series with a positive nonlinear resistor. The negative s -domain capacitance gives rise to an apparent inductive response,

similar to the memristive models of potassium and sodium ion channels [31]. We found that an isolated Mott memristor about a fixed point dwells either in the locally passive (LP) or the EOC region. The EOC region coincides with the NDR region in its steady-state or DC I–V locus. Brown et al. [40] elaborated that for an extended electro-thermal memristor, the coincidence between NDR and EOC or LA regions is not guaranteed. Therefore NDR shall not be used as a sole signature for EOC. In our case, the crossover between the LP and EOC regions also manifests itself in the small-signal frequency response, which shows a sign reversal in the real part of the impedance (complexity) function $\text{Re}Z(s; Q)$ as predicted by the fourth LA criterion. In the frequency domain, an isolated Mott memristor is equivalent to a positive inductor in series with a resistor that is positive in the LP region and negative in the EOC domain. We derived the parametric Nyquist plot of the LP \leftrightarrow EOC crossover at a single current level, then extended it to a 2D color scale map of $\text{Re}Z(s; Q)$ to visualize the LP and EOC regions in the parameter space spanned by frequency and current, which is effectively a phase diagram for complexity. We also examined the scaling trend of the EOC region versus the device size, which shows that the VO_2 conduction channel radius is the relevant dimension for device miniaturization to enhance the EOC frequency regime.

Although an EOC region exists in an isolated 1D Mott memristor, the topological constraint limits the dynamics it can possess, making it impossible to exhibit persistent oscillations. In the last two sections (Section 5 – 6), we lift the topological constraint for an isolated 1D Mott memristor by coupling it to one or more reactive elements, raising the system dimensionality and the dynamical complexity. For simplicity, we choose a DC voltage (V_{dc}) biased Pearson–Anson relaxation oscillator formed by a Mott memristor coupled with a parallel capacitor C_p and a series resistor R_s as an example 2D nonlinear system for our analysis [46]. The same analysis procedure can be applied to higher-dimensional systems, such as spiking neuron circuits consisting of two or more Mott memristors coupled with passive and reactive elements.

In Section 5 we first apply local linearization techniques on this example system, including the element combination approach, the Jacobian matrix method, and the trace-determinant plane classification, to study stability and qualitative behaviors about its hyperbolic fixed points. The element combination approach treats a Mott memristor in parallel with a capacitor as a composite second-order nonlinear element. The small-signal transfer function of the dimension-reduced system has a pair of complex conjugate poles. We derived the Nyquist plot and a 2D phase diagram of the system’s poles visualizing the LP and EOC regions in the circuit parameter space. These results are corroborated by the the trace-determinant plane analysis of the Jacobian linearized 2D system, which reveals a stability-change bifurcation as the parametric (trace, determinant) locus crosses the zero-trace axis as one of the three circuit parameters is varied (R_s , C_p and V_{dc}). However, analysis of stability behavior about a non-hyperbolic center requires additional theoretical tools, since the Hartman-Grobman theorem is not applicable with the loss of hyperbolicity [47, 48].

Finally, in Section 6 we apply several global methods, such as the nullclines and

numerical phase portrait analyses, to understand qualitative behaviors about the non-hyperbolic centers in this example 2D nonlinear system. We found that each of the three circuit parameters (R_s , C_p and V_{dc}) acts as a bifurcation parameter that switches the stability of a fixed point as the parametric (trace, determinant) locus crosses a center. We verified that there exists a supercritical 2D Hopf-like bifurcation, i.e., the creation of a stable limit cycle encircling an unstable spiral as the fixed point switches its stability from stable to unstable. We also noticed that the limit cycle appears abruptly over an extremely thin bifurcation parameter interval, a phenomenon known as ‘‘Canard explosion’’ for relaxation oscillations in chemical and biological systems [50, 51]. This is a prominent distinction than the classical Hopf bifurcation, which predicts a gradual growth proportional to the square root of the bifurcation parameter. Each bifurcation parameter has a different bifurcation growth characteristics. We end the section with a comparison between experimental limit cycle characteristics of a VO_2 relaxation oscillator and SPICE simulations based on the Mott memristor model, showing excellent agreements between them.

We conclude the manuscript with brief remarks about the application implications of locally-active memristors and scalable neuromorphic dynamic neurons with high degree of complexity.

2. One-dimensional locally-active Mott memristor

2.1. The physics-based analytical compact model

The physics-based compact model for a 1D (one state variable) locally-active Mott memristor is biphasic in nature [43]. It assumes that once an IMT is triggered by Joule self-heating beyond a threshold level, metallic and insulating phases coexist in a constant-volume conduction channel defined by the top and bottom electrodes. For mathematical simplification, the conduction channel has an axial symmetry with a constant radius r_{ch} along its length. An experimental crossbar device may have a square or rectangular cross section defined by its top and bottom electrodes. The insulating phase has much lower thermal and electrical conductivity than those of the metallic phase, therefore the core region turns metallic first and its radius r_{met} grows as Joule heating increases. In analogy to the case of an ice-water mixture, the maximum temperature within the metallic core is capped to the transition temperature T_c until the whole conduction channel turns metallic. The minimum temperature at the outer edge of the insulator shell is clamped to the ambient temperature T_0 . The temperature rise required for IMT to occur is defined as $\Delta T = T_c - T_0$. With these assumptions, a radial temperature profile bounded between T_0 and T_c is established across the insulating shell surrounding the metallic core. The schematics of this biphasic thermal model is shown in figure 2.

The state variable $x \triangleq r_{met}/r_{ch}$ is modeled as the dimensionless volumetric fraction of metallic phase in the conduction channel and is bounded between 0 and 1. The model

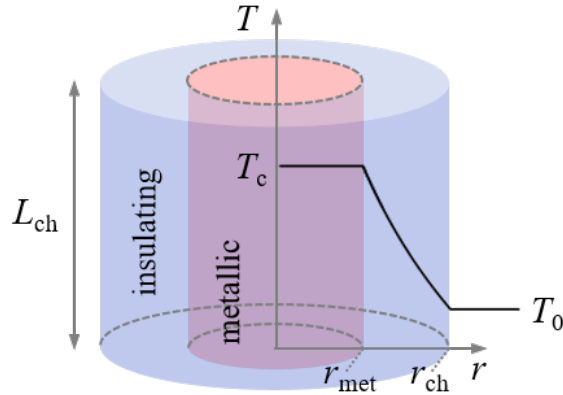


Figure 2: Schematics of the biphasic thermal model for a Mott memristor that undergoes an insulator-to-metal transition, illustrating a cylindrical conduction channel with a metallic-phase core surrounded by an insulating-phase shell. The model assumes that the metallic core is clamped to the transition temperature T_c , and the outer edge of the conduction channel is clamped to the ambient temperature T_0 . The black solid line shows a calculated radial temperature profile. The top and bottom electrodes are not shown for clarity.

derives that the temperature at a specific radius $T(r)$ is a nonlinear function of x of the form $T(r) = T_0 + \Delta T \ln(\frac{r}{r_{ch}}) / \ln(x)$, $r_{met} \leq r \leq r_{ch}$.

Another assumption that the model makes for mathematical simplification is to ignore the axial heat exchanges with the electrodes and the associated temperature gradients near the top and bottom interfaces. Moreover, thermal and electrical conductivity of the insulating shell are approximated as constants regardless of the radial temperature gradient across it. This approximation holds true if neither of them varies significantly as temperature rises from T_0 to T_c . This is probably the case for VO_2 with a small ΔT ($T_c \approx 340$ K, $\Delta T \approx 43$ K) [45], but becomes questionable for NbO_2 with a very large ΔT ($T_c \approx 1080$ K, $\Delta T \approx 784$ K) [49].

The compact model consists of two coupled equations that satisfy the definition of a 1D extended memristor [7]: a state-dependent instantaneous relationship between voltage and current in the form of Ohm's law (state-dependent Ohm's law), and a first-order ordinary differential equation (ODE) that determines the dynamics of the single state variable x (state equation). The kinetic function that accounts for the state dynamics is a function of both the state variable x and the input variable (voltage v or current i). A Mott memristor therefore is a dynamical system — a system whose state at a future time depends deterministically on its present state and a physical law that governs its evolution over time.

Since Joule self-heating depends on the passage of current, a Mott memristor is a current-controlled memristor, and current i instead of voltage v is the appropriate input

variable. The model equations take the following form

$$v(x, i) = R_{\text{ch}}(x)i \quad (1)$$

$$\frac{dx}{dt} \triangleq f_x(x, i) = \frac{i^2 R_{\text{ch}}(x) - \Gamma_{\text{th}}(x)\Delta T}{H'(x)} \quad (2)$$

The single state variable $x \in (0, 1)$ is a dimensionless quantity within the bounded open interval between 0 and 1. $f_x(x, i)$ is the kinetic function for the state variable x . The derivation of $f_x(x, i)$ is nontrivial and is the main task of building the compact model. For Mott memristors and generally electro-thermal memristors, $f_x(x, i)$ is derived from the first law of thermodynamics, which states that the change in the total enthalpy of a system ΔH equals the net heat flow q_p into it at constant pressure: $\Delta H = q_p$. Therefore, their time derivatives are equal as well: $\frac{d\Delta H}{dt} = \frac{dq_p}{dt}$. This basic law forms the theoretical basis to interpret electro-thermal memristors wherein the local temperature change plays a key role. It is worth pointing out that since there is no explicit dependence on time t in $f_x(x, i)$, this is an *autonomous* system.

To simplify the expression for $f_x(x, i)$, three nonlinear auxiliary functions are defined: the state-dependent memristance function $R_{\text{ch}}(x)$, the state-dependent thermal conductance function $\Gamma_{\text{th}}(x)$, and $H'(x) \triangleq \frac{d\Delta H}{dx}$ is defined as the derivative of the total enthalpy change ΔH with regard to the state variable x

$$R_{\text{ch}}(x) = \frac{1}{A(1 + Bx^2)} \quad (3)$$

$$\Gamma_{\text{th}}(x)\Delta T = -\frac{C}{\ln x} \quad (4)$$

$$H'(x) \triangleq \frac{d\Delta H}{dx} = D \left(\frac{1 - x^2 + 2x^2 \ln x}{2x(\ln x)^2} + Ex \right) \quad (5)$$

where $A = \frac{\pi r_{\text{ch}}^2}{\rho_{\text{ins}} L_{\text{ch}}}$, $B = \frac{\rho_{\text{ins}}}{\rho_{\text{met}}} - 1$, $C = 2\pi L_{\text{ch}} \kappa \Delta T$, $D = \pi L_{\text{ch}} r_{\text{ch}}^2 c_p \Delta T$, and $E = \frac{2\Delta h_{\text{tr}}}{c_p \Delta T}$ are constant coefficients whose values are determined by physical model parameters, including material properties and device geometry. Table 1 lists values of these physical model parameters for the case of VO₂ material. The radius and length of the memristor conduction channel are device-dependent parameters and can be determined experimentally by the device geometry. Rest of the model parameters listed in Table 1 are electronic, thermal and phase transition properties of VO₂ material reported in literature [44,45]. Optimization of these material property-dependent parameters can be achieved by a calibration procedure with well-devised characterizations of VO₂ devices and least-square data fitting [52], but is beyond the scope of this work.

Table 2 lists values of model coefficients A , B , C , D , and E for three arbitrarily-chosen VO₂ device sizes — the radius r_{ch} and length L_{ch} of the conduction channel. Coefficients B and E are dimensionless and device size-independent. Without loss of generality, these three device sizes are used throughout this manuscript to illustrate the scaling trend of a calculated quantity as the device size varies. If not mentioned explicitly, hereafter the modeled VO₂ device is the medium-sized one in table 2 with $r_{\text{ch}} = 36$ nm and $L_{\text{ch}} = 50$ nm, and is referred to as the *midsized* VO₂ Mott memristor

Table 1: Material properties and device parameters for a VO₂ Mott memristor model.

Model Property	Symbol	Value	Unit	Reference
Volumetric heat capacity	c_p	3.30×10^6	$\text{Jm}^{-3}\text{K}^{-1}$	[44]
Volumetric enthalpy change of IMT	Δh_{tr}	2.35×10^8	Jm^{-3}	[45]
Thermal conductivity of insulating phase	κ	3.5	$\text{Wm}^{-1}\text{K}^{-1}$	[44]
Electrical resistivity of metallic phase	ρ_{met}	3.00×10^{-6}	Ωm	[44, 45]
Electrical resistivity of insulating phase	ρ_{ins}	1.00×10^{-2}	Ωm	[45]
Temperature rise of IMT	ΔT	43	K	[45]
Radius of the conduction channel	r_{ch}	3.60×10^{-8}	m	Experimental
Length of the conduction channel	L_{ch}	5.00×10^{-8}	m	Experimental

Table 2: Values of model coefficients for three VO₂ device sizes.

Coefficient	Formula	Unit	$r_{\text{ch}} = 10 \text{ nm},$	$r_{\text{ch}} = 36 \text{ nm},$	$r_{\text{ch}} = 56 \text{ nm},$
			$L_{\text{ch}} = 10 \text{ nm}$	$L_{\text{ch}} = 50 \text{ nm}$	$L_{\text{ch}} = 100 \text{ nm}$
A	$\frac{\pi r_{\text{ch}}^2}{\rho_{\text{ins}} L_{\text{ch}}}$	Mho	3.14159×10^{-6}	8.14301×10^{-6}	9.85203×10^{-6}
B	$\frac{\rho_{\text{ins}}}{\rho_{\text{met}}} - 1$	Unitless	3332.3	3332.3	3332.3
C	$2\pi L_{\text{ch}} \kappa \Delta T$	Watt	9.45619×10^{-6}	4.7281×10^{-5}	9.45619×10^{-5}
D	$\pi L_{\text{ch}} r_{\text{ch}}^2 c_p \Delta T$	Joule	4.45792×10^{-16}	2.88873×10^{-14}	1.398×10^{-13}
E	$\frac{2\Delta h_{\text{tr}}}{c_p \Delta T}$	Unitless	3.31219	3.31219	3.31219

or midsize VO₂ device.

A more general approach for physical modeling of an electro-thermal memristor treats the internal temperature as the sole state variable [40]. The kinetic function is derived from Newton's law of cooling, which connects between the net heating power and a time-varying device internal temperature through a temperature-dependent thermal capacitance. There is clearly a benefit of adopting a universal state variable and a generalized formula of the kinetic function, albeit the temperature dependence of thermal capacitance is unknown and requires a model fitting with experimental characterizations, such as the temperature dependence of self-excited oscillation frequency in a memristor-based relaxation oscillator [52]. It is curious that both approaches can reach the same qualitative predictions about the system dynamics, despite the differences in the model assumptions, state variable, and kinetic function.

2.2. Stability analyses

We start the stability analyses by looking at an isolated or uncoupled Mott memristor. The first step is to examine the stability of solutions for equation (2) by treating input current as a parameter with a zero or nonzero constant value, and plotting the kinetic function $f_x(x, i)$ as a function of the state variable x . If a solution $f_x(x, i) = 0$ exists at a point x_Q , it is called a fixed point [53]. This is because the state variable $x(t)$ with an initial condition $x(0) = x_Q$ remains unchanged at any future time, i.e., $x(t) = x_Q$ for $t > 0$. Literature from different disciplines have adopted a variety of terminologies for the same concept, including stationary point, invariant point, equilibrium point, critical point, singular point and steady state point. These terms are generally exchangeable, but may be confusing if not carefully chosen. Especially the use of equilibrium point may cause misinterpretation by physical scientists for reasons we will elaborate below.

A system at equilibrium remains stable over time and does not require a net flow of energy or work to maintain that condition. A steady state also has stable internal states that remain unchanged over time. However, it requires a continuous energy input or work from the external environment to remain in a constant state. A memristor that has stable internal states while having a *finite* current flowing through it is at a nonequilibrium steady state rather than at an equilibrium, since there is a net heat transfer q_p into the memristor. In this manuscript, we mainly use the term of fixed point because of its prevalence in mathematics. Steady state will also be used as a descriptive term when it facilitates interpretation. For example, steady-state resistance is a preferred term than fixed-point resistance.

For a current-controlled memristor, current is the appropriate input variable for stability analysis. However, one can still treat voltage v as an input and run the same type of analysis. Interestingly, doing so would result in a bifurcation – a qualitative change in the solution of a nonlinear system incurred by a small change in a parameter, such as creation or annihilation of fixed points, or a change in their stability.

2.2.1. Power-off plot The question about whether or not a memristor is non-volatile can be answered by looking at the power-off plot (POP) [54]. For a current-controlled memristor, its POP is the locus of the kinetic function $f_x(x, i)$ as a function of the state variable x at zero input current, i.e., the locus of $f_x(x, 0)$ vs. x .

Setting input current to be zero in equation (2), one get

$$f_x(x, 0) = \frac{-\Gamma_{\text{th}}(x)\Delta T}{H'(x)} = \frac{2Cx \ln x}{D[1 - x^2 + 2x^2 \ln x + 2E(x \ln x)^2]} \quad (6)$$

If $f_x(x, 0)$ has an intersection with the x -axis, then the intersection is an equilibrium point x_Q . The memristor state $x(t)$ with an initial state $x(0) = x_Q$ remains unchanged at any future time, i.e., $x(t) = x_Q$ for any $t > 0$.

Figure 3 shows that for a Mott memristor at zero input current, $f_x(x, 0)$ remains negative for any state variable $x \in (0, 1)$. It is plausible since if there were a finite fraction of the conduction channel in metallic phase at the beginning, it is unstable without the

presence of Joule heating, and will always vanish over time. The memory effect in a Mott memristor is therefore transient or volatile in nature, and will be lost given long enough time after the removal of electrical power. Figure 3 inset shows that the negative rate of change in x increases dramatically as x approaches 1.0 asymptotically. The calculations are performed using VO_2 model parameters, but this conclusion is generally applicable to other Mott memristor materials.

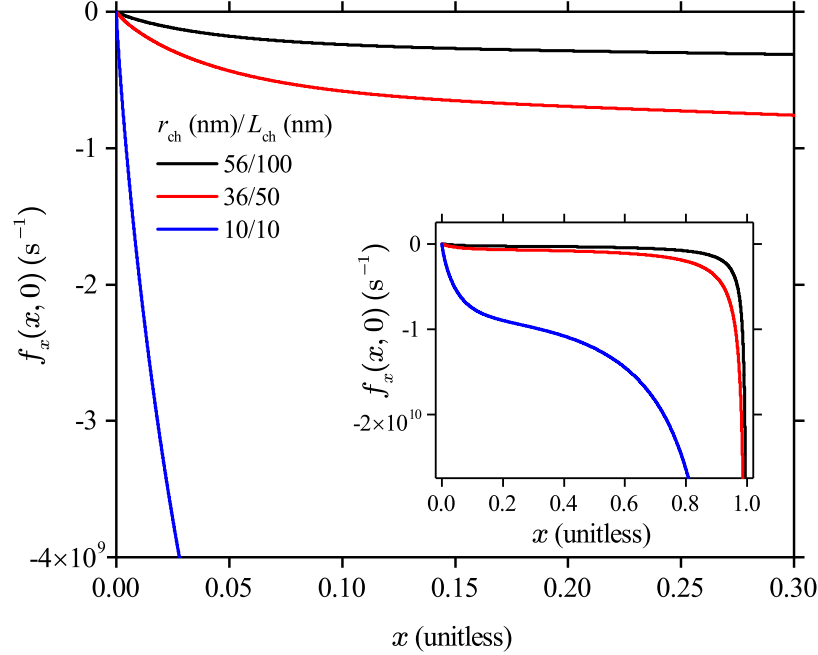


Figure 3: Analytically calculated power-off plots $f_x(x, 0)$ vs. x for three different-sized VO_2 Mott memristors (as labeled) in the small x region ($0 < x < 0.3$). Inset shows the same power-off plots for a much wider range of $0 < x < 1$.

2.2.2. Dynamic route map at constant input current If input current is fixed at a finite constant level $i_0 \neq 0$, one can plot the dynamic route (DR) — the locus of the kinetic function $f_x(x, i_0)$ as a function of the state variable x at a constant input current i_0 [55]. A set of dynamic routes parameterized by input current (or voltage for a voltage-controlled memristor) is called a dynamic route map (DRM) [56]. Rewriting $f_x(x, i)$ in equation (2) by replacing the auxiliary functions $R_{\text{ch}}(x)$, $\Gamma_{\text{th}}(x)$ and $H'(x)$ with their explicit expressions, one get

$$f_x(x, i_0) = \frac{\frac{2x(\ln x)^2}{A(1+Bx^2)}i_0^2 + 2Cx \ln x}{D[1 - x^2 + 2x^2 \ln x + 2E(x \ln x)^2]} \quad (7)$$

As figure 4(a) shows, even a tiny input current of a few μA creates a positive slope for the DR locus of the midsize VO_2 device, flipping the fourth-quadrant POP locus up into the first quadrant once a finite current is supplied. The slope of DR then levels off and becomes negative again as x further increases. Consequently, a constant-current

DR locus always intersects the x -axis at a single fixed point x_Q . This is confirmed by figure 4(b) which shows the DRM loci with a much wider range of current from 0 to 3 mA.

The theory of nonlinear dynamics tells us that the fixed point x_Q is *asymptotically stable* because the solution $x(t)$ starting from any initial state $x(0) \neq x_Q$ approaches the fixed point x_Q as $t \rightarrow \infty$. For $x < x_Q$, $dx/dt > 0$. For $x > x_Q$, $dx/dt < 0$. The arrowhead pointing to the right indicates that the solution $x(t)$ starting from any initial state $x(0) \neq x_Q$ on the DR above the x -axis must move to the right of $x(0)$, because $dx/dt > 0$ for $t > 0$, as long as $x(t)$ lies above the x -axis. Conversely, the arrowhead pointing to the left indicates that the solution $x(t)$ starting from any initial state $x(0) \neq x_Q$ below the x -axis on the DR must move to the left of $x(0)$, because $dx/dt < 0$ for $t > 0$, as long as $x(t)$ lies below the x -axis.

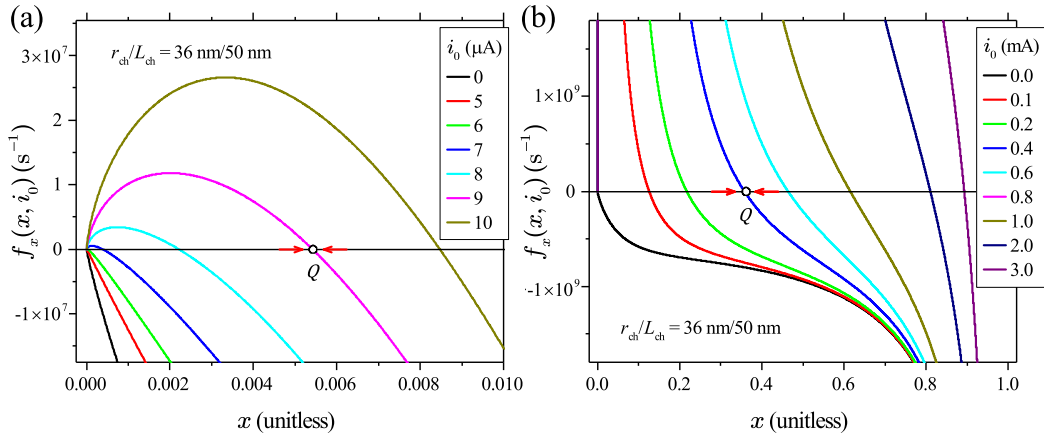


Figure 4: Analytically calculated dynamic route map of $f_x(x, i_0)$ at constant input current levels for the midsize VO₂ Mott memristor, plotted with (a) a narrow range of i_0 from 0 to 10 μA , and (b) a wide range of i_0 from 0 to 3 mA. The open circle in (a) and (b) highlights a fixed point Q where the $f_x(x, i_0)$ locus intersects the x -axis. Arrowheads show the direction of move for a solution $x(t)$ starting from an initial state located close to Q .

2.2.3. Dynamic route map at constant input voltage: saddle-node bifurcation Although a Mott memristor is a current-controlled device, it is interesting to look at the state dynamics for the case that a constant finite input voltage is applied across it. Replacing current i by voltage v in equation (2), the kinetic function can be rewritten as a function of x and v . At a constant input voltage v_0 , it takes the form

$$f_x(x, v_0) = \frac{1}{H'(x)} \left(\frac{v_0^2}{R_{ch}(x)} - \Gamma_{th}(x)\Delta T \right) = \frac{2Ax(\ln x)^2(1 + Bx^2)v_0^2 + 2Cx \ln x}{D[1 - x^2 + 2x^2 \ln x + 2E(x \ln x)^2]} \quad (8)$$

Figure 5(a) shows the DRM loci of $f_x(x, v_0)$ vs. x at constant v_0 levels from 0 to 1.2 V at 0.1 V interval for the midsize VO₂ device. Figure 5(b) is a zoomed view which reveals three behaviorally distinctive regions determined by the amplitude of v_0 . At a very

small $v_0 < 0.0973$ V, the DR locus stays in the fourth quadrant and does not intersect with the x -axis. In other words, $f_x(x, v_0) < 0$ is satisfied at any $x \in (0, 1)$. It indicates that at such small input voltages, even if the initial condition is a metallic phase, a Mott memristor always return to the insulating state after a finite time. Physically speaking, the Joule heating level at such small voltages is too small to sustain a metallic filament at the IMT critical temperature against the heat loss. At $v_0 = 0.0973$ V, the DR locus becomes tangent to the x -axis with only one intersection point close to $x_0 = 0.606$. At a $v_0 > 0.0973$ V, the DR locus “swings” from the fourth quadrant to the first quadrant, then it swings back to the fourth quadrant, intersecting the x -axis at two distinctive points to the left and right of x_0 .

For a 1D nonlinear ODE system, a saddle-node (tangent) bifurcation is the generic bifurcation in which the number of fixed points changes as some parameter is varied. If additional conditions are met, a transcritical or pitchfork bifurcation may occur. A simple example of a saddle-node bifurcation is $dx/dt = \mu \pm x^2$, where μ is the bifurcation parameter and the sign determines if it is supercritical ($\mu - x^2$) or subcritical ($\mu + x^2$). For the supercritical case, as μ increases through $\mu_0 = 0$ (the bifurcation value), the number of fixed points changes from zero to one then two. If $\mu < \mu_0$, dx/dt is always negative and no fixed point exists. At $\mu = \mu_0$, there is one non-hyperbolic, semi-stable fixed point ($x = 0$). At $\mu > \mu_0$, a pair of stable ($x = \sqrt{\mu}$) and unstable ($x = -\sqrt{\mu}$) hyperbolic fixed points are created.

Figure 6 illustrates that if a VO₂ Mott memristor is biased by a constant voltage v_0 , a small change in v_0 as the bifurcation parameter results in a supercritical saddle-node bifurcation. For the midsize VO₂ device, the bifurcation value for v_0 is approximately 0.0973 V. Figure 6(a) re-plots two of the DRM loci in figure 5 at v_0 levels of 0.0973 V and 0.1 V. At $v_0 = 0.0973$ V, there is a single semi-stable fixed point Q_0 (\times). Raising the input voltage by a tiny amount to $v_0 = 0.1$ V results in a qualitative change in the solution structure and creates a pair of fixed points — the left one Q_1 (\circ) is unstable, and the right one Q_2 (\bullet) is stable. The stability of a fixed point is told by the arrowheads indicating the direction of move for a solution $x(t)$ starting from a initial state located close to it. Figure 6(b) plots the bifurcation diagram of the 1D saddle-node bifurcation with the input voltage as the bifurcation parameter. Solid line and dashed line show the stable and unstable solutions of fixed points x_Q , respectively.

3. Loci of steady states

In the present approach, the internal temperature is embedded in the biphasic model and not treated as a state variable. The set of all fixed points (x_Q, i_Q, v_Q) in the 3D (x, i, v) state space that satisfy the instantaneous relationship $v_Q = R_{\text{ch}}(x_Q)i_Q$ and $(dx/dt)|_Q = 0$ is defined as the steady-state or DC locus of a Mott memristor. Solving the steady-state locus of an isolated Mott memristor is among the first steps for the local linearization analysis. Henceforth, both the (x_Q, i_Q, v_Q) locus and its 2D projections are called the steady-state loci without discerning the dimensional difference.

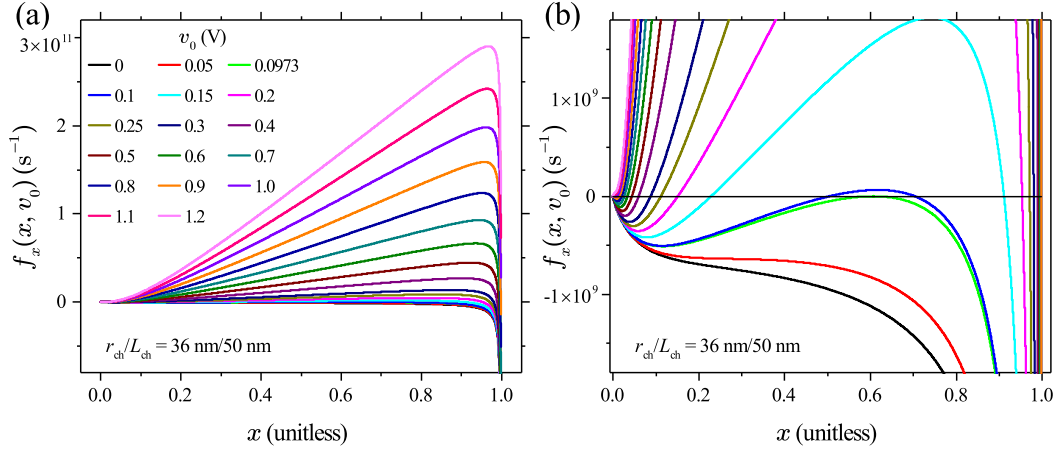


Figure 5: (a) Dynamic route map of $f_x(x, v_0)$ at constant input voltages in the range of 0 to 1.2 V, calculated for the midsize VO₂ Mott memristor. (b) is a zoomed portion of (a) to show that at $v_0 > 0.0973 \text{ V}$, the DR locus intersects the x -axis at two distinctive locations. At $v_0 = 0.0973 \text{ V}$, the DR locus becomes tangent to the x -axis with only one intersection point. At $v_0 < 0.0973 \text{ V}$, the DR locus stays in the fourth quadrant and does not intersect the x -axis.

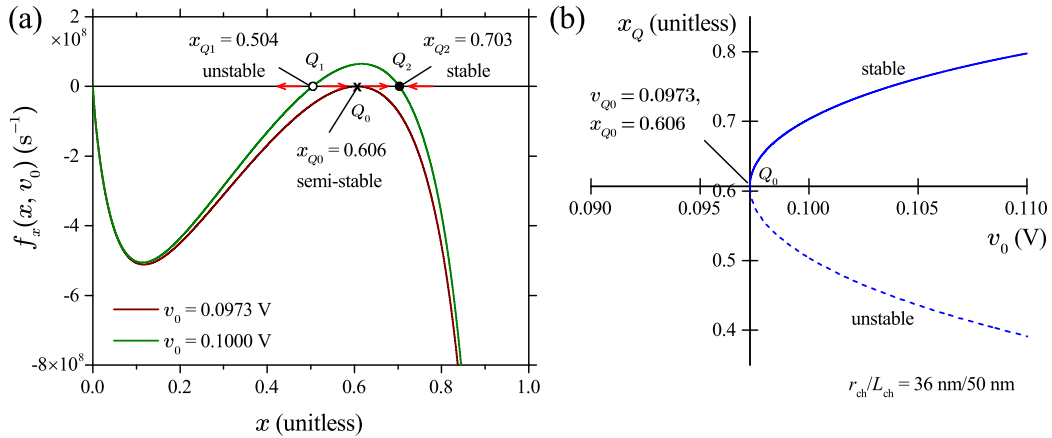


Figure 6: (a) Dynamic routes of $f_x(x, v_0)$ at constant input voltages of 0.0973 V and 0.1 V, calculated for the midsize VO₂ Mott memristor. At $v_0 = 0.0973 \text{ V}$, the single intersection point Q_0 (\times) with the x -axis is a semi-stable fixed point. At $v_0 = 0.1 \text{ V}$, the left intersection point Q_1 (\circ) with the x -axis is an unstable fixed point, and the right intersection point Q_2 (\bullet) with the x -axis is a stable fixed point. Arrowheads show the direction of move for a solution $x(t)$ starting from an initial state located close to a fixed point. (b) Bifurcation diagram of the same device, showing a 1D supercritical saddle-node bifurcation with v_0 as the bifurcation parameter. Solid (dashed) line shows the stable (unstable) solutions of fixed points x_Q .

To obtain the steady-state (x_Q, i_Q, v_Q) locus, one can first define a sequence of $i_Q \in \mathbb{R}$, then find the solutions of the state variable $x = x_Q(i_Q)$ numerically. This is achieved by setting the numerator in equation (7) to be zero, which gives an equation $CA(1 + Bx_Q^2) = -i_Q^2 \ln x_Q$ that can be solved numerically. After solving $x_Q(i_Q)$, voltage v_Q can be calculated by the Ohm's law relationship $v_Q(i_Q) = R_{\text{ch}}(x_Q(i_Q))i_Q$.

However, there is a much easier way to obtain the steady-state (x_Q, i_Q, v_Q) locus. Instead of numerically solving the value of x_Q from a given i_Q , one can first define a sequence of $x_Q \in (0, 1)$, then calculate $i_Q(x_Q)$ analytically using the following formula

$$i_Q(x_Q) = \sqrt{\frac{-CA(1 + Bx_Q^2)}{\ln x_Q}} \quad (9)$$

Voltage v_Q is then calculated by the Ohm's law $v_Q(x_Q) = R_{\text{ch}}(x_Q)i_Q(x_Q)$. The sequence of x_Q can be chosen to be evenly spaced on a linear scale or a logarithmic scale, depending on how fast these functions vary with x_Q . We verified that steady states calculated by both methods are consistent with each other. The analytical method is used for discussions hereafter.

Figure 7(a) shows the steady-state loci of (x_Q, i_Q) calculated by equation (9) for three different VO₂ device sizes, plotted as $x_Q(i_Q)$ since Mott memristors are current-controlled devices. At small currents, the fraction of metallic phase x_Q remains negligibly small. x_Q starts to grow with current in a sublinear fashion once i_Q exceeds a size-dependent threshold level. The current threshold grows with the device size and is at μA level for the shown device sizes.

Figure 7(b) shows the loci of the memristance function $R_{\text{ch}}(x_Q)$ vs. i_Q , which reveal that $R_{\text{ch}}(x_Q)$ has a similar crossover characteristics at the same i_Q thresholds. At small currents, $R_{\text{ch}}(x_Q)$ remains elevated with negligible current dependence. Once i_Q exceeds a size-dependent threshold, $R_{\text{ch}}(x_Q)$ drops rapidly with current in a nonlinear fashion. For the midsize VO₂ device ($r_{\text{ch}} = 36$ nm, $L_{\text{ch}} = 50$ nm), $R_{\text{ch}}(x_Q)$ drops by more than 3 decades from 122.8 k Ω to 97 Ω as i_Q increases from 0 to 1 mA.

Figure 7(c) shows the steady-state loci of (x_Q, v_Q) plotted as $v_Q(x_Q)$, which resemble the shape of a left handled cup. The open left handle is nearly vertical, i.e., at very small x_Q levels a tiny change in x_Q will cause a large change in v_Q . Figure 7(c) left inset plots the extremely-small x_Q region of the (x_Q, v_Q) loci in log-log scale, which reveals that at a given device size, there is a corresponding asymptotic lower bound of steady-state v_Q as x_Q approaches zero. For the midsize VO₂ device ($r_{\text{ch}} = 36$ nm, $L_{\text{ch}} = 50$ nm), the v_Q lower bound turns out to be 0.0973 V (dashed line). Figure 7(c) right inset plots the halfway x_Q region in linear scale, which shows that the $v_Q = 0.0973$ V horizontal line is tangent with the (x_Q, v_Q) locus at its trough of $Q_0 = (0.60628, 0.0973$ V) (marked as \times), the same semi-stable fixed point Q_0 found by the DR analysis. A slight increase in v_Q would bifurcate Q_0 into a pair of fixed points on its left and right. The left inset also tells that in this case, another fixed point would emerge at an extremely-small x_Q level (at $v_Q = 0.2$ V, x_Q is only 10^{-63}), i.e., an insulating steady state exists at a finite voltage. These observations corroborate our previous DR analysis in figure 6. All three (x_Q, v_Q) loci have a sharp peak at $x_Q = 0.00567$ and a rounded trough at $x_Q = 0.60628$, resembling the shape of a cup. Notably the x_Q coordinates of these two extrema are size-independent.

Figure 7(d) shows the steady-state loci of (i_Q, v_Q) plotted as $v_Q(i_Q)$. As current-controlled memristors, the (i_Q, v_Q) loci are letter "N" shaped when plotted with current

as the x axis. They are symmetric with respect to the origin in the first and third quadrants. Therefore one only needs to analyze the first-quadrant halves. Each (i_Q, v_Q) locus has three distinctive regions: A lower positive differential resistance (PDR) region from 0 to a critical current i_{c1} . An NDR region between i_{c1} and a second critical current i_{c2} (see inset). An upper PDR region for even higher currents. Therefore i_{c1} and i_{c2} produce a local maximum and minimum in the (i_Q, v_Q) loci. For the shown device sizes, values of i_{c1} (i_{c2}) are 2.522 μA (269.77 μA), 9.077 μA (971.18 μA) and 14.122 μA (1510.73 μA), respectively. Figure 7(d) also shows that the steady-state or DC loci of (i_Q, v_Q) always pass through the origin (0, 0), satisfying the zero-crossing property of memristors.

It should be noted that the volumetric enthalpy change of IMT Δh_{tr} only shows up in the denominator of the kinetic function $f_x(x, i)$ via coefficient E . Therefore it has no effect in determining the steady-state (i_Q, v_Q) loci. The main effect of IMT on the shape of steady-state (i_Q, v_Q) is applied via coefficient B — the coefficient of the quadratic nonlinearity in memristance function. Coefficient B is approximately the electrical resistivity ratio $\frac{\rho_{\text{ins}}}{\rho_{\text{met}}}$ between the insulating and metallic phases.

The sets of loci plotted in figures 7(a), 7(c) and 7(d) are 2D projections of the steady-state loci (x_Q, i_Q, v_Q) in the 3D state space. Figure 8 shows the locus of (x_Q, i_Q, v_Q) calculated for the midsize VO₂ device ($r_{\text{ch}} = 36$ nm, $L_{\text{ch}} = 50$ nm). It looks somewhat like a twisted handle of a binder clip. The two open legs of the clip are rotated out of the plane defined by the looped clip head. Figure 9 is a zoomed view of figure 8 to visualize the low-current region of the same (x_Q, i_Q, v_Q) locus, so that its 2D projections onto the (i, x) , (v, x) and (i, v) planes can now be directly compared with the loci shown in figures 7(a), 7(c) and 7(d).

4. Local analysis of an isolated Mott memristor

4.1. Linearization and small-signal analysis

Chua's LA theory outlines an algorithmic analysis procedure on nonlinear dynamical electronic circuits using equivalent linearized circuits [37]. The linearized LA analysis examine the locus of fixed points of the composite circuit, the fluctuations around these fixed points, and their Laplace transforms. To explore the complex phenomena of nonlinear dynamical circuits, one can simply apply the LA criteria to access the active parameter domain rather than applying a time-consuming trial-and-error search in the parameter space. A good illustration of this procedure is the memristive HH axon circuit model [31]. Here we apply the local linearization analysis and the LA theory to an isolated VO₂ Mott memristor to gain insights on its behavior near fixed points.

4.1.1. Linearization around a fixed point Considering a fixed point Q with a coordinate (x_Q, i_Q) on the steady-state locus of an isolated Mott memristor, one can expand voltage

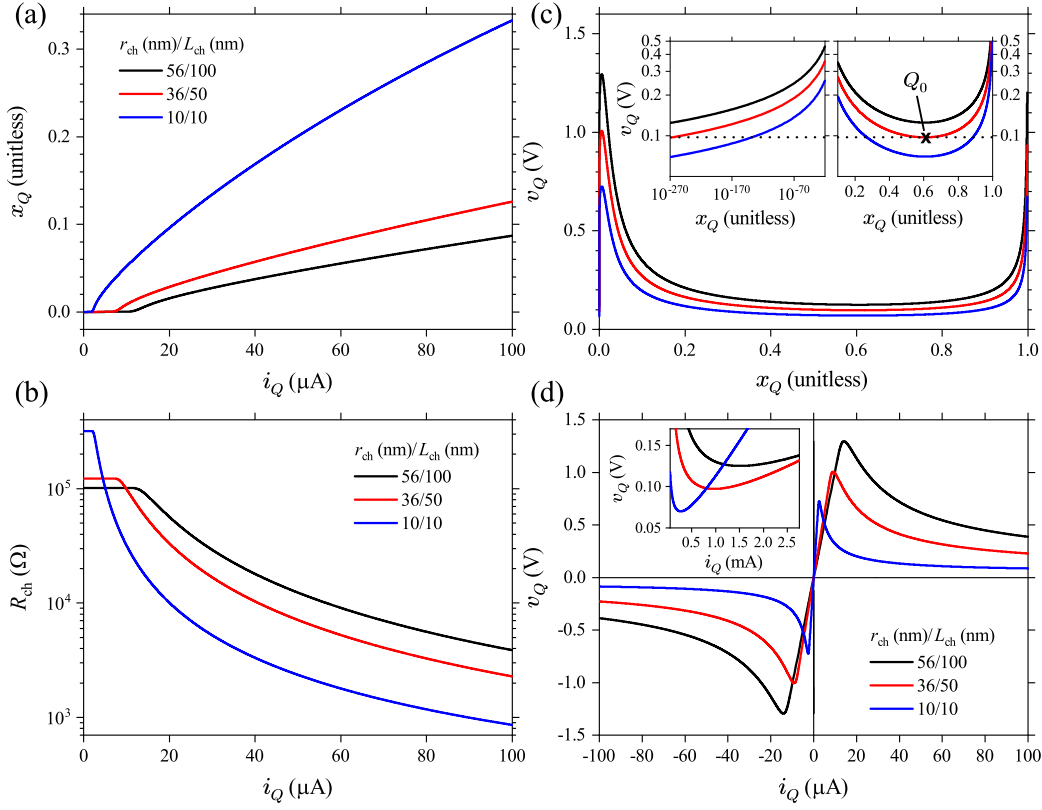


Figure 7: (a) Loci of the steady-state current $i_Q(x_Q)$ calculated by equation (9) and transposed to $x_Q(i_Q)$ with current as the independent variable. (b) Loci of the memristance function $R_{\text{ch}}(x_Q)$ vs. $i_Q(x_Q)$. (c) Loci of the steady-state voltage $v_Q(x_Q)$. Insets are the very-small x_Q (left) and halfway regions (right). Dashed line is $v_0 = 0.0973$ V. Q_0 (\times) is the semi-stable fixed point shown in figure 6. (d) Loci of the steady-state (i_Q, v_Q) showing the zero-crossing property of memristors and a PDR-to-NDR crossover at $i_Q \gtrsim 2.522$ μA , 9.077 μA and 14.122 μA respectively for the three VO_2 device sizes as labeled. Inset reveals another NDR-to-PDR crossover at $i_Q \gtrsim 269.77$ μA , 971.18 μA and 1510.73 μA respectively on the same three loci.

v about the fixed point (x_Q, i_Q) in a Taylor series

$$v(x_Q + \delta x, i_Q + \delta i) = v_Q + i_Q R'_{\text{ch}}(x_Q) \delta x + R_{\text{ch}}(x_Q) \delta i + \text{h.o.t.} \quad (10)$$

where $R'_{\text{ch}}(x_Q) \triangleq \frac{dR_{\text{ch}}}{dx}|_Q$ and h.o.t. denotes higher-order terms in δx and δi . Neglecting h.o.t., we get a linear equation

$$\delta v = i_Q R'_{\text{ch}}(x_Q) \delta x + R_{\text{ch}}(x_Q) \delta i = a_{11}(Q) \delta x + a_{12}(Q) \delta i \quad (11)$$

where coefficients $a_{11}(Q) \triangleq i_Q R'_{\text{ch}}(x_Q)$ and $a_{12}(Q) \triangleq R_{\text{ch}}(x_Q)$. Similarly, the kinetic function $f_x(x, i)$ can be expanded about the fixed point (x_Q, i_Q) in a Taylor series

$$f_x(x_Q + \delta x, i_Q + \delta i) = f_x(x_Q, i_Q) + \frac{\partial f_x(x, i)}{\partial x}|_Q \delta x + \frac{\partial f_x(x, i)}{\partial i}|_Q \delta i + \text{h.o.t.} \quad (12)$$

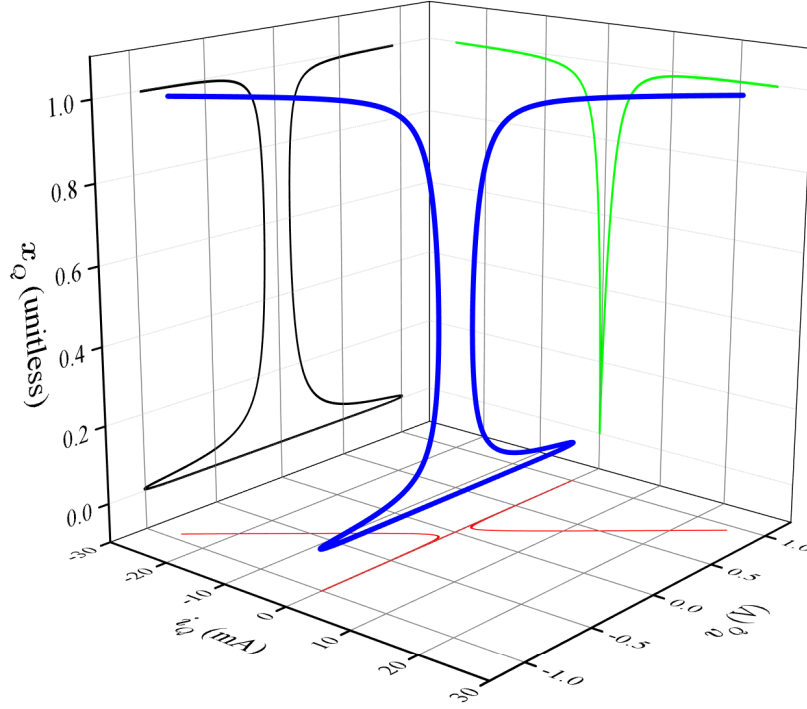


Figure 8: Locus of fixed points (x_Q, i_Q, v_Q) in the 3D state space of (x, i, v) calculated for the midsize VO₂ Mott memristor (blue line) and its 2D projections (green, black, and red lines).

Note that $f_x(x_Q, i_Q) = 0$ since it is a fixed point (x_Q, i_Q) on the steady-state locus. Neglecting h.o.t., we can recast the nonlinear state equation $\frac{dx}{dt} = f_x(x, i)$ into the following linear differential equation

$$\frac{d}{dt}(\delta x) = \left. \frac{\partial f_x(x, i)}{\partial x} \right|_Q \delta x + \left. \frac{\partial f_x(x, i)}{\partial i} \right|_Q \delta i = b_{11}(Q) \delta x + b_{12}(Q) \delta i \quad (13)$$

where coefficients $b_{11}(Q) \triangleq \left. \frac{\partial f_x(x, i)}{\partial x} \right|_Q$ and $b_{12}(Q) \triangleq \left. \frac{\partial f_x(x, i)}{\partial i} \right|_Q$. Applying Equations (2) and (3), one can easily obtain the expressions for the following three linear-term coefficients

$$a_{11}(Q) = -\frac{2Bi_Q x_Q}{A(1+Bx_Q^2)^2} \quad (14)$$

$$a_{12}(Q) = R_{\text{ch}}(x_Q) = \frac{1}{A(1+Bx_Q^2)} \quad (15)$$

$$b_{12}(Q) = \frac{4x_Q(\ln x_Q)^2 i_Q}{DA(1+Bx_Q^2)[1-x_Q^2+2x_Q^2 \ln x_Q+2E(x_Q \ln x_Q)^2]} \quad (16)$$

To obtain the expression for $b_{11}(Q)$, we rewrite $f_x(x, i)$ as $f_x(x, i) = \frac{i^2 X(x) + Y(x)}{Z(x)}$, where the three auxiliary functions are defined as $X(x) = \frac{2x(\ln x)^2}{A(1+Bx^2)}$, $Y(x) = 2Cx \ln x$, and $Z(x) = D[1-x^2+2x^2 \ln x+2E(x \ln x)^2]$. Applying the quotient rule $\frac{d}{dx} \frac{X(x)}{Z(x)} =$

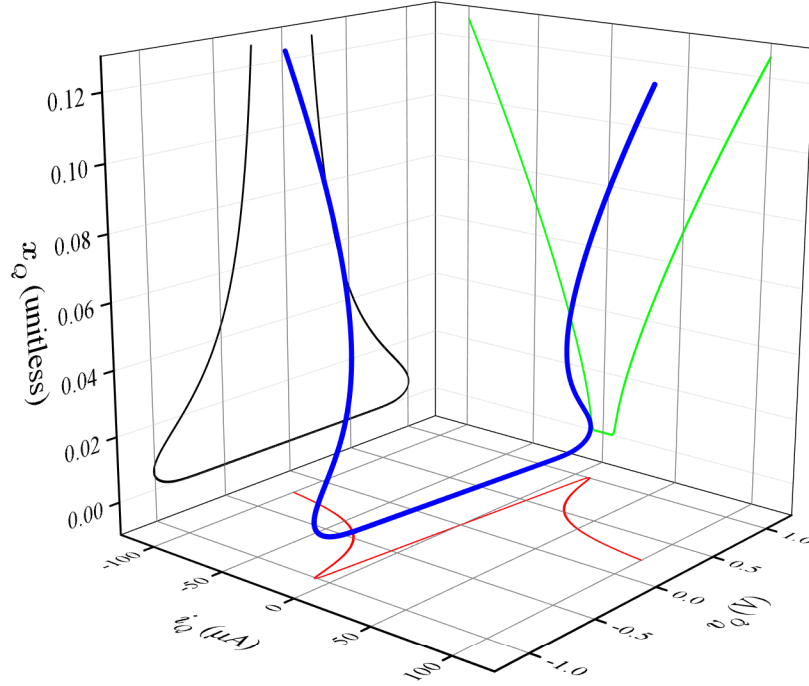


Figure 9: A zoomed view of figure 8 to visualize the low-current region of the fixed-point locus (x_Q, i_Q, v_Q) calculated for the midsize VO₂ Mott memristor. Its 2D projections (green, black, and red lines) can now be compared with the loci of $i_Q(x_Q)$, $v_Q(x_Q)$, and (i_Q, v_Q) shown in figure 7.

$\frac{X'(x)Z(x) - X(x)Z'(x)}{Z(x)^2}$, we get

$$b_{11}(Q) = i_Q^2 \left. \frac{X'(x)Z(x) - X(x)Z'(x)}{Z(x)^2} \right|_Q + \left. \frac{Y'(x)Z(x) - Y(x)Z'(x)}{Z(x)^2} \right|_Q \quad (17)$$

The formulas for $X'(x) \triangleq \frac{dX(x)}{dx}$, $Y'(x) \triangleq \frac{dY(x)}{dx}$ and $Z'(x) \triangleq \frac{dZ(x)}{dx}$ are $X'(x) = \frac{2 \ln x (2Bx^2 - Bx^2 \ln x + \ln x + 2)}{A(1+Bx^2)^2}$, $Y'(x) = 2C(\ln x + 1)$ and $Z'(x) = 4Dx \ln x [1 + E(\ln x + 1)]$.

Figures 10(a)–10(d) plot the current dependence of the linear-term coefficients a_{11} , a_{12} , b_{11} and b_{12} calculated by equations (14)–(17) for three different VO₂ device sizes. They show that coefficients a_{11} and b_{12} are odd functions of the driving current, while coefficients b_{11} and a_{12} are even functions of the driving current. a_{12} is the same as the memristance R_{ch} and is always positive. In contrast, b_{11} is always negative.

4.1.2. Complex-domain equivalent circuit Many insights can be gained about an isolated Mott memristor in the realm of complex analysis. As the second step of the local analysis, we can obtain its complex-domain equivalent circuit by the linear Laplace transform $\hat{f}(s) \triangleq \int_0^\infty f(t)e^{-st} dt$ that maps a function $f(t)$ in the time domain to a function $\hat{f}(s)$ in the complex domain \mathbb{C} , whose elements are complex frequencies $s = \sigma + i\omega$. The complex domain is also known as the s domain. A direct benefit of the Laplace transform is that it turns a differential equation into an algebraic equation.

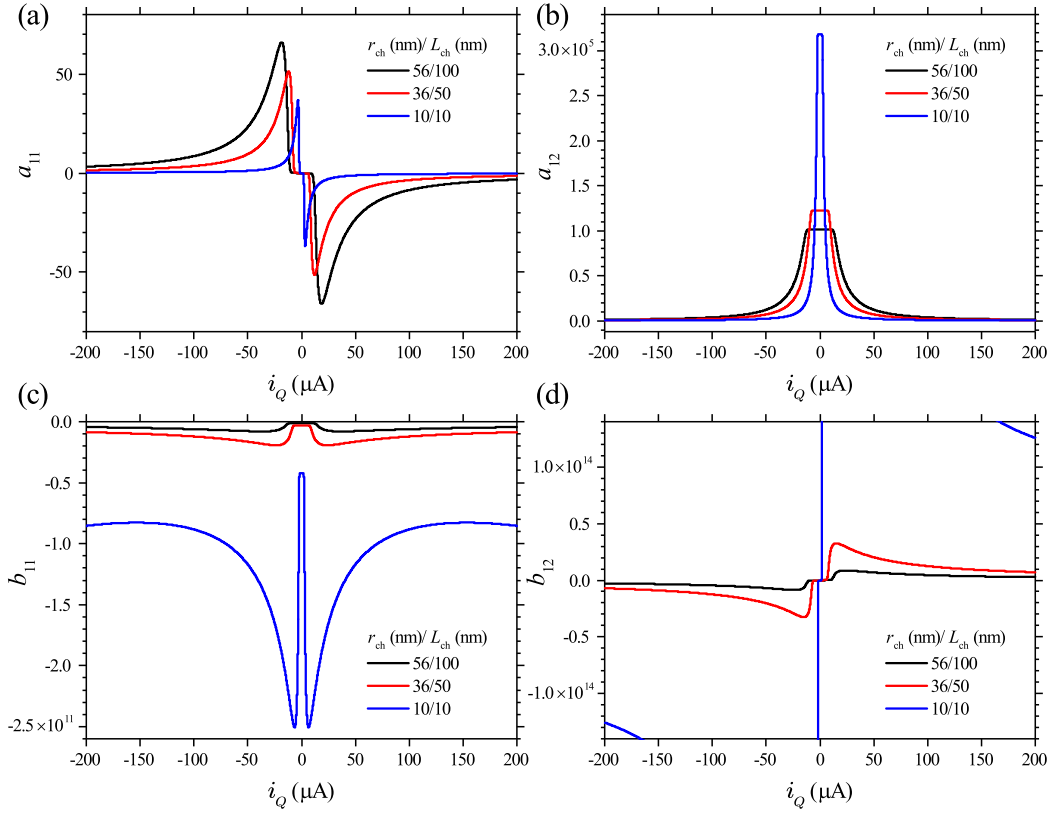


Figure 10: Current dependences of the linear-term coefficients (a) a_{11} , (b) a_{12} , (c) b_{11} , and (d) b_{12} in the linearized expressions of voltage v and the kinetic function $f_x(x, i)$ about a fixed point on the steady-state locus of three different-sized VO₂ Mott memristors as labeled.

Taking the Laplace transforms of equations (11) and (13), we obtain

$$\hat{v}(s) = a_{11}(Q)\hat{x}(s) + a_{12}(Q)\hat{i}(s) \quad (18)$$

$$s\hat{x}(s) = b_{11}(Q)\hat{x}(s) + b_{12}(Q)\hat{i}(s) \quad (19)$$

where $\hat{x}(s)$, $\hat{v}(s)$ and $\hat{i}(s)$ denote the Laplace transforms of $\delta x(t)$, $\delta v(t)$ and $\delta i(t)$, respectively. Solving equation (19) for $\hat{x}(s)$, we obtain

$$\hat{x}(s) = \frac{b_{12}(Q)\hat{i}(s)}{s - b_{11}(Q)} \quad (20)$$

Substituting equation (20) for $\hat{x}(s)$ in equation (18) and solving for the impedance function $Z(s; Q) \triangleq \hat{v}(s)/\hat{i}(s)$, we obtain the s -domain impedance function

$$Z(s; Q) = \frac{a_{11}(Q)b_{12}(Q)}{s - b_{11}(Q)} + a_{12}(Q) \quad (21)$$

For a current-controlled memristor, the impedance function $Z(s; Q)$ in equation (21) is the proper choice for its transfer function $H(s; Q)$. For a voltage-controlled memristor, admittance function $Y(s; Q)$ should be used. Chua pointed out that for a 1D system with just one port state variable, its transfer function is also the scalar

complexity function that forms the basis for the LA analysis [37]. In Chua’s original LA formulations for reaction-diffusion systems, a port state variable of a “reaction” cell (equivalent to a lumped circuit element) interacts with the neighboring cells via an energy or matter flow such as diffusion. Whereas a nonport state variable describes isolated internal dynamics and does not interact with other cells. The concept of LA is defined concerning only port state variables. Clearly the state variable x in the Mott memristor model is a port state variable, since it interacts with a coupled circuit element through a current (energy) flow.

Since the s -domain representation of a capacitor looks like a “resistance” $1/sC$, one can recast the small-signal impedance function $Z(s; Q)$ of a Mott memristor about a fixed point Q as an equivalent circuit that consists of three virtual elements: a capacitor C_1 in parallel with a resistor R_1 , both of them in series with a second resistor R_2

$$Z(s; Q) = \frac{\left(\frac{1}{sC_1}\right)R_1}{\left(\frac{1}{sC_1}\right) + R_1} + R_2 \quad (22)$$

where

$$R_1 \triangleq -\frac{a_{11}(Q)b_{12}(Q)}{b_{11}(Q)} \quad (23)$$

$$R_2 \triangleq a_{12}(Q) = R_{\text{ch}}(x_Q) \quad (24)$$

$$C_1 \triangleq \frac{1}{a_{11}(Q)b_{12}(Q)} \quad (25)$$

Figures 11(a)–11(c) plot the current dependence of the three virtual circuit elements R_1 , R_2 and C_1 calculated by equations (23)–(25) for three different VO₂ device sizes. They are all even functions of the driving current, so we only plot the positive x -axis halves. First thing to notice is that R_1 and C_1 stay negative at any current for all three device sizes calculated. In contrast, R_2 remains positive at any current. Note that R_2 is the same as a_{12} and $R_{\text{ch}}(x_Q)$. Therefore, in the s -domain a Mott memristor can be modeled as a nonlinear positive resistor in series with a composite reactive element consisting of a nonlinear negative capacitor and a nonlinear negative resistor placed in parallel. This small-signal equivalent circuit in the s -domain is shown in figure 11(b) inset.

Since a negative capacitance translates to a positive frequency-dependent inductive reactance, it means that a Mott memristor (or generally a current-controlled LAM) has an apparent inductive reactance without involving a magnetic field. In physiology, an anomalous inductive reactance was observed as early as 1930s in voltage clamp measurements of the squid giant axon [63], but this perplexing phenomenon was not understood until Chua’s memristive formulation for the potassium and sodium ion channels [31].

Figure 11(d) plots the current dependence for the sum of the two resistances ($R_1 + R_2$). At small currents, ($R_1 + R_2$) is positive and remains nearly constant. As current increases, ($R_1 + R_2$) drops abruptly and becomes negative as current exceeds a limit that is identical with the critical current i_{c1} for the lower PDR to NDR transition

on the steady-state (i_Q, v_Q) loci (see figure 7(d)), at $2.522 \mu\text{A}$, $9.077 \mu\text{A}$ and $14.122 \mu\text{A}$ respectively for the three device sizes. The negative $(R_1 + R_2)$ then starts to rise with current. Inset of figure 11(d) shows that $(R_1 + R_2)$ becomes positive again as current exceeds a much larger limit that is identical with the critical current i_{c2} for the NDR to upper PDR transition on the steady-state (i_Q, v_Q) loci (see figure 7(d) inset), at $269.77 \mu\text{A}$, $971.18 \mu\text{A}$ and $1510.73 \mu\text{A}$ respectively for the same three devices. The one-to-one correspondence between the sign of $(R_1 + R_2)$ and the sign of the slope on the steady-state (i_Q, v_Q) loci indicates that the three-element equivalent circuit shown in figure 11(b) inset is the proper small-signal representation of a Mott memristor in the s -domain.

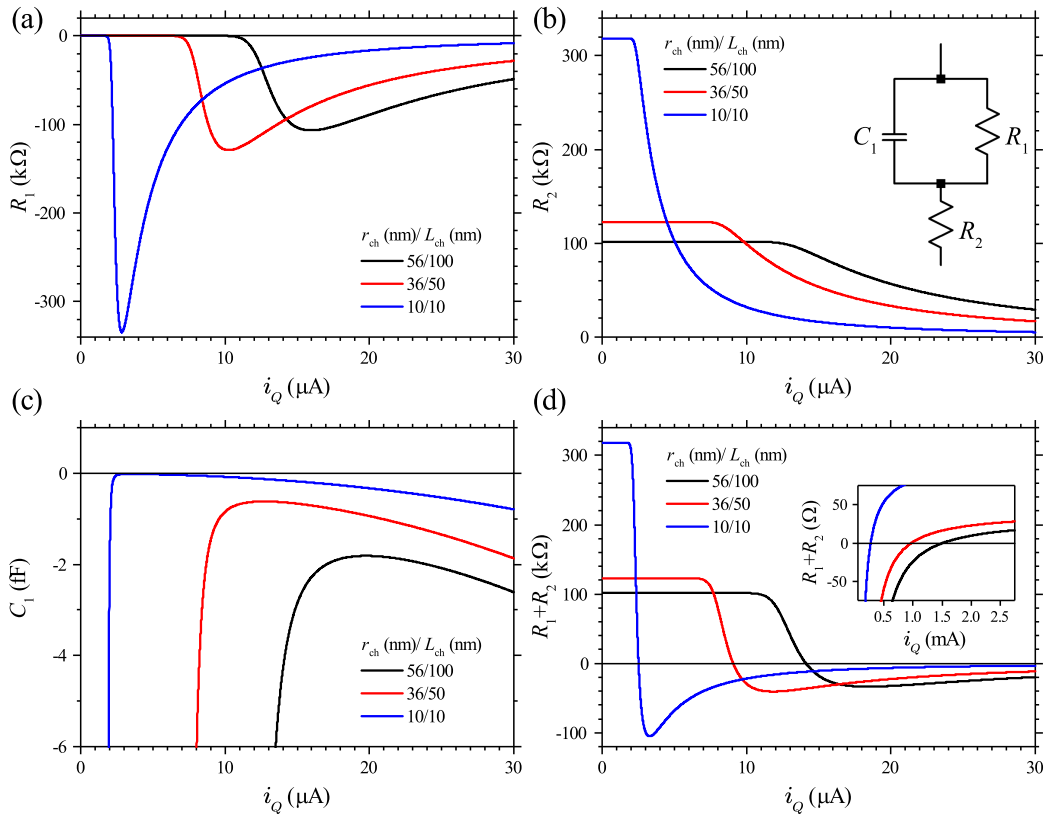


Figure 11: Current dependences of the three virtual circuit elements (a) R_1 , (b) R_2 and (c) C_1 comprising the s -domain impedance function $Z(s; Q)$ about a fixed point on the steady-state (i_Q, v_Q) loci of three different-sized VO₂ Mott memristors as labeled. R_1 and C_1 remain negative at any current for all three device sizes. Inset of (b) shows the small-signal equivalent circuit in the s -domain. (d) Current dependence for the sum of the two resistances $(R_1 + R_2)$. $(R_1 + R_2)$ turns negative as current exceeds a size-dependent limit. Inset of (d) shows that $(R_1 + R_2)$ becomes positive again as current exceeds a much larger size-dependent limit. These two current limits are identical with the critical currents i_{c1} at the lower PDR to NDR and i_{c2} at the NDR to upper PDR transitions on the steady-state (i_Q, v_Q) loci, respectively (see figure 7(d) and inset).

4.2. Pole-zero diagram and Chua's local activity theorem

4.2.1. *Poles and zeros of the transfer function* For a dynamical system, the poles and zeros of its transfer function $H(s; Q)$ in the s -domain can tell about important characteristics of the system response without solving the complete differential equations. The first step of pole-zero analysis is to rewrite the s -domain small-signal transfer function $H(s; Q)$ as a rational function of s , i.e., a ratio of two polynomials. For the case of a 1D current-controlled Mott memristor, both the denominator and numerator s polynomials have a degree of $n = 1$, therefore its impedance function $Z(s; Q)$ is written as

$$Z(s; Q) = \frac{b_1 s + b_0}{a_1 s + a_0} \quad (26)$$

where all of the coefficients of s polynomials in the denominator and numerator are real numbers. Using equation (22), the expressions for these four coefficients are derived as

$$a_0 = 1 \quad (27)$$

$$a_1 = R_1 C_1 \quad (28)$$

$$b_0 = R_1 + R_2 \quad (29)$$

$$b_1 = R_1 R_2 C_1 \quad (30)$$

Since a_0 is a constant and $b_0 = R_1 + R_2$ is already discussed (see figure 11(d)), we only need to look at $a_1 = R_1 C_1$ and $b_1 = R_1 R_2 C_1$. Both of them are even functions of the input current. Their current dependence are plotted in figure 12 for three different VO₂ device sizes.

A rational transfer function can be further rewritten in a factored or pole-zero form by expressing the s polynomials in the denominator and numerator as products of linear factors. The roots of the denominator polynomial are the poles, and the roots of the numerator polynomials are the zeros. For any polynomial with real coefficients, its roots are either real or complex conjugate pairs.

For an isolated 1D Mott memristor, there is just one pole and one zero. To obtain the expressions for the zero and the pole of $Z(s; Q)$, recast equation 26 as

$$Z(s; Q) = \frac{k(s - z)}{(s - p)} \quad (31)$$

where $k = b_1/a_1 = R_2$ is a positive real coefficient, z and p denote respectively the zero and the pole of $Z(s; Q)$. The expressions for z and p are

$$z = -\frac{b_0}{b_1} = -\frac{R_1 + R_2}{R_1 R_2 C_1} \quad (32)$$

$$p = -\frac{a_0}{a_1} = -\frac{1}{R_1 C_1} = b_{11} \quad (33)$$

Figure 13 show the loci of the zero z and the pole p versus input current for three different VO₂ device sizes. It is conspicuous that both z and p are located on the real axis in the complex plane, and both are even functions of current. It may be noted that

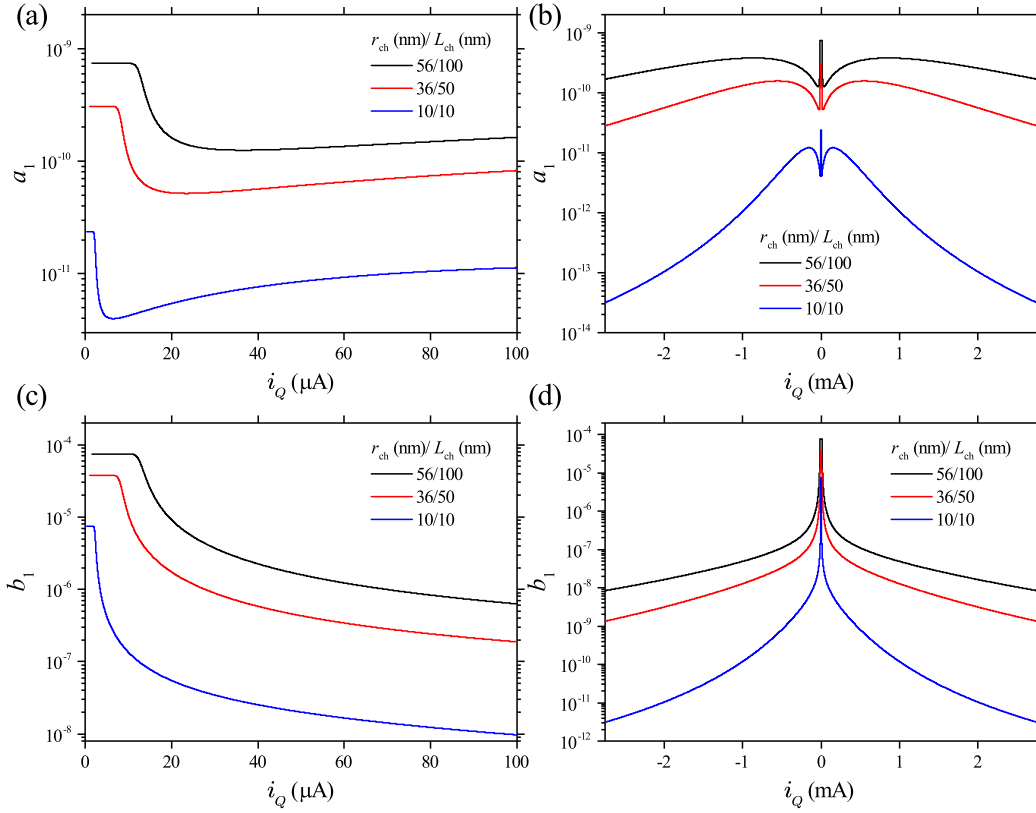


Figure 12: Current dependences for two of the four s -polynomial coefficients (a) a_1 (low-current part), (b) a_1 (wide range), (c) b_1 (low-current part) and (d) b_1 (wide range) in the rational-function representation of the impedance function $Z(s; Q)$ about a fixed point on the steady-state (i_Q, v_Q) locus of three different-sized VO₂ Mott memristors as labeled. The other two coefficients are $a_0 = 1$ and $b_0 = R_1 + R_2$ (see figure 11(d)).

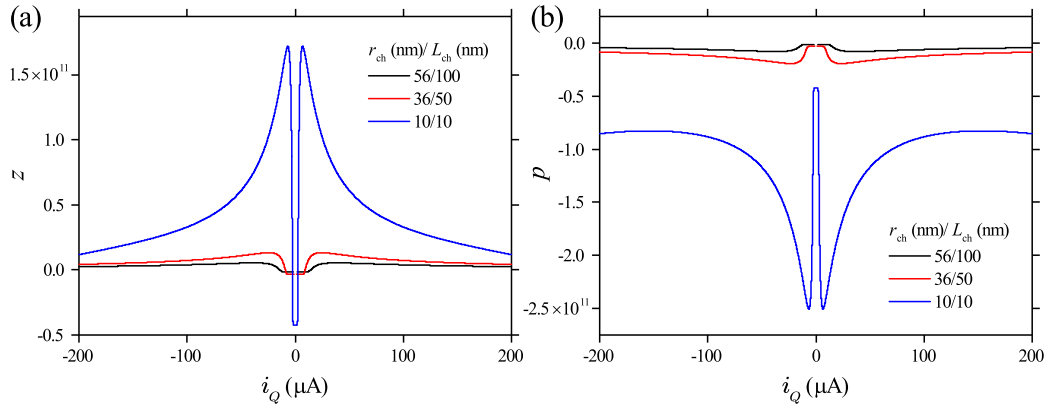


Figure 13: Current dependence of (a) the zero z and (b) the pole p of the s -domain impedance function $Z(s; Q)$ about a fixed point on the steady-state (i_Q, v_Q) locus of a VO₂ Mott memristor, calculated for three different device sizes as labeled.

p is already plotted in figure 10(c) in the form of b_{11} . It is replotted as figure 13(b) for

a side-by-side comparison with z .

Since both the zero and the pole of $Z(s; Q)$ are located on the real axis, one can simply look at their signs to tell about the local dynamical behaviors about a fixed point, as it will be discussed in the next subsection. Generally speaking, for a 1D uncoupled Mott memristor, its pole p (or b_{11}) remains negative at any current level. In contrast, its zero z has two sign reversals at two distinctive input current levels. These characteristics are illustrated in figure 14 which shows the current dependence of p and z of $Z(s; Q)$ calculated for the midsize VO₂ device ($r_{\text{ch}} = 36$ nm, $L_{\text{ch}} = 50$ nm).

Figures 14(a) and 14(b) show the loci of $p(i_Q)$ for the low-current part (up to 100 μA) and a wide range (up to 2 mA), respectively. p has a non-monotonic current dependence, but $p < 0$ always holds true. Figure 14(c) shows that z is initially negative at small currents, then it turns positive if the current is higher than ≈ 9.077 μA , as indicated by a pair of nearby fixed points $\{Q_1, Q_2\}$ across zero. Their coordinates $[x_Q, i_Q, v_Q, \text{Re}(z)]$ are $[0.00566, 9.075$ μA , 1.007 V, $-5.882 \times 10^6]$ for Q_1 and $[0.00567, 9.078$ μA , 1.007 V, $3.388 \times 10^6]$ for Q_2 . Figure 14(d) shows that z becomes negative again if current exceeds ≈ 971.18 μA , as indicated by a pair of nearby fixed points $\{Q_3, Q_4\}$ across zero. Their coordinates are $[0.60628, 971.171$ μA , 0.097 V, $3.854 \times 10^4]$ for Q_3 and $[0.60629, 971.203$ μA , 0.097 V, $-8.477 \times 10^4]$ for Q_4 . The two critical currents for sign reversals in z match exactly with the ones that separate the NDR region from the lower and upper PDR regions on the steady-state (i_Q, v_Q) locus of the same device, as shown in figure 14(e) and 14(f). The coincidences are confirmed by examining the locations of the same two pairs of nearby fixed points $\{Q_1, Q_2\}$ and $\{Q_3, Q_4\}$ on the (i_Q, v_Q) locus.

4.2.2. Chua's local activity theorem Chua's local analysis method established a practical set of criteria to classify the dynamics of an isolated or uncoupled nonlinear circuit element about its fixed points. The approach to determine if a linearized element is LP or locally active about a fixed point $Q = (x_Q, i_Q, v_Q)$, is to check if its output fluctuations in response to small input fluctuations dissipate over time, or get amplified otherwise. For the discussion, we choose the example of a 1D current-controlled memristor with current as the input and voltage as the output. Their roles are exchanged for a voltage-controlled memristor. Mathematically, with a homogeneous initial condition $(\delta x(0), \delta i(0), \delta v(0)) = \mathbf{0}$ (no fluctuation at $t = 0$), a linearized element is LP if and only if (iff) the fluctuation energy integrated over time remains positive

$$\text{LP} \Leftrightarrow \int_0^{t'} \delta i(t) \cdot \delta v(t) dt \geq 0 \quad (34)$$

for any finite time interval $t' > 0$. The uncoupled element is locally active at a fixed point Q , iff there exists an input fluctuation $\delta i(t)$ and a finite time $0 < T < \infty$, such that the integrated fluctuation energy becomes *negative*. For a multidimensional element, the fluctuation power to be integrated is a scalar "dot" product between the two vectors $\delta \mathbf{i}(t)$ and $\delta \mathbf{v}(t)$.

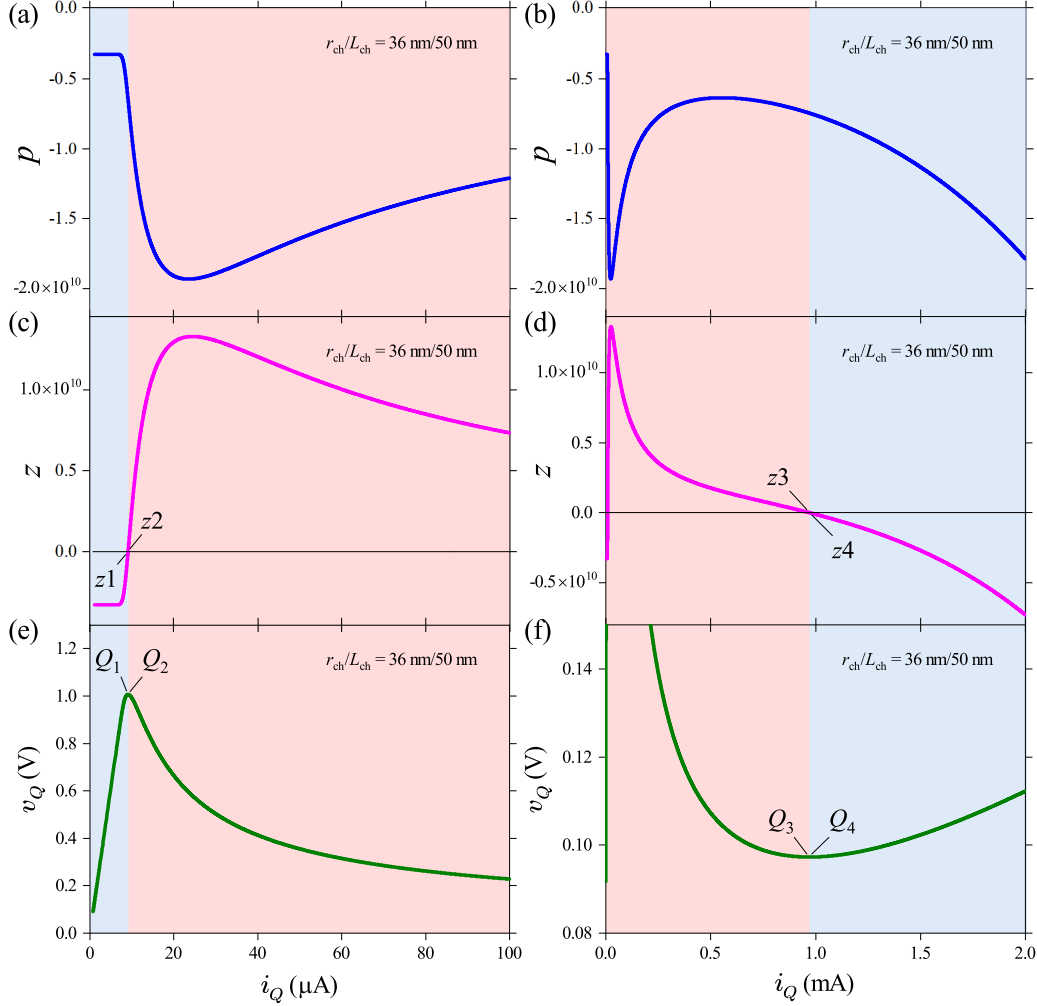


Figure 14: Current dependence of the pole p of $Z(s; Q)$ in (a) and (b), and the zero z in (c) and (d) for the midsize VO_2 Mott memristor. p remains negative at any current. For z , (c) shows a $(-) \rightarrow (+)$ sign reversal at $9.077 \mu\text{A}$, as indicated by a pair of nearby zeros $\{z1, z2\}$ with opposite sign; (d) shows a $(+) \rightarrow (-)$ sign reversal at $971.18 \mu\text{A}$, as indicated by a pair of nearby zeros $\{z3, z4\}$ with opposite sign. (e) and (f) show the corresponding parts of the steady-state (i_Q, v_Q) locus of the same device. The crossovers between the NDR region (red) and the lower and upper PDR regions (blue) at the local voltage extrema coincide with the sign reversals in z , as indicated by the locations of $\{Q_1, Q_2\}$ and $\{Q_3, Q_4\}$ pairs of fixed points on the (i_Q, v_Q) locus.

However, it is not practical to inspect the time-domain integral for all possible input fluctuations. By applying the Laplace transform, Chua derived a mathematically equivalent but much more practical formula for the local passivity theorem in the complex domain. For the 1D scalar case, the necessary and sufficient condition for an uncoupled 1D circuit element to be LP is that its complexity function or transfer function $H(s; Q)$ is a positive real (PR) function, which satisfies both (1) $\text{Im}[H(s; Q)] = 0$ if $\text{Im}[s] = 0$, and (2) $\text{Re}[H(s; Q)] \geq 0$ if $\text{Re}[s] \geq 0$. Condition (1) is always satisfied since

$H(s; Q)$ is a rational function. Condition (2) means that the closed right half plane (RHP) of s maps into the closed RHP of $H(s; Q)$. A simple example for a PR function is $H(s; Q) = a + bs + cs^{-1}$, where a , b , and $c \geq 0$.

Chua proved the following local passivity theorem as a practical test for the PR condition: An uncoupled 1D circuit element is LP at a fixed point *iff all of the following four criteria are satisfied*

- i) $H(s; Q)$ has no poles in the open RHP ($\text{Re}(s) > 0$).
- ii) $H(s; Q)$ has no higher-order poles (degree $n \geq 2$) on the imaginary axis (Im axis).
- iii) If $H(s; Q)$ has a simple pole $s = i\omega_p$ on the Im axis, then the residue of $H(s; Q)$ at $i\omega_p$ must be a PR number.
- iv) The Im axis (excluding poles) maps into the closed RHP of $H(s; Q)$, i.e., $\text{Re}[H(i\omega; Q)] \geq 0$ for all $\omega \in (-\infty, \infty)$ where $s = i\omega$ is not a pole.

The LA theorem is derived by negating any one of the above conditions. That is to say, an uncoupled 1D circuit element is locally active at a fixed point *iff any one of the following four criteria is satisfied*

- i) $H(s; Q)$ has a pole in the open RHP $\text{Re}(s) > 0$.
- ii) $H(s; Q)$ has a higher-order pole (degree $n \geq 2$) on the Im axis.
- iii) $H(s; Q)$ has a simple pole on the Im axis with negative-real or complex residue.
- iv) At least some points on the Im axis map into the open left half plane (LHP) of $H(s; Q)$, i.e., $\text{Re}[H(i\omega; Q)] < 0$ for some $\omega \in (-\infty, \infty)$.

For a system of higher dimensions, Chua proved a similar set of four test criteria for LA, wherein the complexity function $H(s; Q)$ for an 1D element is replaced by the complexity matrix for a multidimensional element.

As elaborated in Ref. [40], the local stability of a fixed point is a property that is independent of the local activity of dynamics about it. Near a fixed point, an isolated memristor may have four possible combinations of local stability and local activity properties that can lead to persistent or decaying dynamics. Since the condition of both LP and locally unstable is unphysical to realize, in general one only needs to consider three possible scenarios: LP and stable, locally active and stable which is termed as edge of chaos (EOC) by Chua, and locally active but unstable (LA\EOC).

For a 1D uncoupled memristor, if its transfer function has a positive coefficient ($k > 0$ in equation (31)), the dynamical class about a fixed point is told by where the pole and zero of its transfer function are located in the complex plane, as specified below

- i) Locally Passive \Leftrightarrow pole in open LHP ($\text{Re}(p) < 0$) and zero in closed LHP ($\text{Re}(z) \leq 0$)
- ii) Edge of Chaos \Leftrightarrow pole in open LHP ($\text{Re}(p) < 0$) and zero in open RHP ($\text{Re}(z) > 0$)
- iii) Locally Active but Unstable \Leftrightarrow pole in closed RHP ($\text{Re}(p) \geq 0$)

Plots of $\text{Im}(p)$ versus $\text{Re}(p)$ and $\text{Im}(z)$ versus $\text{Re}(z)$, known as pole-zero diagram, thus offer a graphical determination of local steady-state dynamics without resorting to time-domain integration.

As discussed previously, for a current-controlled Mott memristor both the pole and the zero are located on the real axis. The pole p of its impedance function $Z(s; Q)$ is always in the open LHP ($\text{Re}(p) < 0$), therefore it does not possess the LA\EOC dynamics in (iii). On the other hand, the zero z of $Z(s; Q)$ can reside in either the closed LHP or the open RHP, depending on the input current amplitude. In figure 14, we have shown that $\text{Re}(z)$ flips its sign twice depending on the input current, and the two sign reversals in $\text{Re}(z)$ coincide with the crossovers between the NDR region and the lower and upper PDR regions on the steady-state (i_Q, v_Q) locus.

4.2.3. Pole-zero diagram In figure 15, we visualize the evolution of p and z locations in the complex plane as functions of the input current for the current-controlled midsize VO_2 Mott memristor. Figure 15(a) shows that $\text{Re}(p) < 0$ is always satisfied. The coordinates $[x_Q, i_Q, v_Q, \text{Re}(p)]$ for the minimal and maximal calculated values of p , labeled as p_{\min} and p_{\max} , are $[0.998, 25.268 \text{ mA}, 0.935 \text{ V}, -9.543 \times 10^{13}]$ and $[1 \times 10^{-145}, 1.074 \text{ } \mu\text{A}, 0.132 \text{ V}, -3.273 \times 10^9]$, respectively. As may be noted, p_{\min} and p_{\max} in our calculations are not the actual bounds of p , since x_Q can approach very closely to its asymptotes 0 and 1 but will never touch them.

Figure 15(b) shows that the zero z is located in the LHP at zero current, and it shifts to the right as current increases. z crosses the Im axis into the RHP at a critical current of $9.077 \text{ } \mu\text{A}$, as indicated by a pair of nearby fixed points $\{z1, z2\}$ on the opposite side of the Im axis (the same ones as shown in figure 14). z continues shifting to the right with current until it reaches a maximum value at z_{\max} with a coordinate of $[0.03549, 24.482 \text{ } \mu\text{A}, 0.578 \text{ V}, 1.327 \times 10^{10}]$. Then it reverses course and shifts to the left with current. z crosses the Im axis again and returns to the LHP at a second critical current of $971.18 \text{ } \mu\text{A}$, as indicated by a pair of nearby fixed points $\{z3, z4\}$ on the opposite side of the Im axis (the same ones as shown in figure 14). Continuously increasing the current will drive x_Q asymptotically toward 1 and further decrease z . We stop the calculation at z_{\min} with a coordinate of $[0.998, 25.268 \text{ mA}, 0.935 \text{ V}, -9.467 \times 10^{13}]$. We use the same blue and red colors as shown in figure 14 to highlight the LP and EOC regions, respectively.

Applying the pole-zero diagram LA criteria specified above, we conclude that an uncoupled 1D Mott memristor about a fixed point either belongs to the LP class or the EOC class, but can never belong to the LA\EOC class. For the midsize VO_2 device, the LP \rightarrow EOC transition occurs at $(x_Q, i_Q, v_Q) \approx (0.00567, 9.076 \text{ } \mu\text{A}, 1.007 \text{ V})$. The EOC \rightarrow LP transition occurs at $(x_Q, i_Q, v_Q) \approx (0.60629, 971.2 \text{ } \mu\text{A}, 0.0973 \text{ V})$.

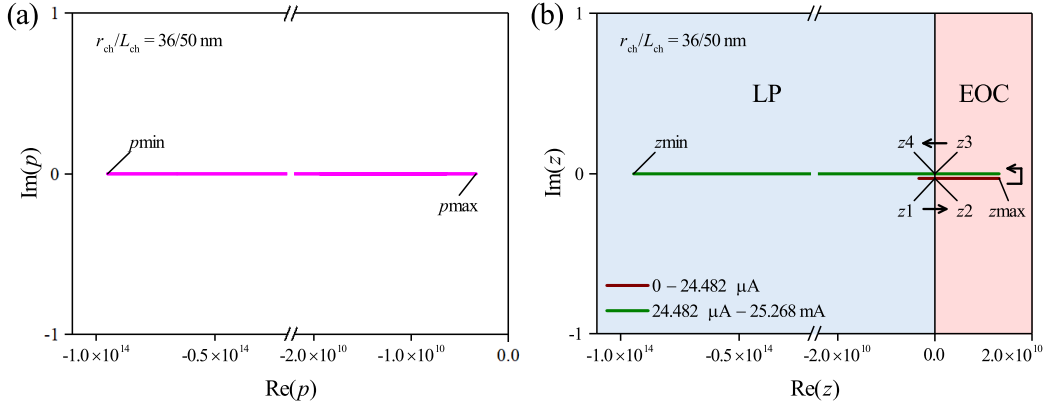


Figure 15: Locations of (a) the pole p and (b) the zero z in the complex plane as functions of input current, calculated for the midsize VO_2 Mott memristor. Both p and z are located on the real axis. p remains in LHP with its minimal and maximal calculated values indicated by p_{min} and p_{max} . z is located in LHP at $i_Q = 0$ and shifts to the right with current, crossing the imaginary axis into RHP at $9.077 \mu\text{A}$ as indicated by $\{z_1, z_2\}$. It continues shift to the right until reaching z_{max} at $24.482 \mu\text{A}$, then shifts to the left with current and reenters LHP at $971.18 \mu\text{A}$ as indicated by $\{z_3, z_4\}$. The minimum of z is approximately at z_{min} . The part of z locus between 0 and $24.482 \mu\text{A}$ (brown) is shifted vertically for clarity. The LP and EOC regions are highlighted by blue and red colors, respectively.

4.3. Frequency response

An important question now arises: for an uncoupled 1D Mott memristor that is current-biased in the EOC region (coinciding with its NDR region), will it remain to be locally active so that it can amplify a small sinusoidal input fluctuation at arbitrarily-high frequencies? Otherwise, is there a finite upper limit for the input fluctuation frequency, beyond which the element cannot provide an AC signal gain anymore? In this section, we move the small-signal analysis to the frequency domain, which allows us to apply the fourth criterion in Chua's LA theorem to get the answers.

For dynamical systems, it is useful to study the system's frequency response. In small-signal analysis, this is performed by applying a single-frequency sinusoidal fluctuation of current input $i(t) = I \sin \omega t$ with an angular frequency $\omega = 2\pi f$, where f is the frequency of the sinewave. The amplitude $I \ll 1$ is very small to satisfy the small-signal condition. For a 1D Mott memristor about a fixed point Q , substituting $s = i\omega$ for the complex frequency s in the small-signal impedance $Z(s; Q)$ in equation (26) and rearranging into its real and imaginary parts, we get

$$Z(i\omega; Q) = \left[\frac{a_0 b_0 + a_1 b_1 \omega^2}{a_0^2 + a_1^2 \omega^2} \right] + i \left[\frac{(a_0 b_1 - a_1 b_0) \omega}{a_0^2 + a_1^2 \omega^2} \right] \quad (35)$$

The functions $\text{Re}Z(i\omega; Q)$ and $\text{Im}Z(i\omega; Q)$ are the real and imaginary parts of the frequency response expressed in terms of the small-signal impedance $Z(i\omega; Q)$, both

expressed as rational functions of ω :

$$\operatorname{Re}Z(i\omega; Q) = \frac{a_0b_0 + a_1b_1\omega^2}{a_0^2 + a_1^2\omega^2} \quad (36)$$

$$\operatorname{Im}Z(i\omega; Q) = \frac{(a_0b_1 - a_1b_0)\omega}{a_0^2 + a_1^2\omega^2} \quad (37)$$

where the coefficients a_0 , a_1 , b_0 and b_1 are given in equations (27)–(30).

Figure 16(a) and 16(b) plot the frequency dependence of $\operatorname{Re}Z(i\omega; Q)$ and $\operatorname{Im}Z(i\omega; Q)$ (also referred to as $\operatorname{Re}Z$ and $\operatorname{Im}Z$ hereafter) at different steady-state current levels between 2 μA and 10 μA for the midsize VO_2 Mott memristor. We replaced angular frequency ω with frequency f as the x -axis for engineering convenience. Notice that positive and negative frequencies refer to the opposite directions of rotation for the complex exponential $e^{i\omega t}$ vector in the complex plane. $\operatorname{Re}Z$ is an even function of frequency, while $\operatorname{Im}Z$ is an odd function of frequency. At small currents, $\operatorname{Re}Z$ is in the order of $10^5 \Omega$ and shows very weak frequency dependence. Increasing current will “pull” it toward negative direction and develop a dip centered at zero frequency. The higher the current is, the stronger the frequency dependence becomes.

Frequency response of $\operatorname{Re}Z$ shows a dramatic change as current increases from 9 μA to 10 μA . From the pole-zero diagram analysis, we already know that for the midsize VO_2 Mott memristor, the critical current at the LP (lower PDR) to EOC (NDR) crossover is $i_{c1} \approx 9.077 \mu\text{A}$. At $i_Q = 9 \mu\text{A}$, $\operatorname{Re}Z$ still remains positive at any frequency, but its minimum at zero frequency is very close to the origin. At $i_Q = 10 \mu\text{A}$, $\operatorname{Re}Z$ turns negative at frequencies lower than a limit $|f_{\max}| \approx 0.88 \text{ GHz}$, indicating that the element is locally active within certain frequency upper bound. This $(+) \rightarrow (-)$ sign reversal in $\operatorname{Re}Z$ is yet another hallmark of the LP \rightarrow EOC transition, and brings us new information on *the boundary of the EOC region in the frequency domain*.

The value of f_{\max} can be derived from Chua’s fourth LA criterion. For an uncoupled 1D current-driven memristor in the frequency domain, $\operatorname{Re}Z(i\omega; Q) < 0$ for some finite angular frequencies $\omega \in (-\infty, \infty)$ is a sufficient condition for it to be LA. From equation 35, this means $a_0b_0 + a_1b_1\omega^2 < 0$, or $\omega^2 < \frac{-a_0b_0}{a_1b_1}$. Therefore, a 1D uncoupled Mott memristor is locally active if the angular frequency is lower than an upper bound specified as

$$|\omega| < \omega_{\max} = \sqrt{\frac{-a_0b_0}{a_1b_1}} \quad (38)$$

which also requires that $\frac{a_0b_0}{a_1b_1} < 0$ so that ω_{\max} is a real number.

At small currents, $\operatorname{Im}Z$ is both very small and shows very weak frequency dependence. Increasing current will make its amplitude and frequency dependence more substantial. The amplitude of $\operatorname{Im}Z$ first rises quickly with frequency before reaching a peak at a characteristic frequency f_p , then it falls with frequency and approaches the x -axis asymptotically. $|f_p|$ increases with current and reaches 1.51 GHz at $i_Q = 10 \mu\text{A}$. Inset of figure 16(b) is the same frequency dependence of $\operatorname{Im}Z$ plotted in log-log scale, which shows that $\operatorname{Im}Z$ is proportional to frequency for $|f| < |f_p|$ and inversely proportional to frequency for $|f| > |f_p|$.

4.3.1. Nyquist plot It is instructive to plot the locus of $\text{Im}Z(i\omega; Q)$ vs. $\text{Re}Z(i\omega; Q)$ in Cartesian coordinates with ω indicated as a parameter. Such a parametric plot is called a Nyquist plot, which is a graphic technique used to provide intuition on the stability of a dynamical system.

Figure 16(c) shows the loci of Nyquist plot for the same VO_2 device as shown in figure 16(a) and 16(b). Figure 16(d) is a zoomed portion of it to reveal those much smaller loci at $i_Q \leq 7 \mu\text{A}$. Ostensibly, the locus of small-signal $\text{Im}Z(i\omega; Q)$ vs. $\text{Re}Z(i\omega; Q)$ at a finite steady-state current appears to be a circle centered on the x -axis. Increasing current will inflate the radius of the circle and move its center toward the negative direction. Points in the upper half-plane correspond to positive frequencies, and those in the lower half-plane correspond to negative frequencies. Increasing the frequency modulus will move a point in the right direction along the upper or lower arm of the locus. A closer look finds that the left half of the locus intersects the x -axis at zero frequency. For the right half, the distance between the locus and the x -axis approaches 0 as $|f| \rightarrow \infty$, but there is no intersection at any finite frequency. In other words, the x -axis is a horizontal asymptote for the right half of the locus. Therefore the locus of $\text{Im}Z(i\omega; Q)$ vs. $\text{Re}Z(i\omega; Q)$ is actually an open set of points rather than a closed loop. At $i_Q \approx 9.077 \mu\text{A}$, the locus crosses the y -axis into the LHP, as illustrated by the two loci at $9 \mu\text{A}$ and $10 \mu\text{A}$. Therefore, Nyquist plot provides another visualization of the $\text{LP} \rightarrow \text{EOC}$ transition as the steady-state current increases.

Figure 17 is an annotated Nyquist plot for the $\text{Im}Z$ vs. $\text{Re}Z$ locus of the same VO_2 device at $i_Q = 10 \mu\text{A}$, highlighting several key points on the locus. We use the same blue and red colors as shown in figure 14 and figure 15 to represent the LP and EOC regions. Clearly, the lower half of the locus is a reflection of the upper half of it over the x -axis, by negating the values of $\text{Im}Z$ and frequency at the same $\text{Re}Z$ value. The solid dot (\bullet) at $\text{Re}Z \approx -3.17 \times 10^4$ represents the x -intercept of the locus at zero frequency, as indicated by a pair of nearby points at $f = 1 \text{ Hz}$ and $f = -1 \text{ Hz}$. The open circle (\circ) at $\text{Re}Z \approx 9.72 \times 10^4$ represents the x -asymptote of the locus as $|f| \rightarrow \infty$, as indicated by a pair of nearby points at $f = 1 \text{ THz}$ and $f = -1 \text{ THz}$. The two pairs of points at $f = \pm 0.871 \text{ GHz}$ and $f = \pm 0.895 \text{ GHz}$ indicate the crossover from the EOC (red) region to the LP (blue) region as frequency exceeds 0.88 GHz .

4.3.2. Frequency-domain equivalent circuit The frequency-domain equivalent circuit of an isolated Mott memristor can be readily obtained by substituting a_0 , a_1 , b_0 and b_1 in Formula (35) of $Z(i\omega; Q)$ with R_1 , R_2 and C_1 using equations (27)–(30). The real part of $Z(i\omega; Q)$ in Formula (36), now defined as the frequency-domain resistance function, takes the form of

$$R_\omega(\omega, Q) \triangleq \text{Re}Z(i\omega; Q) = \frac{(R_1 + R_2) + (R_1 C_1)^2 R_2 \omega^2}{1 + (R_1 C_1)^2 \omega^2} \quad (39)$$

which can be further rewritten by replacing C_1 with $-1/b_{11}R_1$ using equation (33)

$$R_\omega(\omega, Q) = \frac{b_{11}^2 (R_1 + R_2) + R_2 \omega^2}{b_{11}^2 + \omega^2} \quad (40)$$

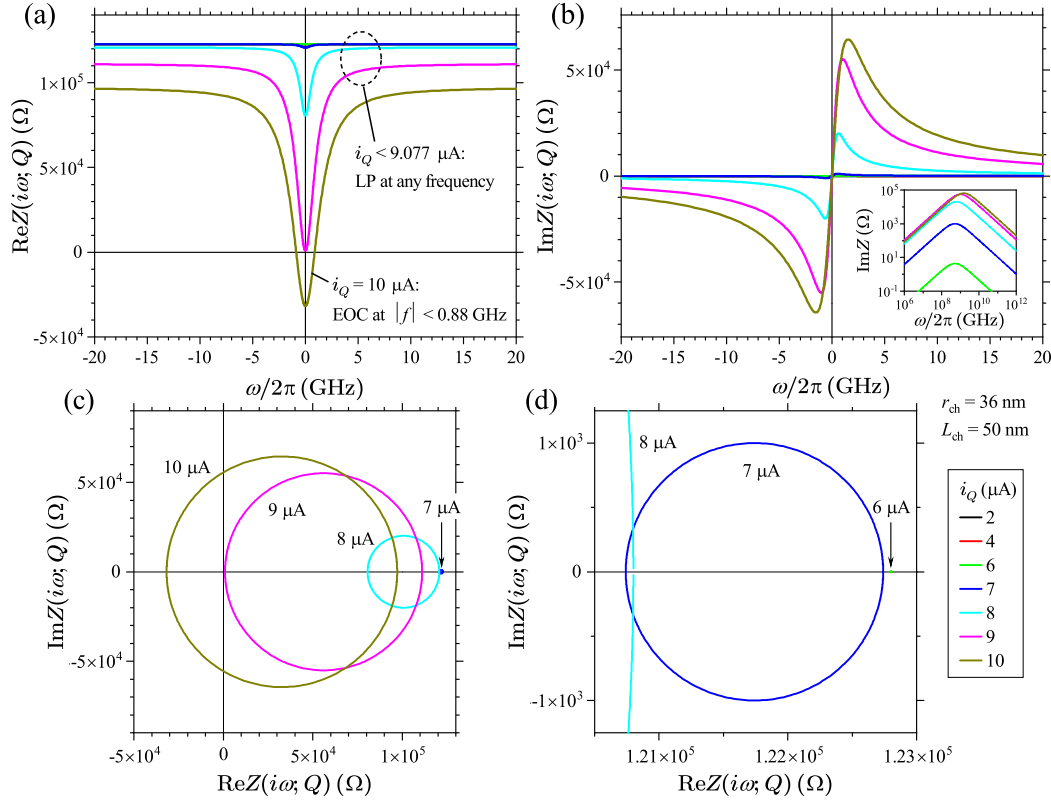


Figure 16: Small-signal impedance $Z(i\omega; Q)$ frequency response of the midsize VO₂ Mott memristor biased at constant steady-state currents in the range of 2 μA to 10 μA. (a) $\text{Re}Z(i\omega; Q)$ vs. $\omega/2\pi$ (in GHz). At $i_Q < 9.077 \mu\text{A}$, $\text{Re}Z > 0$ at any frequency and the memristor remains LP. At $i_Q = 10 \mu\text{A}$, an EOC region exists with $\text{Re}Z < 0$ at $|f| < 0.88$ GHz. (b) $\text{Im}Z(i\omega; Q)$ vs. $\omega/2\pi$. Inset is a part of the same figure plotted in log-log scale. (c) Nyquist plot $\text{Im}Z(i\omega; Q)$ vs. $\text{Re}Z(i\omega; Q)$. (d) Zoomed portion of (c) to reveal the loci at smaller currents.

The sign of $R_\omega(\omega, Q)$ can be either positive or negative, depending on the (ω, Q) coordinate. $R_\omega(\omega, Q) \geq 0$ maps to the LP region, and $R_\omega(\omega, Q) < 0$ maps to the EOC region. The angular frequency formula (38) to satisfy Chua's fourth LA criterion now becomes

$$|\omega| < \omega_{\max} = -b_{11} \sqrt{\frac{-(R_1 + R_2)}{R_1}} \quad (41)$$

Since the memristance R_2 is always positive, this indicates that $(R_1 + R_2)$ must be negative for ω_{\max} to be a real number. From the previous discussion of figure 11(d), $(R_1 + R_2) < 0$ maps into the NDR (EOC) region on the steady-state (i_Q, v_Q) locus.

We now look at the imaginary part of $Z(i\omega; Q)$. By substituting a_0 , a_1 , b_0 and b_1 in Formula (37) of $\text{Im}Z(i\omega; Q)$ with R_1 , R_2 and C_1 , we rewrite $\text{Im}Z(i\omega; Q)$ as

$$\text{Im}Z(i\omega; Q) \triangleq L_\omega(\omega, Q)\omega = \left[\frac{-R_1^2 C_1}{1 + (R_1 C_1)^2 \omega^2} \right] \omega \quad (42)$$

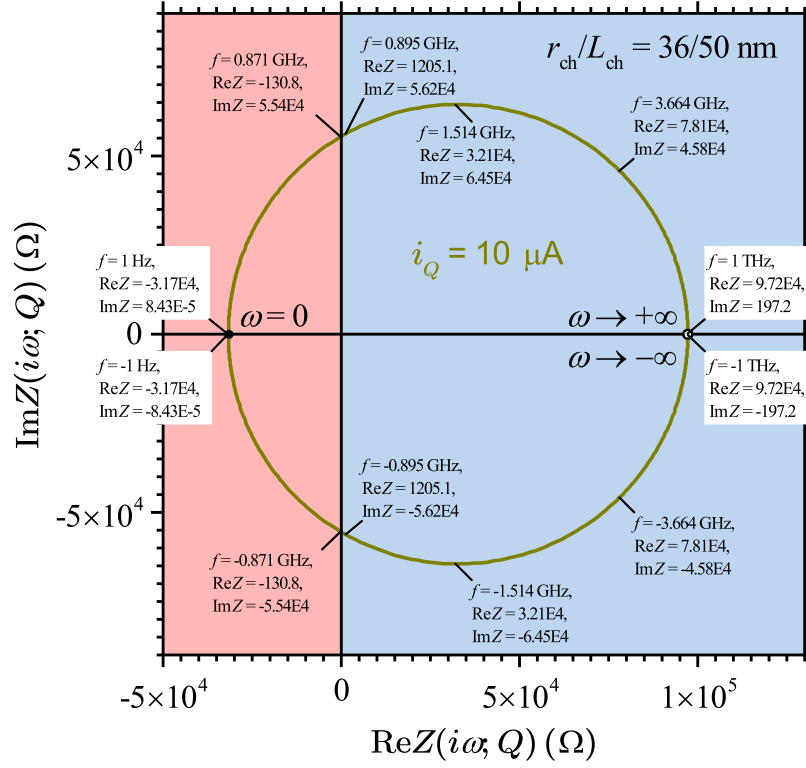


Figure 17: Nyquist plot $\text{Im}Z(i\omega; Q)$ vs. $\text{Re}Z(i\omega; Q)$ of the midsize VO_2 Mott memristor at a constant steady-state current $i_Q = 10 \mu\text{A}$. The LP and EOC regions are highlighted by blue and red colors, respectively.

where $L_\omega(\omega, Q)$ is defined as the frequency-domain inductance function. Evidently, the sign of $L_\omega(\omega, Q)$ is determined by the sign of C_1 . Since C_1 remains negative at any fixed point Q (see discussion on figure 11(c)), $L_\omega(\omega, Q)$ is always positive, regardless of the location of Q in the LP or EOC region. Therefore, *the frequency-domain reactance of an isolated Mott memristor is always inductive*, causing its voltage output to lead a sinusoidal current input in phase. $\text{Im}Z(i\omega; Q)$ can be further rewritten by replacing C_1 with $-1/b_{11}R_1$

$$L_\omega(\omega, Q)\omega = \left(\frac{b_{11}R_1}{b_{11}^2 + \omega^2} \right) \omega \quad (43)$$

Finally, the frequency-domain small-signal impedance function is expressed as

$$Z(i\omega; Q) = R_\omega(\omega, Q) + iL_\omega(\omega, Q)\omega \quad (44)$$

Therefore, in frequency domain one can treat an uncoupled Mott memristor as a positive inductor in series with a resistor that is negative up to certain maximum frequency (the EOC region) and positive beyond it (the LP region) [64].

4.3.3. Phase diagram for complexity The fourth criterion in Chua's LA theorem tells that a negative real part of the complexity function of an uncoupled 1D circuit element

at some finite frequencies is a sufficient condition for it to be locally active. For a current-driven memristor, its complexity function is the impedance function $Z(i\omega; Q)$. Since $Z(i\omega; Q)$ depends on both the angular frequency ω and the steady-state current i_Q , plotting $\text{Re}Z$ as a color scale with current and frequency as the (x, y) coordinate provides a visualization of the LP and EOC regions in the operating parameter space. The $\text{Re}Z = 0$ contour outlines the border between them. One could call such a 2D graphical representation of $\text{Re}Z$ a *phase diagram for complexity*.

In figure 18, we plot the 2D color scale map of $\text{Re}Z(i_Q, f)$ for the midsize VO_2 Mott memristor. Figure 18(a) is the low-current region of it plotted up to $20.8 \mu\text{A}$. It shows that at lower frequencies, the LP \rightarrow EOC transition occurs at a nearly frequency-independent critical current $i_{c1} \approx 9.077 \mu\text{A}$, as indicated by an almost vertical $\text{Re}Z = 0$ contour. At frequencies higher than $\sim 0.88 \text{ GHz}$, the critical current increases drastically, consequently the direction of the $\text{Re}Z = 0$ contour turns almost parallel to the current axis. Figure 18(b) is the same color scale $\text{Re}Z$ map with a much wider current range up to 2 mA , revealing an EOC \rightarrow LP transition that occurs at a nearly constant critical current $i_{c2} \approx 971.18 \mu\text{A}$ at low frequencies. The direction of the $\text{Re}Z = 0$ contour shows a similar crossover from nearly vertical at frequencies lower than $\sim 0.88 \text{ GHz}$ to almost horizontal at higher frequencies.

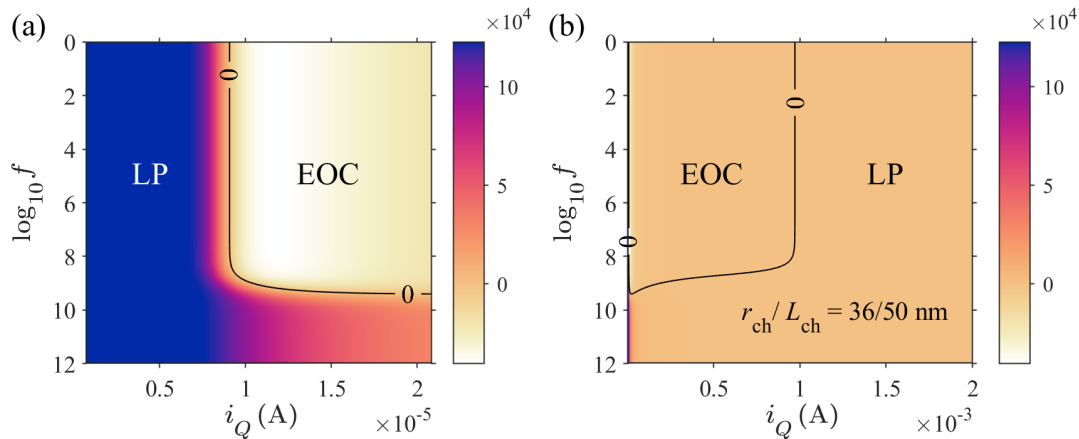


Figure 18: 2D color scale map of $\text{Re}Z(i_Q, f)$ for the midsize VO_2 Mott memristor as a visualization of the LP and EOC regions in the frequency and current parameter space, showing (a) the low-current region of it up to $i_Q = 20.8 \mu\text{A}$, and (b) a wide-range map plotted up to $i_Q = 2 \text{ mA}$. Frequencies are plotted in logarithmic scale.

To understand the scaling trend of the local activity region versus the device size, we plotted the 2D color scale map of $\text{Re}Z(i_Q, f)$ for VO_2 Mott memristors with different combinations of r_{ch} and L_{ch} sizes. Figure 19 shows the main results of this exercise. We found that $\text{Re}Z$ is independent of the VO_2 channel length L_{ch} . This is not unexpected since the VO_2 compact model is essentially 2D in nature. Figure 19(a) is a zoomed view of the $\text{Re}Z = 0$ contours for VO_2 devices with r_{ch} in the range of $5\text{--}60 \text{ nm}$. The shaded area under each contour is the EOC region that satisfies $\text{Re}Z(i_Q, f) < 0$. The apex of each contour corresponds to the maximum frequency f_{max} for the device to

remain locally active. Figure 19(b) shows that f_{\max} increases super-exponentially as the VO₂ channel radius r_{ch} shrinks down. For a VO₂ device with r_{ch} as small as 5 nm, f_{\max} reaches as high as 132.1 GHz. This is a favorable device scaling in the sense of operation bandwidth for using Mott memristors as locally active components. It also reveals that the steady-state current at f_{\max} is directly proportional to the radius of the conduction channel r_{ch} .

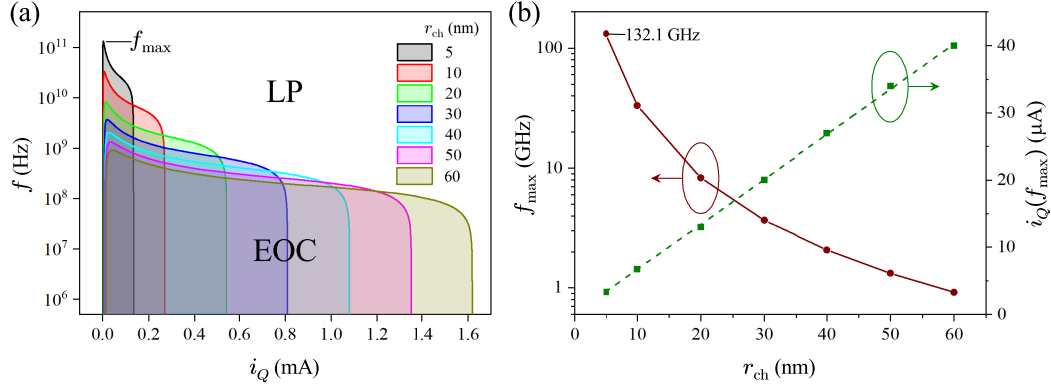


Figure 19: (a) A zoomed view of the $\text{Re}Z = 0$ contours for VO₂ Mott memristors with channel radius r_{ch} in the range of 5 nm to 60 nm. Shaded areas under the contours are the EOC regions wherein $\text{Re}Z(i_Q, f) < 0$. The apex of each contour at $f = f_{\max}$ shows the maximum frequency of the EOC region. (b) Scaling of f_{\max} (brown) and $i_Q(f_{\max})$ (green) vs. r_{ch} . f_{\max} increases super-exponentially as r_{ch} decreases. $i_Q(f_{\max})$ scales linearly with r_{ch} . A linear regression (dashed line) returns a slope of 671 ± 3 (A/m) and coefficient of determination $R^2 = 0.99988$.

5. Local analysis of reactively-coupled Mott memristors: 2D relaxation oscillator

The topological constraint for an isolated 1D Mott memristor limits the dynamics it can describe. It is impossible to exhibit damped or persistent oscillations. However, the topological constraint is lifted once it is coupled to one or more reactive elements, which increases the dimension of the system as a whole and the complexity in dynamics. For continuous dynamical systems, the Poincaré–Bendixson theorem says that chaos only arises in three or more dimensions.

For simplicity, we will limit our discussions to 2D cases. Experimentally, it is difficult to characterize an isolated memristor without inadvertently coupling it to one or more reactive elements. On the other hand, such couplings introduce interesting phenomena such as self-excited persistent oscillations or stable limit cycles. Limit cycles belong to an important category of attractors besides fixed points. A nonlinear system consisting of a Mott memristor coupled with reactive elements may exhibit a *local* Hopf-like bifurcation. As a bifurcation parameter is varied, its local stability abruptly switches between a fixed point and a limit cycle around it. Persistent oscillations that arise out

of Hopf-like bifurcations are well studied in the Hodgkin-Huxley and FitzHugh-Nagumo models of biological nerve cells [65–68], and they are relevant for the intriguing neuronal signaling phenomena such as firing of action potentials. However, finding the limit cycle solutions for a dynamical system is generally a very difficult mathematical problem. The unsolved second part of Hilbert’s 16th problem is a famous example. The local analysis techniques that we have discussed so far are not sufficient, and one needs to resort to global nonlinear techniques such as nullcline analysis and Lyapunov stability theory. In this section, we apply local analysis to a simple example of a reactively-coupled Mott memristor. Then in the next section we take a cursory glance at global analysis using the same example to illustrate its usefulness.

5.1. Voltage-biased relaxation oscillator circuit

A voltage-biased Pearson–Anson relaxation oscillator circuit is a simple yet very useful example to illustrate the effect of such external couplings. As shown in figure 20, if a Mott memristor M is connected to a capacitor C_p in parallel, and both of them are connected to a resistor R_s placed in series, then together they form a composite circuit which can be represented as $\{(M//C_p) + R_s\}$. In practice, one may inadvertently form such a circuit when attempting to test an individual memristor device without explicitly connecting C_p and R_s . C_p may come from the geometric capacitance between the two electrodes of a thin-film metal-oxide-metal device, or stray capacitance of coaxial cables. R_s may arise from the output resistance of a voltage source, resistance of metal lead wires, and contact resistance at the metal-oxide interfaces. If a DC voltage bias V_{dc} is applied to one terminal of R_s , and the other terminal of R_s connected to the memristor is taken as the output node, the $\{(M//C_p) + R_s\}$ circuit forms a Pearson–Anson (PA) or relaxation oscillator. If the passive elements and voltage bias are appropriately valued, it exhibits persistent self-excited oscillations that will be elaborated below.

5.2. Small-signal analysis: the element combination approach

The $\{(M//C_p) + R_s\}$ Mott memristor PA circuit is a second-order system with two state variables: charge q_C stored in the capacitor C_p (or equivalently voltage v across C_p and M), and fraction of metallic phase x in the memristor M . This second-order system is described by two coupled differential equations. Its steady states or fixed points can be found by the global nullcline method, which will be covered in the next section. For the sake of continuity in discussion, we assume that fixed points of the PA oscillator are already solved, and focus on what can be told by local analysis for the moment. We can combine $(M//C_p)$ into a composite second-order nonlinear element (dashed box in figure 20), then apply the small-signal local analyses and Chua’s LA criteria to the system consisting of the composite element in series with R_s .

To perform small-signal analysis, we first need to find out the transfer function of the composite circuit. In the s domain, impedance of a capacitor C_p is $1/sC_p$ if assuming an initial condition $v(0) = 0$. Impedance M in its pole-zero form is $Z_M(s; Q) = \frac{k(s-z)}{(s-p)}$

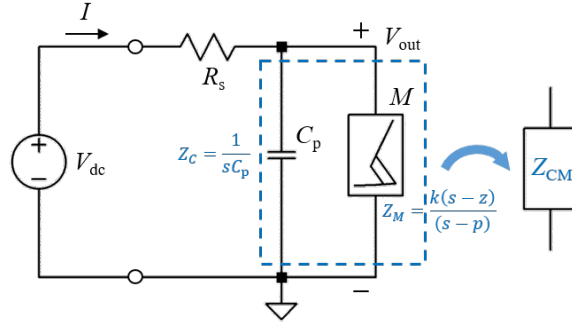


Figure 20: Circuit diagram of a DC voltage biased Pearson-Anson relaxation oscillator formed by a Mott memristor M in parallel with a capacitor C_p , and both connected in series with a resistor R_s . Formulas in blue are the s -domain impedances of M and C_p (with an initial condition $v(0) = 0$) used to derive the total impedance Z_{CM} .

(equation 31). One can derive the transfer function $H(s; Q)$ of the PA oscillator about a fixed point Q using the voltage divider formula

$$H(s; Q) = V_{\text{out}}/V_{\text{dc}} = Z_{CM}/(R_s + Z_{CM}) \quad (45)$$

where Z_{CM} is the total impedance of C_p in parallel with M

$$Z_{CM} = Z_C Z_M / (Z_C + Z_M) = \frac{k(s-z)}{kC_p s^2 + (1 - kC_p z)s - p} \quad (46)$$

Substituting the expression of Z_{CM} in the transfer function formula, we get

$$H(s; Q) = \frac{k(s-z)}{kR_s C_p s^2 + (R_s + k - kR_s C_p z)s - (R_s p + kz)} \quad (47)$$

One can see that $H(s; Q)$ of a Mott memristor PA oscillator has the same zero as an uncoupled memristor, but it has a pair of two poles instead of one pole for an uncoupled memristor.

To simplify the expression of $H(s; Q)$, we define a time constant $\tau_0 \triangleq R_s C_p$ and a cutoff frequency $\omega_0 \triangleq (R_s C_p)^{-1}$. We also substitute k by the positive real memristance function R_{ch} , and rewrite $H(s; Q)$ in the pole-zero form

$$H(s; Q) = \frac{k'(s-z)}{d_2 s^2 + d_1 s + d_0} = \frac{k'(s-z)}{(s-p_+)(s-p_-)} \quad (48)$$

where

$$k' = \omega_0 \quad (49)$$

$$d_2 = 1 \quad (50)$$

$$d_1 = \frac{R_s + R_{\text{ch}} - R_{\text{ch}}\tau_0 z}{R_{\text{ch}}\tau_0} = \left(1 + \frac{R_s}{R_{\text{ch}}}\right)\omega_0 - z \quad (51)$$

$$d_0 = \frac{-(R_s p + R_{\text{ch}} z)}{R_{\text{ch}}\tau_0} = -\frac{R_s}{R_{\text{ch}}}\omega_0 p - \omega_0 z \quad (52)$$

Here p and z are the pole and zero of the memristor M . We then derive the pair of poles p_{\pm} for the PA oscillator by finding the roots of the quadratic equation $d_2s^2 + d_1s + d_0 = 0$

$$p_{\pm} = \frac{-d_1 \pm \sqrt{d_1^2 - 4d_2d_0}}{2d_2} = \frac{-d_1 \pm \sqrt{d_1^2 - 4d_0}}{2} \quad (53)$$

The discriminant $d_1^2 - 4d_2d_0$ of the quadratic equation is expressed as

$$d_1^2 - 4d_2d_0 = z^2 + 2\omega_0z \left(1 - \frac{R_s}{R_{ch}}\right) + \left(1 + \frac{R_s}{R_{ch}}\right)^2 \omega_0^2 + 4\omega_0p \left(\frac{R_s}{R_{ch}}\right) \quad (54)$$

If $d_1^2 - 4d_2d_0 \geq 0$, p_{\pm} are positive or negative real numbers. Otherwise if $d_1^2 - 4d_2d_0 < 0$, p_{\pm} are a complex conjugate pair. Without loss of generality, here we keep the standard expression for the discriminant of a quadratic equation instead of replacing d_2 with 1 (equation (50)) for the particular case of a Mott memristor PA circuit.

To understand the effects of parameters R_s , C_p and V_{dc} on the dynamical behavior of a Mott memristor PA oscillator, we first calculated the values for the pair of poles p_{\pm} of its small-signal transfer function $H(s; Q)$, by varying one parameter while fixing the other two parameters, then applied the parametric Nyquist plot technique to gain intuition on the stability of the reduced system.

Let us first examine the effect of varying R_s while fixing C_p and V_{dc} . Figure 21(a) shows Nyquist plot of $\text{Im}(p_{\pm})$ vs. $\text{Re}(p_{\pm})$ for the midsize VO_2 Mott memristor PA oscillator with $C_p = 1$ pF, $V_{dc} = 1.2$ V, and R_s stepped from 100 Ω to 27 k Ω at 100 Ω interval. It reveals three distinctive regions as R_s increases: (1) $R_s = 100 \Omega - 200 \Omega$, p_+ and p_- are negative real numbers. (2) $R_s = 300 \Omega - 7.5$ k Ω , p_+ and p_- are a complex conjugate pair. (3) $R_s = 7.6$ k $\Omega - 27$ k Ω , p_+ and p_- are positive real numbers. Figure 21(b) is a zoomed view of figure 19(a), which reveals that increasing R_s from 3.3 k Ω to 3.4 k Ω flips the sign of $\text{Re}(p_{\pm})$ from negative to positive, i.e., the pair of poles crosses over from LHP to RHP. If we treat the reduced system as a 1D uncoupled element, and apply the first criterion of Chua's LA theorem — the element is locally active if $H(s; Q)$ has a pole in the open RHP $\text{Re}(s) > 0$, then the reduced system has a crossover from LP to LA as R_s increases from 3.3 k Ω to 3.4 k Ω .

A similar crossover is observed by varying V_{dc} while fixing R_s and C_p . Figure 21(c) shows Nyquist plot of $\text{Im}(p_{\pm})$ vs. $\text{Re}(p_{\pm})$ for the midsize VO_2 Mott memristor PA oscillator with $R_s = 3.4$ k Ω , $C_p = 1$ pF, and V_{dc} stepped from 0.55 V to 13.5 V at 50 mV interval. It reveals two distinctive regions as V_{dc} increases: (1) $V_{dc} = 0.55$ V – 0.65 V, p_+ and p_- are positive real numbers. (2) $V_{dc} = 0.7$ V – 13.5 V, p_+ and p_- are a complex conjugate pair. Figure 21(d) is a zoomed view of figure 21(c), which reveals that increasing V_{dc} from 1.2 V to 1.25 V flips the sign of $\text{Re}(p_{\pm})$ from positive to negative, i.e., the pair of poles crosses over from RHP to LHP. Applying the first criterion of Chua's LA theorem in a similar manner, then the reduced system has a crossover from LA to LP as V_{dc} increases from 1.2 V to 1.25 V.

Instead of using the sign of $\text{Re}(p_{\pm})$ in the Cartesian coordinate as a test for the first LA criterion, one can also use the argument (phase) of a pole in the polar coordinate.

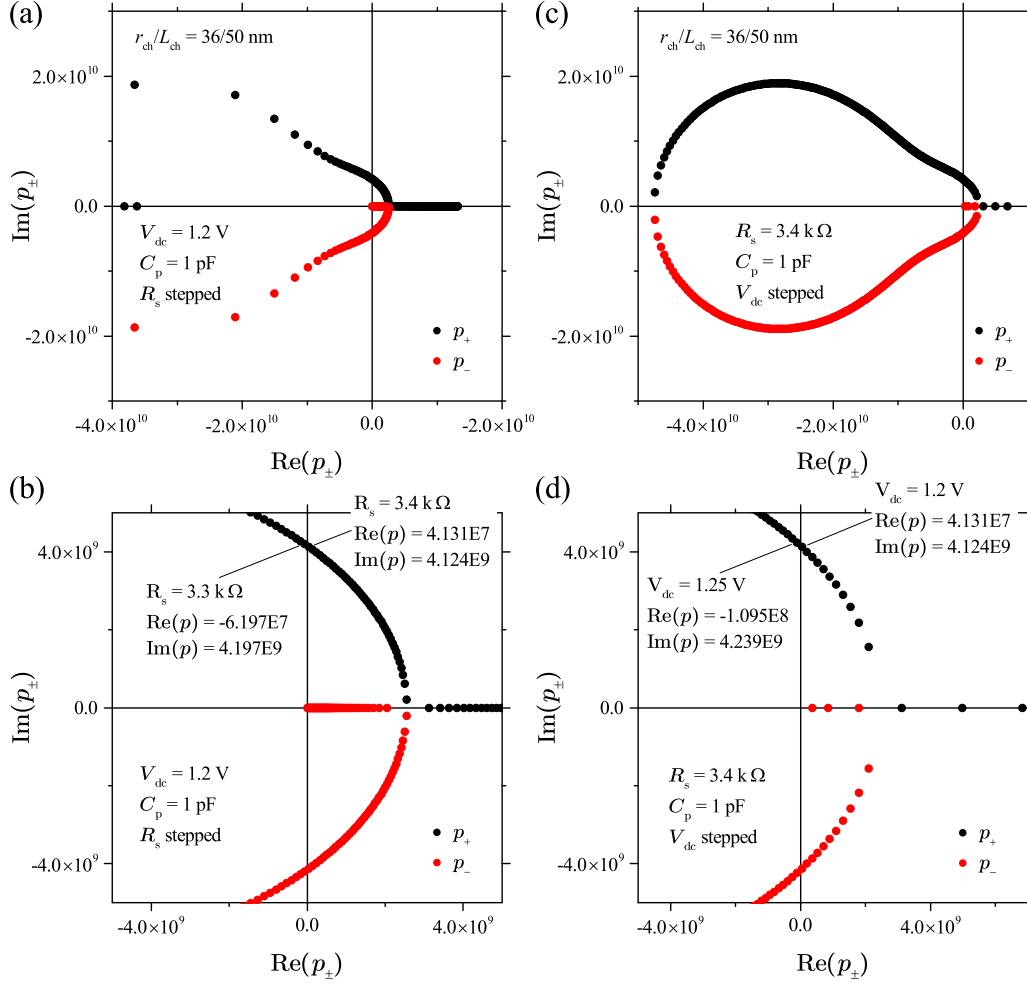


Figure 21: (a) Nyquist plot of $\text{Im}(p_{\pm})$ vs. $\text{Re}(p_{\pm})$ for the pair of poles p_{\pm} of the small-signal transfer function $H(s; Q)$ of the midsize VO_2 Mott memristor PA oscillator with $C_p = 1 \text{ pF}$, $V_{\text{dc}} = 1.2 \text{ V}$, and R_s stepped from 100Ω to $27 \text{ k}\Omega$ at 100Ω interval. (b) is a zoomed view of (a), showing that increasing R_s from $3.3 \text{ k}\Omega$ to $3.4 \text{ k}\Omega$ turns $\text{Re}(p_{\pm})$ from negative to positive. (c) Nyquist plot of the same PA oscillator with $R_s = 3.4 \text{ k}\Omega$, $C_p = 1 \text{ pF}$, and V_{dc} stepped from 0.55 V to 13.5 V at 50 mV interval. (d) is a zoomed view of (c), showing that increasing V_{dc} from 1.2 V to 1.25 V turns $\text{Re}(p_{\pm})$ from positive to negative.

The p_+ pole is located in the first and second quadrants, including the Re and Im+ axes. Its complex conjugate p_- is located in the third and fourth quadrants, including the Re and Im− axes. We only need to look at $\arg(p_+)$, argument of the p_+ pole of $H(s; Q)$, as a test for the first LA criterion. A crossover from LA to LP occurs if $\arg(p_+)$ increases from below 90° to above 90° , i.e., p_+ moves from the first quadrant to the second quadrant by crossing the Im+ axis.

At a fixed C_p parameter, one can thus visualize the LA and LP operating regions of a Mott memristor PA oscillator by plotting a 2D color scale map of $\arg(p_+)$ with R_s and V_{dc} parameters as the x and y coordinates. The procedure is then repeated at different C_p values to see how the LA and LP regions evolve as C_p is adjusted. Figure

22 shows four 2D color scale maps of $\arg(p_+)$ for the midsize VO₂ Mott memristor PA oscillator at $C_p = 0.1$ pF (a), 1 pF (b), 10 pF (c) and 100 pF (d), respectively.

We take figure 22(a) as an example to discuss their common characteristics. From the complex domain aspect, $\arg(p_+)$ has three distinctive regions if one navigates along the top-right to bottom-left diagonal. At small V_{dc} and large R_s (the top-right pink region), $\arg(p_+) = 0^\circ$, p_+ is a positive real number on the Re+ axis. At larger V_{dc} and smaller R_s , p_+ is a complex number (the middle colored region) in either the first quadrant (LA) or the second quadrant (LP), divided by the 90° contour line. At even larger V_{dc} and smaller R_s , $\arg(p_+) = 180^\circ$, p_+ is a negative real number on the Re- axis. A conspicuous feature is that all the borderlines between adjacent regions are straight lines that extend from top-left to bottom-right. Despite their appearance, they do not intersect at a common point if extrapolated toward the top-left direction. From the dynamics aspect, there are only two regions, the LA region ($\text{Re}(p_+) > 0$) and the LP region ($\text{Re}(p_+) < 0$) separated by the 90° contour line.

The effect of C_p can be seen by comparing the four color scale maps. As C_p increases from 0.1 pF to 10 pF, the 90° LA-LP borderline rotates clockwise, the rotation stalls as C_p further increases to 100 pF. The $\arg(p_+) = 0^\circ$ (positive real) region at the top right corner continuously grows with increase in C_p , while the complex region shrinks with increase in C_p . The $\arg(p_+) = 180^\circ$ (negative real) region at the bottom left corner initially shrinks significantly as C_p increases from 0.1 pF to 1 pF, then it recovers a little as C_p further increases.

Using the element combination approach, one can also examine the case of an inductively coupled Mott memristor, e.g., connecting an external inductor in parallel with a Mott memristor. It is found that the poles of the transfer function of such a composite circuit remain in the LHP, thus the composite circuit does not meet the LA criterion to exhibit instabilities or persistent oscillations [40]. This is not surprising since an isolated Mott memristor has an apparent inductive reactance.

5.3. Jacobian matrix method

For second or higher order nonlinear systems, the Jacobian matrix method is a linearization technique that allows local stability analysis near a hyperbolic fixed point. As an introduction in a nutshell, consider an autonomous system of ODEs $\dot{\mathbf{x}} = \mathbf{f}(\mathbf{x})$, where $\dot{\mathbf{x}}$ is the component-wise time derivative for the set of state variables \mathbf{x} . \mathbf{x} corresponds to a point in an open subset of real n -space $E \subset \mathbb{R}^n$. $\mathbf{f} : E \rightarrow \mathbb{R}^n$ is a differentiable function that describes the dynamics of \mathbf{x} . \mathbf{f} is also called a vector field, since mapping from \mathbf{x} to $\mathbf{f}(\mathbf{x})$ assigns a vector. For a 2D (planar) system described by $\frac{dx}{dt} = f(x, y)$ and $\frac{dy}{dt} = g(x, y)$, $\mathbf{f}(\mathbf{x}) = (f(x, y), g(x, y))$ can be visualized by a vector based at the point (x, y) , whose x - and y -components are $f(x, y)$ and $g(x, y)$, respectively. The set of solutions $\phi(t, \mathbf{x}_0)$ of the initial value problem $\dot{\mathbf{x}} = \mathbf{f}(\mathbf{x})$, $\mathbf{x}(0) = \mathbf{x}_0 \in E$ is called the flow of the ODE, or the flow of the vector field \mathbf{f} . For each initial condition \mathbf{x}_0 , $\phi(t, \mathbf{x}_0)$ gives the trajectory of a unique solution of the ODE, which is called the

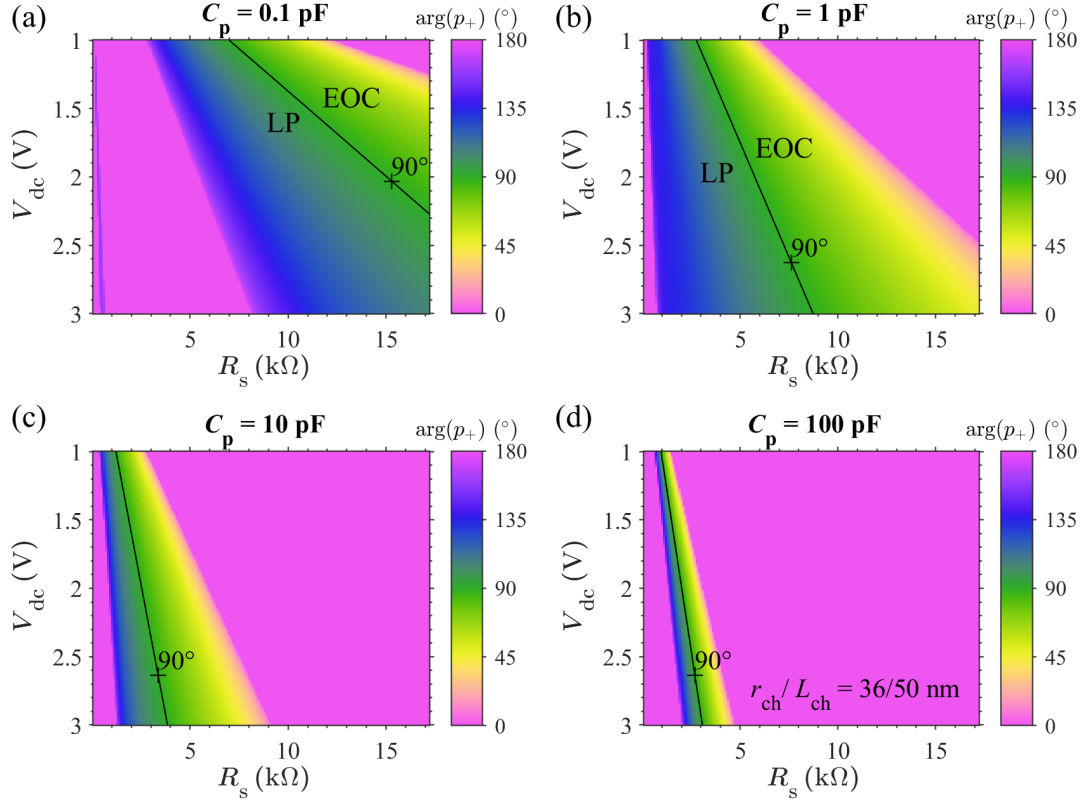


Figure 22: 2D color scale maps of $\arg(p_+)(R_s, V_{dc})$, argument of the p_+ pole of $H(s; Q)$ with R_s and V_{dc} as the x and y coordinates, for the midsize VO₂ Mott memristor PA oscillator at (a) $C_p = 0.1$ pF, (b) $C_p = 1$ pF, (c) $C_p = 10$ pF and (d) $C_p = 100$ pF, respectively. In each plot, the LA region ($\text{Re}(p_+) > 0$) and the LP region ($\text{Re}(p_+) < 0$) are separated by the 90° contour line (solid black line marked by “+”). We use a cyclic color map with four distinct colors to allow four orientations or phase angles to be visualized. Both $\arg(p_+) = 0^\circ$ and $\arg(p_+) = 180^\circ$ are shown with the same color (pink).

orbit of \mathbf{x} under ϕ .

In autonomous systems, \mathbf{f} does not explicitly depend on time. If $\mathbf{f}(\mathbf{x}_Q) = 0$, i.e., its time derivative is zero, then \mathbf{x}_Q is a fixed point. The Jacobian matrix $D\mathbf{f}$, or simply Jacobian, is the matrix of all the first-order partial derivatives of $\mathbf{f}(\mathbf{x})$. The Hartman–Grobman theorem and the stable manifold theorem guarantee that the local qualitative behavior of a nonlinear system $\dot{\mathbf{x}} = \mathbf{f}(\mathbf{x})$ near a hyperbolic fixed point \mathbf{x}_Q is determined by a linear system $\dot{\mathbf{x}} = A\mathbf{x}$, where $A = D\mathbf{f}(\mathbf{x}_Q)$ is the Jacobian of \mathbf{f} at \mathbf{x}_Q . In other words, the flow of a nonlinear system is topologically conjugate to that of its linearized system in some neighborhood of a fixed point, so long as it is hyperbolic. If the Jacobian is a square matrix, and none of the eigenvalues of $D\mathbf{f}(\mathbf{x}_Q)$ is a pure imaginary number, then the fixed point is hyperbolic, and its stability can be told by the signs of the real parts of the eigenvalues, as will be elaborated later.

Next, we take the Jacobian matrix approach to analyze the local stability of a Mott memristor PA oscillator. This second-order system is described by the following

equations

$$v = R_{\text{ch}}(x)i_{\text{M}} \quad (55)$$

$$\frac{dx}{dt} = f_x(x, i_{\text{M}}) \quad (56)$$

$$\frac{dv}{dt} = \frac{1}{C_{\text{p}}} \left(\frac{V_{\text{dc}} - v}{R_{\text{s}}} - i_{\text{M}} \right) \quad (57)$$

where $f_x(x, i_{\text{M}})$ and $R_{\text{ch}}(x)$ are the kinetic function and memristance function of the memristor M , respectively. i_{M} is the current flowing through M . Substituting it with $v/R_{\text{ch}}(x)$, we obtain the two coupled ODEs that describe the system dynamics

$$\frac{dx}{dt} \triangleq f(x, v) = f_x \left(x, \frac{v}{R_{\text{ch}}(x)} \right) \quad (58)$$

$$\frac{dv}{dt} \triangleq g(x, v) = \frac{1}{C_{\text{p}}} \left(\frac{V_{\text{dc}} - v}{R_{\text{s}}} - \frac{v}{R_{\text{ch}}(x)} \right) \quad (59)$$

In a vector form, the system is described as $\dot{\mathbf{x}} = \mathbf{f}(\mathbf{x})$. Here $\dot{\mathbf{x}} = [x, v]^{\text{T}}$ is the state variable vector, and $\mathbf{f}(\mathbf{x}) = [f(x, v), g(x, v)]^{\text{T}}$ is the differentiable function that describes the dynamics of \mathbf{x} . Around a fixed point Q with a coordinate (x_Q, v_Q) , the Jacobian matrix $D\mathbf{f}$ of the system is a 2×2 matrix of all the first-order partial derivatives of $\mathbf{f}(\mathbf{x})$ that takes the form

$$D\mathbf{f}|_Q = \begin{bmatrix} \xi_{11} & \xi_{12} \\ \xi_{21} & \xi_{22} \end{bmatrix} = \begin{bmatrix} \left. \frac{\partial f(x, v)}{\partial x} \right|_Q & \left. \frac{\partial f(x, v)}{\partial v} \right|_Q \\ \left. \frac{\partial g(x, v)}{\partial x} \right|_Q & \left. \frac{\partial g(x, v)}{\partial v} \right|_Q \end{bmatrix} \quad (60)$$

The four elements of the Jacobian matrix are derived as

$$\xi_{11} = \left. \frac{\partial f(x, v)}{\partial x} \right|_Q = b_{11}(Q) - \frac{b_{12}(Q)a_{11}(Q)}{R_{\text{ch}}(x_Q)} \quad (61)$$

$$\xi_{12} = \left. \frac{\partial f(x, v)}{\partial v} \right|_Q = \frac{b_{12}(Q)}{R_{\text{ch}}(x_Q)} \quad (62)$$

$$\xi_{21} = \left. \frac{\partial g(x, v)}{\partial x} \right|_Q = \frac{a_{11}(Q)}{R_{\text{ch}}(x_Q)C_{\text{p}}} \quad (63)$$

$$\xi_{22} = \left. \frac{\partial g(x, v)}{\partial v} \right|_Q = - \left(\frac{1}{R_{\text{s}}C_{\text{p}}} + \frac{1}{R_{\text{ch}}(x_Q)C_{\text{p}}} \right) \quad (64)$$

The eigenvalues of the Jacobian around a fixed point Q are calculated by solving its characteristic equation that can be expanded to a quadratic polynomial.

$$(D\mathbf{f} - \lambda I)|_Q = \lambda^2 - \text{tr}(D\mathbf{f})\lambda + \det(D\mathbf{f}) = \lambda^2 - (\xi_{11} + \xi_{22})\lambda + (\xi_{11}\xi_{22} - \xi_{12}\xi_{21}) \quad (65)$$

where I is the identity matrix. $\text{tr}(D\mathbf{f})$ is the trace of the Jacobian and $\det(D\mathbf{f})$ is the determinant of it. For simplicity, we use tr and \det to represent them hereafter. Their

expressions are derived as

$$\text{tr} = - \left[\omega_1 \left(1 + \frac{R_1}{R_{\text{ch}}} \right) + \omega_0 \left(1 + \frac{R_s}{R_{\text{ch}}} \right) \right] \quad (66)$$

$$\text{det} = \omega_1 \omega_0 \left(1 + \frac{R_1}{R_{\text{ch}}} + \frac{R_s}{R_{\text{ch}}} \right) \quad (67)$$

where we define another cutoff frequency $\omega_1 \triangleq (R_1 C_1)^{-1}$ besides the previously defined cutoff frequency $\omega_0 = (R_s C_p)^{-1}$ to simplify the expressions.

The two roots λ_+ and λ_- of the characteristic equation are

$$\lambda_{\pm} = \frac{\text{tr} \pm \sqrt{\text{tr}^2 - 4 \text{det}}}{2} \quad (68)$$

Note that $\lambda_+ + \lambda_- = \text{tr}$ and $\lambda_+ \lambda_- = \text{det}$, i.e., trace is the sum of eigenvalues, and determinant is the product of them. The discriminant $\text{tr}^2 - 4 \text{det}$ of the characteristic equation in expanded form is

$$\text{tr}^2 - 4 \text{det} = \omega_1^2 (1 + \gamma_1)^2 + \omega_0^2 (1 + \gamma_s)^2 - 2\omega_1 \omega_0 [(1 - \gamma_1)\gamma_s + (1 + \gamma_1)] \quad (69)$$

where we define two dimensionless resistance ratios $\gamma_1 \triangleq \frac{R_1}{R_{\text{ch}}}$ and $\gamma_s \triangleq \frac{R_s}{R_{\text{ch}}}$ to simplify the expression.

5.4. Trace-determinant plane classification

For a 2D homogeneous linear system $\dot{\mathbf{x}} = \mathbf{A}\mathbf{x}$, the parameter space of a trace-determinant (tr-det) plane allows qualitative classification of its fixed points. Here a homogeneous linear system is defined in opposition to a nonhomogeneous linear system $\dot{\mathbf{x}} = \mathbf{A}\mathbf{x} + \mathbf{h}(t)$ that includes a vector of functions $\mathbf{h}(t)$ independent of solutions and their derivatives. For a 2D nonlinear system after linearization, one needs to be cautious when attempting the tr-det plane method, since linearization may change the type of its fixed points, especially at the borderlines on the tr-det plane. Here we examine the tr-det plane method on a linearized Mott memristor PA oscillator to see if one can gain some insight into the original nonlinear system.

In a tr-det plane, a coordinate (tr, det) corresponds to a Jacobian matrix with trace tr and determinant det. The location of this point relative to the parabola curve $\text{tr}^2 - 4 \text{det} = 0$ determines the geometry of the phase portrait. The sign of the discriminant $\text{tr}^2 - 4 \text{det}$ divides the eigenvalues of $D\mathbf{f}$ into the following regions.

- a) If $\text{tr}^2 - 4 \text{det} > 0$, λ_+ and λ_- are real and distinct
- b) If $\text{tr}^2 - 4 \text{det} < 0$, λ_+ and λ_- are complex conjugates with nonzero imaginary part
- c) If $\text{tr}^2 - 4 \text{det} = 0$, λ_+ and λ_- are real and repeated (identical)

Within each of these three regions, the tr-det plane further classifies the dynamics and stability of isolated or non-isolated fixed points as enumerated below. The numbers within () that appear out of order are class identifiers (IDs) used in Table 3, which is a tabulated summary of the tr-det plane classification. It is notable that the only stable

region in the tr-det plane is the closed second quadrant, i.e., $\text{tr} \leq 0$ and $\text{det} \geq 0$. If a fixed point is stable, its eigenvalues λ_+ and λ_- must both be negative real: $(\lambda_+, \lambda_-) \leq 0$, or they are complex conjugates with negative real part: $\text{Re}(\lambda_+, \lambda_-) \leq 0$.

Region (a) with two real and distinct eigenvalues $\lambda_+ \neq \lambda_-$

- (1) $\lambda_+ > 0 > \lambda_-$: unstable saddle point
- (2) $\lambda_+ = 0, \lambda_- < 0$: stable line of non-isolated fixed points
- (4) $\lambda_+ > 0, \lambda_- = 0$: unstable line of non-isolated fixed points
- (5) $0 > \lambda_+ > \lambda_-$: stable sink
- (13) $\lambda_+ > \lambda_- > 0$: unstable source

Region (b) with a pair of complex conjugate eigenvalues $\lambda_{\pm} = \alpha \pm \beta i, \beta \neq 0$

- (8) $\text{Re}(\lambda_{\pm}) < 0$: stable spiral sink
- (9) $\text{Re}(\lambda_{\pm}) = 0$: stable center (not asymptotically stable)
- (10) $\text{Re}(\lambda_{\pm}) > 0$: unstable spiral source

Center is a non-hyperbolic fixed point since it has a pair of pure imaginary eigenvalues, therefore the Hartman–Grobman theorem is not applicable. A center is stable (or Lyapunov stable), but not asymptotically stable. A solution that starts close to a center stays close to it, but never converges to it over time, since non-zero pure imaginary eigenvalues correspond to periodic solutions that oscillate without damping.

Region (c) with real and repeated eigenvalues: $\lambda_{\pm} = \lambda$

- (3) $\lambda = 0$: parallel lines of non-isolated fixed points, or entire plane
- (6) $\lambda < 0$ and is incomplete: stable degenerate sink
- (7) $\lambda < 0$ and is complete: stable star sink
- (11) $\lambda > 0$ and is incomplete: unstable degenerate source
- (12) $\lambda > 0$ and is complete: unstable star source

Here a nonzero real and repeated eigenvalue is complete if it has two linearly independent eigenvectors, and the fixed point (star) is a proper node. Otherwise if the eigenvalue is incomplete (has only one eigenvector), the fixed point is a degenerate or improper node.

For a linearized 2D nonlinear system, the view is that the tr-det plane predictions for classes 1, 5, 8, 10, and 13 are always correct. Predictions for the other eight classes may not be accurate, but at least it correctly tells about the stability of classes 6, 7, 11, and 12. Prediction of class 9 is accurate if the system is conservative.

Now we apply the tr-det plane analysis for the 2D nonlinear system of the VO₂ Mott memristor PA oscillator. This system has been analyzed previously using an element combination approach, by treating a Mott memristor M and a capacitor C_p in parallel as a composite second-order nonlinear element Z_{CM} , which is connected to a resistor R_s in series. The small-signal transfer function of this 1D nonlinear system has two poles p_{\pm} that are a pair of complex conjugate in part of the circuit parameter space. Nyquist plots of figure 21(a) and 21(b) show the evolution in the positions of p_{\pm} as one steps

Table 3: Trace-determinant (tr-det) plane classification of fixed points for 2D linear homogeneous systems. In the tr-det plane, the only stable region is the closed second quadrant, i.e., $\text{tr} \leq 0$ and $\text{det} \geq 0$.

Determinant	Trace	Eigenvalues	Stability and Class	ID
$\text{det} < 0$	any	$\lambda_+ > 0 > \lambda_-$	unstable saddle point	1
$\text{det} = 0$	$\text{tr} < 0$	$\lambda_+ = 0, \lambda_- < 0$	stable line of fixed points	2
	$\text{tr} = 0$	$\lambda_+ = \lambda_- = 0$	parallel lines, or entire plane	3
	$\text{tr} > 0$	$\lambda_+ > 0, \lambda_- = 0$	unstable line of fixed points	4
$\text{det} > 0$	$\text{tr} < -\sqrt{4 \text{det}}$	$0 > \lambda_+ > \lambda_-$	stable node (sink)	5
	$\text{tr} = -\sqrt{4 \text{det}}$	repeated $\lambda_{\pm} = \text{tr}/2 < 0$	stable degenerate node (6), or stable star (7)	6,7
	$-\sqrt{4 \text{det}} < \text{tr} < 0$	complex conjugate $\text{Re}(\lambda_{\pm}) < 0$	stable spiral sink	8
	$\text{tr} = 0$	complex conjugate $\text{Re}(\lambda_{\pm}) = 0$	stable center (not asymptotically stable)	9
	$0 < \text{tr} < \sqrt{4 \text{det}}$	complex conjugate $\text{Re}(\lambda_{\pm}) > 0$	unstable spiral source	10
	$\text{tr} = \sqrt{4 \text{det}}$	repeated $\lambda_{\pm} = \text{tr}/2 > 0$	unstable degenerate node (11), or unstable star (12)	11, 12
	$\text{tr} > \sqrt{4 \text{det}}$	$\lambda_+ > \lambda_- > 0$	unstable node (source)	13

R_s while keeping $C_p = 1$ pF and $V_{\text{dc}} = 1.2$ V unchanged. Increasing R_s from 3.3 k Ω to 3.4 k Ω flips the sign of $\text{Re}(p_{\pm})$ from negative to positive and produces a crossover from LP to LA as per Chua's LA theorem for a 1D uncoupled element.

Instead of element combination, now we apply the tr-det plane analysis of the Jacobian linearized 2D PA oscillator system. We show that the 2D tr-det plane method elucidates the nature of this crossover in local activity to be a bifurcation which changes the stability of an isolated fixed point. Figure 23(a) plots the (tr, det) plane that is geometrically divided into different regions by the tr- and det-axes and the $\text{det} = \text{tr}^2/4$ parabola. Each of them are labeled by the class IDs as listed in Table 3. It shows a locus of (tr, det) calculated from the Jacobian matrix of the midsize VO₂ Mott memristor PA oscillator around its fixed points, by fixing $C_p = 1$ pF, $V_{\text{dc}} = 1.2$ V, and stepping R_s from 100 Ω to 17.2 k Ω at 100 Ω interval. The (tr, det) points for 100 $\Omega \leq R_s \leq 600$ Ω outside the plotted area are all located above the $\text{det} = \text{tr}^2/4$ parabola within the same stable spiral sink (class 8) region. The trajectory of (tr, det) formed by varying R_s is

nonlinear and convex shaped. Increasing R_s moves (tr, det) toward the region of an unstable spiral source (class 10) in the first quadrant and produces a bifurcation as it crosses the positive det axis. At $R_s > 7.5$ k Ω , (tr, det) of the fixed point crosses the $det = tr^2/4$ parabola into the unstable source (class 13) region, but its stability remains unchanged. Therefore, R_s is clearly a bifurcation parameter for the 2D PA oscillator.

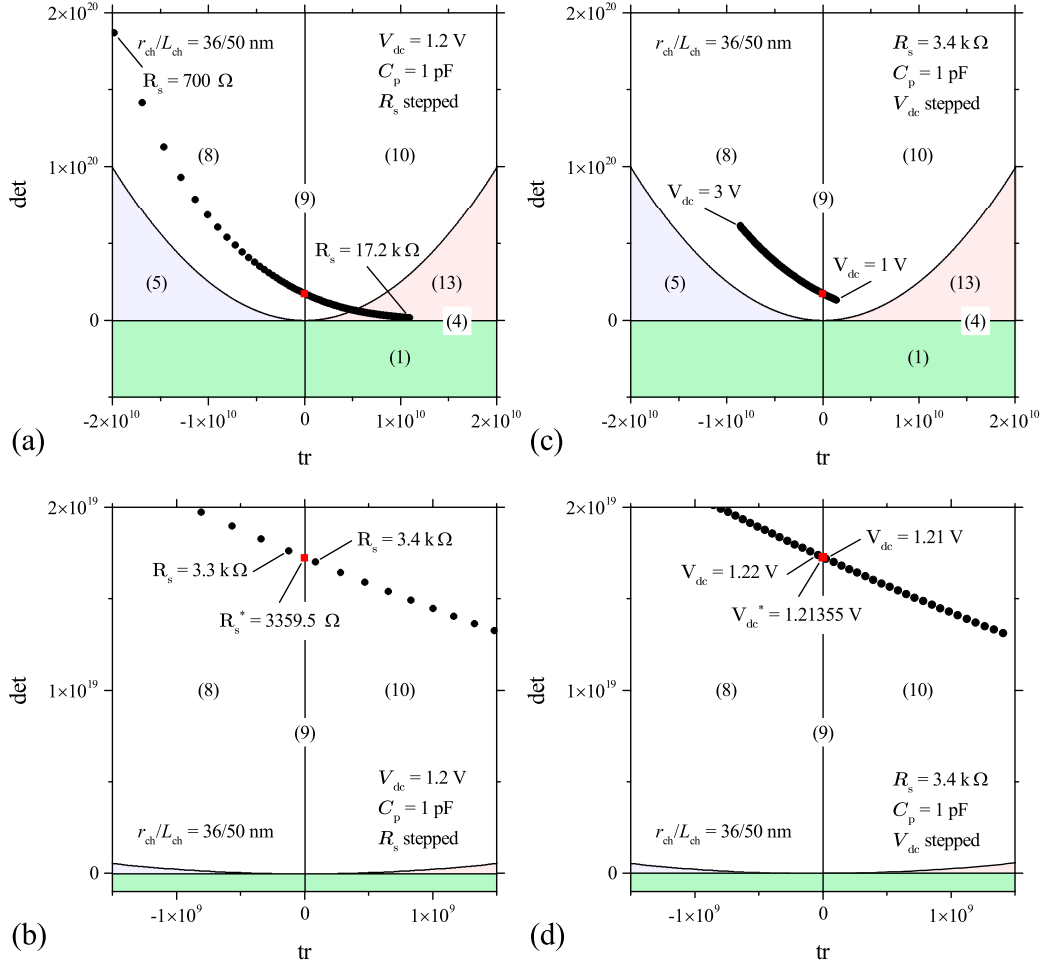


Figure 23: (a) Trace-determinant plane showing the (tr, det) locus for the Jacobian of the midsize VO₂ Mott memristor PA oscillator with $C_p = 1$ pF, $V_{dc} = 1.2$ V, and bifurcation parameter R_s stepped from 100 Ω to 17.2 k Ω at 100 Ω interval. (b) is a zoomed view of (a), showing that increasing R_s from 3.3 k Ω to 3.4 k Ω results in a bifurcation from a stable spiral sink (class 8) to an unstable spiral source (class 10). At $R_s^* = 3359.5$ Ω , the fixed point is a stable center (class 9) located on the $tr = 0$ axis. (c) The (tr, det) locus for the Jacobian of the same PA oscillator with $R_s = 3.4$ k Ω , $C_p = 1$ pF, and bifurcation parameter V_{dc} stepped from 1 V to 3 V at 10 mV interval. (d) is a zoomed view of (c), showing that increasing V_{dc} from 1.21 V to 1.22 V produces a bifurcation from an unstable spiral source (class 10) to a stable spiral sink (class 8). At $V_{dc}^* = 1.21355$ V, the fixed point is a stable center (class 9) located on the positive det axis.

Figure 23(b) is a zoomed view of (a). It shows that increasing R_s from 3.3 k Ω to 3.4 k Ω produces a stability-change bifurcation from a stable spiral sink (class 8) to an

unstable spiral source (class 10), both belonging to Region (b) of $\text{tr}^2 - 4\det < 0$ that has complex conjugate Jacobian eigenvalues. At a critical value of $R_s^* = 3359.5 \Omega$, (tr, \det) is located exactly on the $\text{tr} = 0$ axis as the borderline between the unstable first quadrant and stable second quadrant. The tr - \det plane predicts that the fixed point is a stable center (class 9). We have learned that predictions about a spiral sink (class 8) and a spiral source (class 10) are always correct for 2D nonlinear systems, but the prediction about a center (class 9) is unproven, since a 2D PA oscillator is not a conservative system.

In figure 23(c), we plot the (tr, \det) locus for the Jacobian of the same PA oscillator around its fixed points, this time by fixing $R_s = 3.4 \text{ k}\Omega$, $C_p = 1 \text{ pF}$, and stepping V_{dc} from 1 V to 3 V at 10 mV interval. It shows a similarly shaped convex trajectory of (tr, \det) as the case for stepping R_s . However, the effect of V_{dc} is opposite to that of R_s — a larger V_{dc} moves (tr, \det) toward the stable spiral sink (class 8) region in the second quadrant. Figure 23(d) is a zoomed view of (c), showing that increasing V_{dc} from 1.21 V to 1.22 V produces a stability-change bifurcation from an unstable spiral source (class 10) to a stable spiral sink (class 8). At a critical value of $V_{\text{dc}}^* = 1.21355 \text{ V}$, (tr, \det) is located exactly on the $\text{tr} = 0$ axis. Therefore, V_{dc} is also a bifurcation parameter for the 2D PA oscillator. The fact that the critical values of bifurcation parameters R_s and V_{dc} found by the tr - \det plane analysis match well with those found by the small-signal Nyquist plot analysis of the element combination approach (see figure 21) corroborates the validity of both methods.

The parallel capacitor C_p also works as a bifurcation parameter if one fix R_s and V_{dc} and adjust C_p . Figure 24(a) plots four loci of the Jacobian (tr, \det) for the midsize VO₂ Mott memristor PA oscillator, now with $V_{\text{dc}} = 1.2 \text{ V}$ and R_s fixed at 3 k Ω , 5 k Ω , 7 k Ω and 9 k Ω , respectively. For each locus, we step up C_p in the sequence of: 10 fF, 20 fF, 50 fF, 0.1 pF, 0.2 pF, 0.5 pF, 1 pF, 2 pF, 5 pF and 10 pF. Similar to the case of varying R_s , increasing C_p also moves (tr, \det) from the stable second quadrant into the unstable first quadrant. However, the (tr, \det) locus is linear instead of convex shaped. Equations (66) and (67) together predict a slope of $-\omega_1 [1 + R_1 / (R_{\text{ch}} + R_s)]$ for the (tr, \det) locus if C_p is varied, which matches exactly with the linear regression slopes of the four loci. Equation 67 also predicts that (tr, \det) asymptotically approaches the positive tr axis as one continuously increases C_p , but never reaches it. Open symbols highlight the critical C_p^* values for the stability-change bifurcation as the (tr, \det) loci intercept the positive \det axis. It can be seen that a larger fixed R_s would shift the (tr, \det) locus upward and decrease its critical C_p^* value. Figure 24(b) plots the dependence of critical C_p^* on R_s in a log-log fashion for three different V_{dc} settings at 1.0 V, 1.2 V and 1.4 V. One can tell that $C_p^*(R_s)$ follows a power law with an exponent close to -2.5 . For the trace at $V_{\text{dc}} = 1.2 \text{ V}$, we added the point of $R_s = 3359.5 \Omega$. The power law predicts a $C_p^* = 1 \text{ pF}$, which is consistent with the critical (R_s^*, C_p) value for the same bifurcation in the case of varying R_s at a fixed $C_p = 1 \text{ pF}$ (see figure 23(b)).

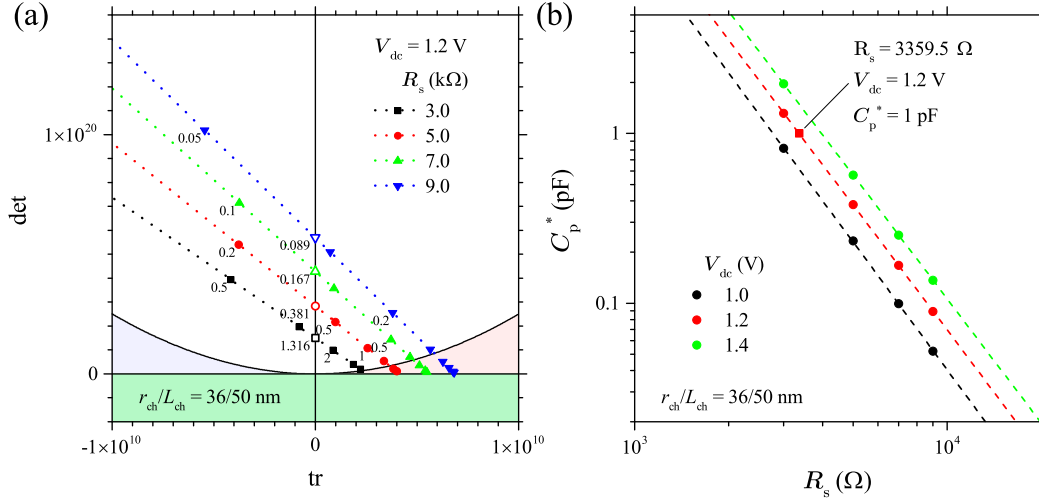


Figure 24: (a) Trace-determinant plane showing four (tr, det) loci for the Jacobian of the midsize VO₂ Mott memristor PA oscillator with $R_s = 3$ kΩ, 5 kΩ, 7 kΩ and 9 kΩ, respectively, all at $V_{dc} = 1.2$ V. For each locus, increasing C_p (from 10 fF to 10 pF in the present case) moves the Jacobian (tr, det) along a linear trajectory from the stable second quadrant into the unstable first quadrant, which then approaches the positive tr axis asymptotically. The open symbol that intercepts the positive det axis shows the critical C_p^* for the source-sink bifurcation. (b) Log-log plot of the critical C_p^* vs. R_s for three cases of $V_{dc} = 1.0$ V, 1.2 V and 1.4 V. Dashed lines are power-law fits $C_p^* = aR_s^b$ with an exponent $b \approx -2.5$. Square (red) shows that $C_p^* = 1$ pF if $R_s = 3359.5$ Ω, which is consistent with figure 23(b).

6. Global analysis of reactively-coupled Mott memristors: 2D relaxation oscillator

6.1. Nullclines and direction field

The local analysis techniques we have discussed so far require a foreknowledge of the fixed points for a 2D nonlinear system. Global analyses, such as nullclines in the phase space of state variables, can be used to analyze a nonlinear system of ODEs and locate its fixed points. For a 2D or planar system, the x - (or y -) nullcline is defined as the set of points in the phase plane of (x, y) where the time derivative of x (or y) vanishes. Therefore the vector field is vertical on the x -nullcline and horizontal on the y -nullcline. Together, they partition \mathbb{R}^2 into different open regions differing on the sign of their time derivatives. One can then determine the direction of vector field in each region. The intersections of the x - and y -nullclines yield the fixed points. A direction field (also called a slope field) is the scaled version of a vector field, with all the vector lengths normalized to unity. In the 2D phase plane, plotting the x - and y -nullclines together with the direction field reveals fixed points and offer clues about their dynamical classification as well as orbits of solutions.

For the case of a 2D Mott memristor PA oscillator, the x -nullcline (x_0, v_0) is the locus of points where the time derivative of the state variable x for the memristor M

vanishes

$$f(x_0, v_0) = f_x \left(x_0, \frac{v_0}{R_{\text{ch}}(x_0)} \right) = 0 \quad (70)$$

which can be rewritten as

$$v_0 = \left[-A (1 + Bx_0^2) \frac{\ln x_0}{C} \right]^{-0.5} \quad (71)$$

Since (x_0, v_0) are steady states of M , the x -nullcline only depends on the internal characteristics of M , and is independent of the external circuit parameters including R_s , C_p and V_{dc} . It remains the same as that of an isolated M (see figure 7(c)).

The v -nullcline (x_1, v_1) is the locus of points where the time derivative of the state variable v vanishes

$$g(x_1, v_1) = \frac{1}{C_p} \left(\frac{V_{\text{dc}} - v_1}{R_s} - \frac{v_1}{R_{\text{ch}}(x_1)} \right) = 0 \quad (72)$$

which can be rewritten as

$$v_1 = \frac{V_{\text{dc}}}{1 + R_s A (1 + Bx_1^2)} \quad (73)$$

Since v is the voltage across the capacitor C_p and M in parallel, this means that the charge stored on the capacitor does not change over time, thus there is no current flowing through it. Therefore, R_s in series with M forms a voltage divider. The v -nullcline depends on V_{dc} and R_s , but is independent of C_p .

The intersections of the x - and v -nullclines are the fixed points Q of the 2D system where both x - and v -derivatives vanish

$$f(x_Q, v_Q) = f_x \left(x_Q, \frac{v_Q}{R_{\text{ch}}(x_Q)} \right) = 0 \quad (74)$$

$$g(x_Q, v_Q) = \frac{1}{C_p} \left(\frac{V_{\text{dc}} - v_Q}{R_s} - \frac{v_Q}{R_{\text{ch}}(x_Q)} \right) = 0 \quad (75)$$

Figure 25 plots the x - and v -nullclines and direction field in the phase plane of the midsize VO₂ Mott memristor PA oscillator with $R_s = 3.4 \text{ k}\Omega$ and $V_{\text{dc}} = 1.2 \text{ V}$. Note that the direction field depends on C_p and is plotted for the case of $C_p = 1.0 \text{ pF}$. At these settings, the 2D nonlinear system has just one fixed point $(x_Q, v_Q) = (0.30396, 0.12564)$ at the single intersection of the x -nullcline (blue violet line) and v -nullcline (brown line). The x - and v -nullclines partition the phase plane into four open regions depending on the signs of time derivatives for x and v , labeled as $(++)$, $(+-)$, $(-+)$ and $(--)$, respectively. The direction field (arrowheads) shows a conspicuous clockwise rotational pattern around Q , suggesting that the orbit of a solution $(x(t), v(t))$ with an initial condition close to Q would rotate around it clockwise. Intuitively, if Q were a stable spiral sink, $(x(t), v(t))$ would approach it along a spiral. If Q were an unstable spiral source, $(x(t), v(t))$ would move away from it along a spiral. However, we will show that it is also possible that $(x(t), v(t))$ forms an isolated periodic orbit that keeps rotating around Q . Additional analyses are required besides the nullclines and direction field to know if such a case exists.

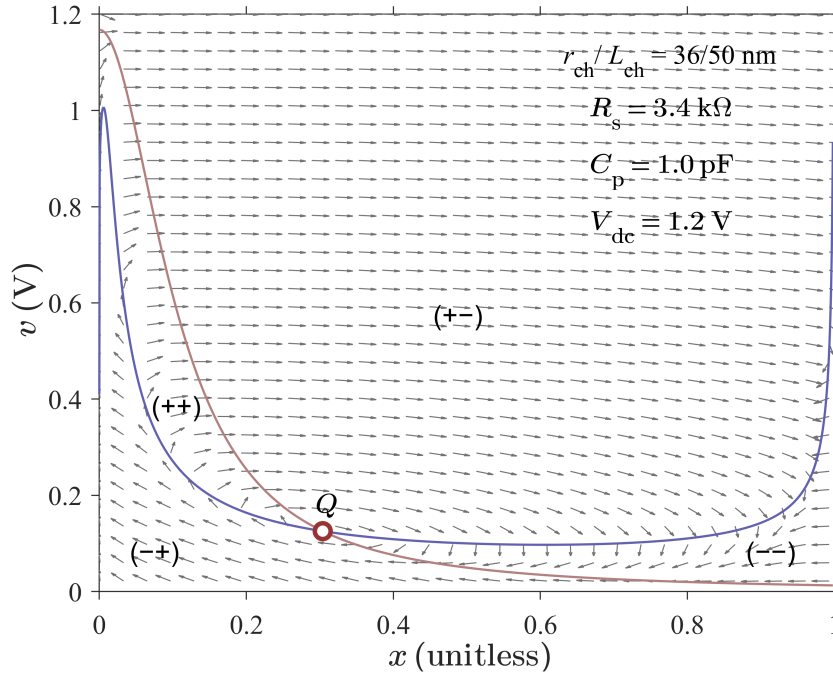


Figure 25: Nullclines and direction field (arrowheads) in the phase plane of the midsize VO₂ Mott memristor PA oscillator with $R_s = 3.4 \text{ k}\Omega$, $C_p = 1.0 \text{ pF}$ and $V_{dc} = 1.2 \text{ V}$. Under these conditions, the 2D nonlinear system has one fixed point $(x_Q, v_Q) = (0.30396, 0.12564)$ at the single intersection of the x - (blue violet line) and v - (brown line) nullclines. Based on the signs of dx/dt and dv/dt , the x - and v -nullclines partition the \mathbb{R}^2 plane into four open regions labeled as $(++)$, $(+-)$, $(-+)$ and $(--)$, respectively.

Since the location of the v -nullcline varies with V_{dc} and R_s , decreasing V_{dc} will shift it downward with respect to the x -nullcline, which may change the number of intersections between them. To find out about it, in figure 26 we plot three sets of x -, v -nullclines and direction field for the same model PA oscillator at V_{dc} values of 1.0379 V, 1.0 V and 0.519 V, respectively. Figure 26(a) and its zoomed view (b) show the case of $V_{dc} = 1.0379 \text{ V}$. At this critical value of V_{dc} , the v -nullcline becomes tangent with the x -nullcline near its peak at the PDR-to-NDR crossover $Q_a^* = (0.00589, 1.00681)$, increasing the number of fixed points from one to two.

Further reducing V_{dc} will split Q_a^* into a pair of unstable (Q_2) and stable (Q_3) fixed points that move apart from each other as V_{dc} further drops. This is characteristic of a 2D saddle-node bifurcation. We are already familiar with the 1D case for an isolated Mott memristor (see figure 6). To illustrate, Figure 26(c) and its zoomed view (d) show the case of $V_{dc} = 1.0 \text{ V}$. Now there are three intersections between the v - and x -nullclines. Besides the original fixed point $Q_1 = (0.25937, 0.13823)$ located in the NDR region of M , two new fixed points $Q_2 = (0.01064, 0.96326)$ and $Q_3 = (0.00243, 0.97254)$ emerge at very small x values. As a result, the \mathbb{R}^2 plane is now partitioned into six open regions instead of four. The two additional regions are $(++)$ within the PDR region of M , and $(--)$ near the PDR-to-NDR transition of M . The direction field gives away that Q_2 is an unstable node, while Q_3 is a stable node at an intersection in the PDR

region (insulating state) of M .

Q_1 and Q_2 approach each other as V_{dc} further drops. Figure 26(e) and its zoomed view (f) show that at another critical value of $V_{dc} = 0.519$ V, the v -nullcline becomes tangent with the x -nullcline in its NDR region as Q_1 and Q_2 merge into one fixed point Q_b^* . It then disappears if V_{dc} continues to drop. At $V_{dc} < 0.519$ V, only one stable fixed point Q_3 survives in the insulating state of M .

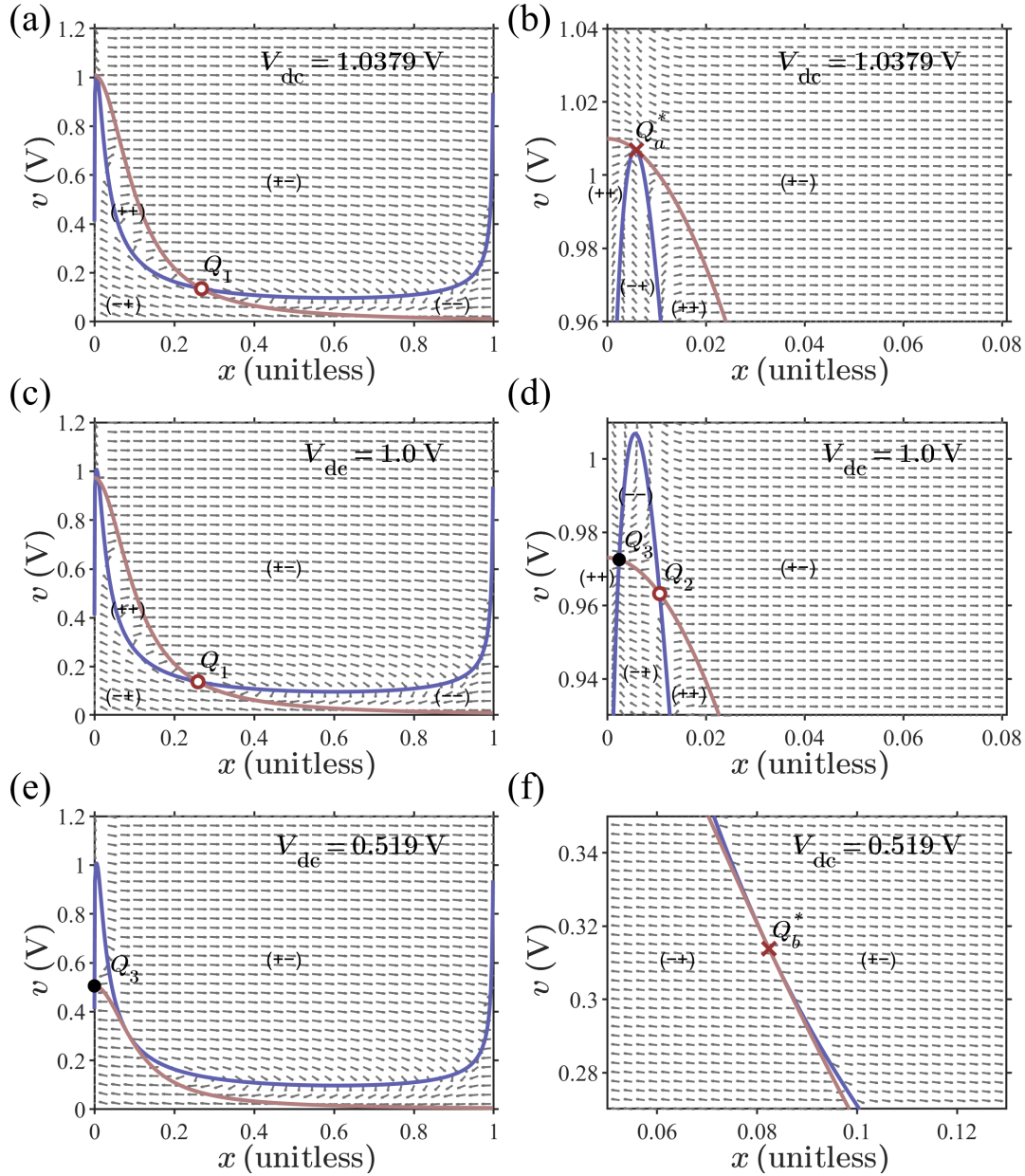


Figure 26: Nullclines and direction fields (arrowheads) in the phase plane of the midsize VO_2 Mott memristor PA oscillator with $R_s = 3.4$ k Ω , $C_p = 1.0$ pF and V_{dc} at (a) 1.0379 V, (c) 1.0 V, and (e) 0.519 V. (b), (d) and (f) are zoomed views to reveal semi-stable (\times), stable (\bullet), and unstable (\circ) fixed points at the intersections of the x - (blue violet line) and v - (brown line) nullclines.

6.2. 2D saddle-node bifurcations by varying V_{dc}

Plotting nullclines and direction fields at different values of V_{dc} allowed us to identify two bifurcations, both appear to be 2D saddle-node bifurcation. Next, we apply the bifurcation diagram and tr-det plane methods to clarify their nature. We step the bifurcation parameter V_{dc} from 3.0 V to 0 V at an interval of 0.01 V while keep the other parameters unchanged, and solve the fixed points (x_Q, v_Q) by finding all the intersection of x - and v -nullclines. Figure 27(a) and (b) are the bifurcation diagrams for x_Q and v_Q , respectively. Solid (open) circles are used for stable (unstable) fixed points. There exist three distinctive regions (I, II, III) according to the number of fixed points at a specific V_{dc} . In region I ($V_{dc} > 1.0379$ V), there is only one fixed point Q_1 . The tr-det plane analysis (Figure 23(d)) told us that Q_1 has a stability-change bifurcation at $V_{dc} = 1.21355$ V (labeled as Q_c^*) and switches from a stable spiral sink to an unstable spiral source as V_{dc} drops below 1.21355 V.

At $V_{dc} = 1.0379$ V, a new fixed point Q_a^* emerges at (0.00589, 1.00681). It then splits into two fixed points Q_2 (unstable) and Q_3 (stable) which move away from each other as V_{dc} further drops. These characteristics resemble a 2D saddle-node bifurcation. In region II (0.519 V $< V_{ch} < 1.0379$ V), the 2D system has three fixed points (stable Q_3 , unstable Q_1 and Q_2). As V_{dc} continues to decrease, another bifurcation occurs at $V_{dc} = 0.519$ V, where Q_1 and Q_2 coalesce into Q_b^* at (0.08240, 0.31379) and annihilate each other. This corresponds to the v -nullcline becoming tangent with the x -nullcline in its NDR region before departing from it. The system only has one stable fixed point Q_3 in region III (0 V $< V_{ch} < 0.519$ V), as the v -nullcline only intersects with the x -nullcline in the insulating region of the Mott memristor.

To further understand the bifurcations at Q_a^* and Q_b^* , in figure 27(c), we plot the (tr, det) loci for the Jacobian of all the fixed points shown in (a) and (b). Since two of the Jacobian elements are functions of C_p , the calculations are done at $C_p = 1.0$ pF to match with figure 26. The (tr, det) locus of Q_1 was already shown in figure 23(c) and (d) and is re-plotted here with a much wider range of V_{dc} . At $V_{dc} > 1.21355$ V, it is in the second quadrant above the $\det = \text{tr}^2/4$ parabola as a stable spiral. At $V_{dc} = 1.21355$ V, it crosses the positive det axis at Q_c^* as a center into the first quadrant and switches the stability. For 0.519 V $< V_{dc} < 1.21355$ V, Q_1 remains unstable, first as an unstable spiral, then as an unstable node after crossing the $\det = \text{tr}^2/4$ parabola, before vanishing at $V_{dc} = 0.519$ V.

At $V_{dc} = 1.0379$ V, a saddle-node bifurcation creates a new fixed point Q_a^* . Figure 27(d) as a zoomed view of 27(c) shows that Q_a^* is located on the negative tr axis very close to the origin (at $\text{tr} = -2.23772 \times 10^8$). It then splits into a pair of fixed points Q_2 and Q_3 . The (tr, det) locus of Q_2 follows a V-shaped trajectory and resides entirely within the fourth quadrant, indicating that Q_2 is an unstable saddle point (class 1). The (tr, det) locus of Q_3 is entirely within the second quadrant below the $\det = \text{tr}^2/4$ parabola, indicating that Q_3 is a stable sink (class 5). As V_{dc} drops from 1.0379 V, Q_1 and Q_2 approach each other until they coalesce into Q_b^* as V_{dc} reaches 0.519 V,

indicating that another saddle-node bifurcation occurs. Q_b^* is located on the positive tr axis. It vanishes at even lower V_{dc} values, and the only fixed point left is Q_3 in the second quadrant. Interestingly, the saddle-node bifurcation at Q_b^* involves two unstable fixed points Q_1 and Q_2 , rather than a pair of stable and unstable fixed points as in typical cases.

It is worth mentioning that the linearized tr-det plane predictions on the borderline classes (class 2 and 4 on the tr axis) are incorrect, since Q_a^* and Q_b^* are non-hyperbolic semi-stable fixed points rather than a stable or unstable line of fixed points. It also cannot tell about a possible Hopf bifurcation associated with the non-hyperbolic fixed point Q_c^* (class 9 on the det axis). Therefore we will revisit this topic in subsection 6.7.

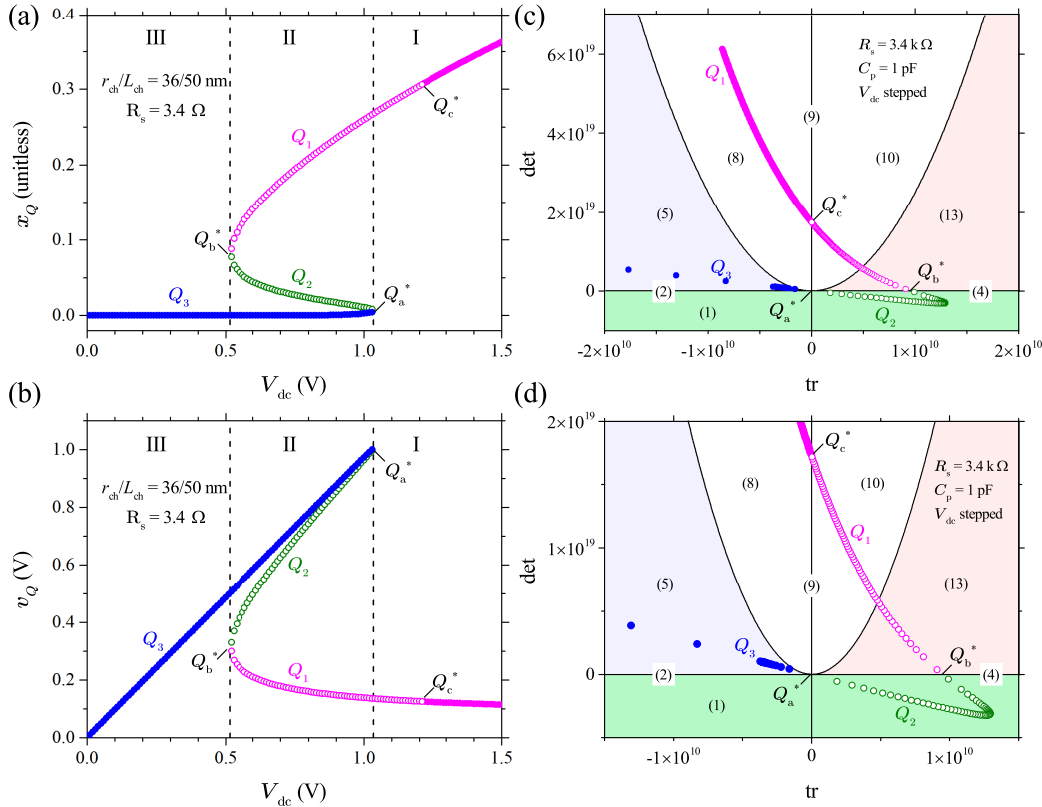


Figure 27: Bifurcation diagrams showing V_{dc} dependences of (a) x_Q and (b) v_Q of the fixed point (x_Q, v_Q) for the midsize VO₂ Mott memristor PA oscillator, found by the nullclines method. $R_s = 3.4 \text{ k}\Omega$ and C_p is arbitrary. Stable (unstable) fixed points are represented by solid (open) circles. As V_{dc} is stepped from 3 V to 0 V at 0.01 V interval (plotted up to 1.5 V for clarity), initially (region I) the 2D system has only one fixed point Q_1 , which undergoes a stability-change bifurcation at $V_{dc} = 1.21355 \text{ V}$ (Q_c^*). A saddle-node bifurcation at $V_{dc} = 1.0379 \text{ V}$ (Q_a^*) creates a pair of fixed points Q_2 and Q_3 in region II. At $V_{dc} = 0.519 \text{ V}$ (Q_b^*), another bifurcation occurs as Q_1 and Q_2 coalesce and annihilate each other. For even lower V_{dc} (region III), only one fixed point Q_3 exists. (c) The (tr, det) loci for the Jacobian of the same fixed points as shown in (a) and (b), calculated with $C_p = 1.0 \text{ pF}$. (d) is a zoomed view of (c), showing that Q_a^* is located on the negative tr axis very close to the origin, Q_b^* is on the positive tr axis, and Q_c^* is on the positive det axis.

6.3. 2D supercritical Hopf-like bifurcation by varying R_s

The tr-det plane analysis of a linearized VO₂ Mott memristor PA oscillator showed that its fixed point can be a non-hyperbolic center as the R_s or C_p parameter passes through a critical value. Stability and qualitative behavior of nonlinear systems near a non-hyperbolic fixed point is tricky and requires further theoretical treatment. Here using R_s as the bifurcation parameter, we illustrate an example of 2D local Hopf-like bifurcation. For nonlinear systems of dimension two or higher, a local Hopf bifurcation, also called Poincaré-Andronov-Hopf bifurcation, is the local creation or annihilation of a periodic solution around a fixed point as it switches stability. The bifurcating periodic solution is called a limit cycle, which is an isolated periodic orbit (closed trajectory) with no nearby periodic orbits, such that at least a nearby trajectory spirals into it either as time approaches infinity or as time approaches negative infinity. The orbital stability of a limit cycle is opposite to that of the fixed point it encircles. If a stable limit cycle appears around an unstable fixed point, it is a supercritical Hopf bifurcation. Otherwise if an unstable limit cycle appears around a stable fixed point, then it is a subcritical Hopf bifurcation. The example we will discuss has a supercritical orbital stability.

6.4. Hopf bifurcation theorem

For a nonlinear system near a non-hyperbolic fixed point in its linear part, the center manifold theorem states that its qualitative behavior can be told by the behavior on the center manifold. The Jacobian matrix of the linearized system defines three main subspaces according to the real part of its eigenvalues. The center subspace is spanned by eigenvectors corresponding to eigenvalues with zero real part. A center manifold is an invariant manifold of the same dimension as and tangent to the center subspace. The stability problem is therefore reduced to lower dimensions. A direct application of the center manifold theorem is the Hopf bifurcation theorem, which allows *analytical* prediction on the existence of limit cycles. A version of the Hopf bifurcation theorem that is generalized to \mathbb{R}^n is briefly introduced here [57, 58]. Consider a nonlinear system $\dot{\mathbf{x}} = \mathbf{f}(\mathbf{x}; \mu)$, $\mathbf{x} \in \mathbb{R}^n$, $\mu \in \mathbb{R}$, where μ is a bifurcation parameter. Assume it has a fixed point $(\mathbf{x}_0; \mu)$ so that $\mathbf{f}(\mathbf{x}_0; \mu) = 0$. The eigenvalues of the linearized system $\dot{\mathbf{x}} = D\mathbf{f}(\mathbf{x}; \mu)$ about this fixed point are $\lambda_{\pm}(\mu) = \alpha(\mu) \pm \beta(\mu)i$. If both of the following conditions are satisfied at $\mu = \mu_0$:

- a) $\alpha(\mu_0) = 0$, $\beta(\mu_0) \neq 0$ (non-hyperbolicity condition), i.e., there is a pair of simple, conjugate pure imaginary eigenvalues and no other pure imaginary eigenvalues,
- b) $\left. \frac{d\alpha(\mu)}{d\mu} \right|_{\mu=\mu_0} = d \neq 0$ (transversality condition), i.e., the eigenvalues cross the imaginary axis with finite speed,

then there is a unique center manifold passing through $(\mathbf{x}_0; \mu_0)$ in $\mathbb{R}^n \times \mathbb{R}$.

The third condition (genericity condition) is about the first Poincaré-Lyapunov constant $L_1(\mu_0)$, which is the coefficient of cubic terms if the system is transferred to the normal form. If $L_1(\mu_0) \neq 0$, then a surface of periodic solutions exists in the center

manifold. Approximated to the second order, this surface is a paraboloid tangent to the eigenspace associated with $\lambda_{\pm}(\mu_0)$. The region for periodic solutions to appear (either as μ moves into $\mu < \mu_0$ or into $\mu > \mu_0$) as well as the stability of periodic solutions are determined by the signs of $L_1(\mu_0)$ and d [57]. For the case of $d > 0$ that is relevant to our example, if $L_1(\mu_0) < 0$, then Hopf bifurcation is supercritical, i.e., a stable limit cycle bifurcates from an unstable fixed point into the region $\mu > \mu_0$. If $L_1(\mu_0) > 0$, then Hopf bifurcation is subcritical, i.e., an unstable limit cycle bifurcates from a stable fixed point into the region $\mu < \mu_0$.

Calculation of $L_1(\mu_0)$ can be a substantial effort, as it involves the second and third order derivatives of the system about the bifurcation point. For the sake of brevity, we leave aside the derivation of the first Poincaré-Lyapunov constant $L_1(\mu_0)$ for a Mott memristor PA oscillator, and only examine if it satisfies the non-hyperbolicity and transversality conditions. Figure 28(a) shows the complex-plane loci of the pair of simple, conjugate eigenvalues $\lambda_{\pm}(R_s)$, calculated by equation (68) for the Jacobian of the midsize VO₂ Mott memristor PA oscillator that has been analyzed by the tr-det plane method (see figure (23)). Fixing C_p , V_{dc} and increasing the bifurcation parameter R_s , the fixed point of the linearized system evolves from a stable spiral ($\text{Re}(\lambda_{\pm}) < 0$), to a non-hyperbolic center ($\text{Re}(\lambda_{\pm}) = 0$) at $R_s^* = 3359.5 \Omega$, and then to an unstable spiral ($\text{Re}(\lambda_{\pm}) > 0$). At $R_s = R_s^*$, the system satisfies the non-hyperbolicity condition for a Hopf bifurcation. Figure 28(b) plots $d\text{Re}(\lambda_{\pm})/dR_s$ vs. R_s calculated from $\lambda_{\pm}(R_s)$, which shows that the derivative of the real part of eigenvalues with respect to the bifurcation parameter R_s is finite and positive at the non-hyperbolic center ($R_s = R_s^*$) and its nearby region. Thus the transversality condition for a Hopf bifurcation is also satisfied.

6.5. Phase portrait analysis of limit cycles

Now we check the above analytical prediction against numerical calculations. A local Hopf bifurcation can be revealed by numerically solving the coupled ODEs with an arbitrary initial condition (x_0, v_0) , then inspecting the orbit of the solution $(x(t), v(t))$ in the phase plane pre-loaded with nullclines and direction field. Such a plot is called a phase portrait. Plotting the time series $x(t)$ and $v(t)$ of the numerical solution helps tell if there are damped oscillations toward a stable fixed point, or persistent self-excited oscillations characteristic of a limit cycle.

Figure 29 compares two sets of phase portraits and the corresponding time series for the midsize VO₂ Mott memristor PA oscillator with $C_p = 1.0$ pF, $V_{dc} = 1.2$ V and initial condition $(x_0, v_0) = (0.1, 0.39)$, numerically solved by a MATLAB ode45 solver [59]. Figure 29 (a)–(c) (left column) show the case for $R_s = 3.2$ k Ω . At this value of R_s , there is a single fixed point $(x_Q, v_Q) = (0.3178, 0.1225)$ at the intersection of the nullclines. The linear tr-det plane analysis predicts that it is a stable spiral sink (see figure 23(b) and text). The phase portrait corroborates this prediction, showing that the orbit of the solution (purple trace) converges to Q along a clockwise spiral trajectory. The clockwise rotation of the system state over time is determined by the

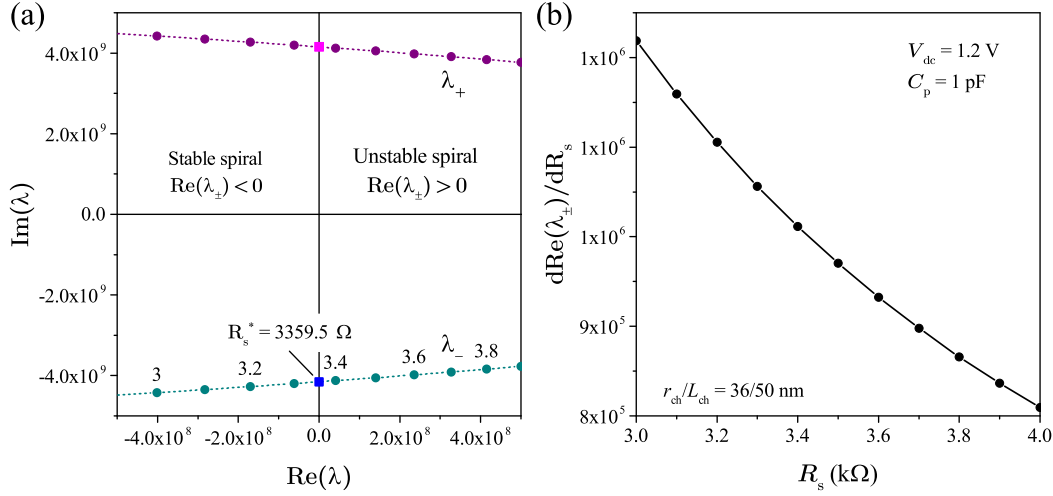


Figure 28: Examination of the non-hyperbolicity and transversality conditions for the Hopf bifurcation theorem. (a) Loci of the conjugate pair of eigenvalues $\lambda_{\pm}(R_s)$ in the complex plane for the Jacobian of the midsize VO_2 Mott memristor PA oscillator with $C_p = 1$ pF, $V_{dc} = 1.2$ V, and bifurcation parameter R_s stepped at 100Ω interval (labeled as $k\Omega$ for several λ_- points). The Jacobian has a stable spiral for $\text{Re}(\lambda_{\pm}) < 0$ and an unstable spiral for $\text{Re}(\lambda_{\pm}) > 0$. At $R_s^* = 3359.5 \Omega$, λ_{\pm} are pure imaginary and the fixed point is a non-hyperbolic center located on the $\text{tr} = 0$ axis. (b) Calculated $d\text{Re}(\lambda_{\pm})/dR_s$ vs. R_s , showing that its value is finite and positive for R_s that ranges from 3.0 k Ω to 4.0 k Ω .

direction field. The time series $x(t)$ and $v(t)$ shown in the bottom rows exhibit fast damped oscillations that come to rest at (x_Q, v_Q) within about 20 ns.

Figure 29 (d)–(f) (right column) show the case for $R_s = 3.4$ k Ω . Such a small increase in R_s (by 200Ω) results in a tiny shift in the location of Q to $(x_Q, v_Q) = (0.3040, 0.1256)$. The linear tr - \det analysis predicts that Q switches its stability and becomes an unstable spiral source. The orbit initially resembles the case of figure 29 (a), but it does not finish even one loop around Q before morphing into a periodic orbit that rotates clockwise about Q with a distorted rectangular shape. The corresponding time series $x(t)$ and $v(t)$ shown in the bottom rows exhibit periodic oscillations — a pulse train $\tilde{x}(t + T_{lc}) = \tilde{x}(t)$ and a sawtooth wave $\tilde{v}(t + T_{lc}) = \tilde{v}(t)$, both launched after a very short transient period. Here T_{lc} is the period of the limit cycle. Appearance of a stable limit cycle around a fixed point as it switches from a stable sink to unstable source is the hallmark of a supercritical Hopf bifurcation. We added several colored diamonds to represent solutions $x(t)$ and $v(t)$ equally spaced in time from 25.5 ns to 28 ns at 0.5 ns interval. Their locations on the closed trajectory of limit cycle are clearly unevenly spaced, revealing the alternative slow-fast motion along it as a hallmark for relaxation oscillations.

To convince ourselves that the periodic orbit revealed by figure 29 (d)–(f) is both isolated and stable, i.e., a stable limit cycle, we numerically calculated 324 solutions of the same system with the initial condition (x_0, v_0) distributed on a regularly spaced

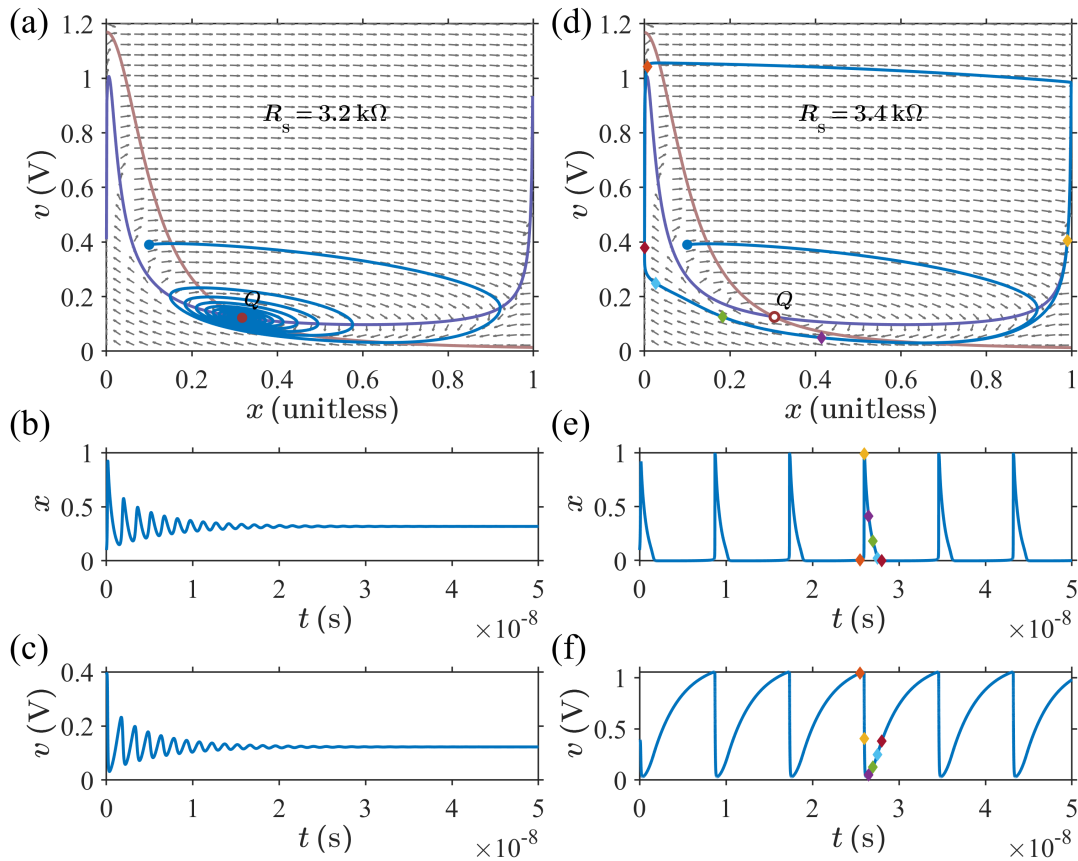


Figure 29: Phase portraits $(x(t), v(t))$ (top row) and the corresponding time series $x(t), v(t)$ (middle and bottom rows) numerically solved by a MATLAB ode45 solver for the midsize VO₂ Mott memristor PA oscillator with $C_p = 1.0$ pF, $V_{dc} = 1.2$ V and the initial condition $(x_0, v_0) = (0.1, 0.39)$. Left column ((a)–(c)) is the case for $R_s = 3.2$ k Ω with a stable fixed point $(x_Q, v_Q) = (0.3178, 0.1225)$ at the intersection of the nullclines. The phase portrait and time series corroborate the linear analysis prediction that it is a spiral sink. Right column ((d)–(f)) is the case for $R_s = 3.4$ k Ω with an unstable fixed point $(x_Q, v_Q) = (0.3040, 0.1256)$ (open circle). The phase portrait and time series reveal the birth of a limit cycle encircling Q as it switches stability, characteristic of a Hopf bifurcation. Colored diamonds are solutions equally spaced in time from 25.5 ns to 28 ns at 0.5 ns interval, showing alternative slow-fast motion along the closed limit cycle trajectory.

(18 \times 18) grid that spans across almost the entire allowable (x, v) phase space. x_0 is evenly spaced from 0.05 to 0.95, and v_0 from 0.06 V to 1.14 V. Orbits that start from within and outside the limit cycle are light and dark gray colored, respectively. The results are shown in figure 30. The phase portrait in figure 30(a) offers a sampled view for the flow of this 2D nonlinear system. It shows that, regardless of its initial condition location, the $(x(t), v(t))$ orbit always settles on the same limit cycle $(\tilde{x}(t), \tilde{v}(t))$ (the blue orbit) after a transient movement. If (x_0, v_0) is very close to Q , the transient part of the orbit can form many turns of clockwise spiral following the direction field, but the orbit always manage to “escape” from Q and becomes a limit cycle encircling it. The time series in figure 30(b) reveal that the time elapsed in the transient stage

until $x(t)$ (or $v(t)$) become periodic varies across individual solutions, depending on the initial condition (x_0, v_0) . The distinctive transient time makes the oscillation waveforms asynchronous across individual orbits, which is equivalent of having different oscillation phases. However, all the time series settle as oscillations sharing the same period. To be precise, the mean (standard deviation) of the oscillation period is 8.621 ns (5 ps), with a coefficient of variation as small as 0.06 %. The minimum and maximum oscillation period are 8.6 ns and 8.626 ns, respectively. The robustness of a limit cycle against the initial transient may explain why life is full of relaxation oscillators, including the heartbeat [60].

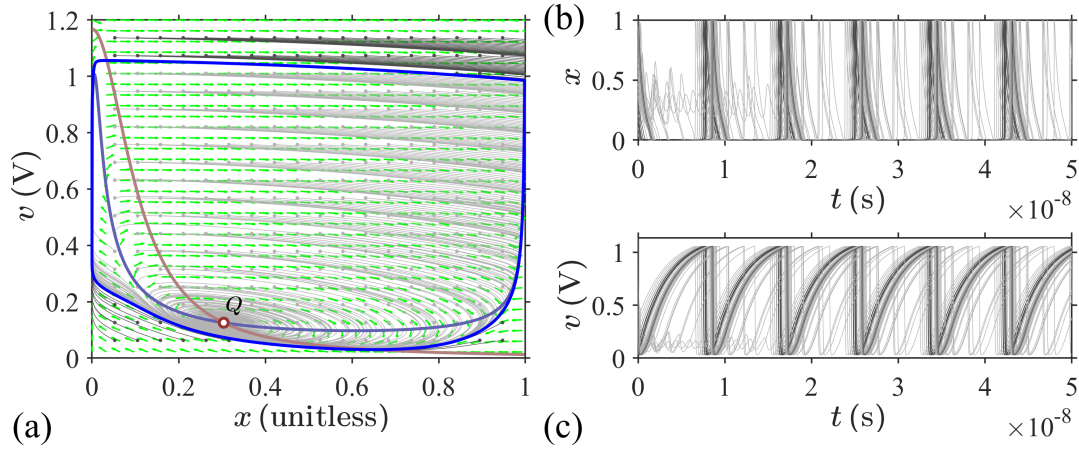


Figure 30: (a) Phase portrait and (b) the corresponding time series $x(t)$, $v(t)$ numerically solved by a MATLAB ode45 solver for the midsize VO₂ Mott memristor PA oscillator with $C_p = 1.0$ pF, $V_{dc} = 1.2$ V and $R_s = 3.4$ k Ω . The system has an unstable fixed point $(x_Q, v_Q) = (0.3040, 0.1256)$ (open circle) at the intersection of the nullclines. A total of 324 orbits are solved with their initial conditions (solid dots) located on a regular grid of (x_0, v_0) , with 18 x_0 levels evenly spaced from 0.05 to 0.95, and 18 v_0 levels from 0.06 V to 1.14 V. Orbits that start from within and outside the limit cycle are light and dark gray colored, respectively. Every $(x(t), v(t))$ trajectory converges onto the same limit cycle (blue orbit) encircling Q , regardless of the initial condition location. The $x(t)$ and $v(t)$ time series show different oscillation phases depending on the initial condition, but all sharing the same period. The mean (standard deviation) of the oscillation period is 8.621 ns (5 ps).

Figure 31(a) and (b) plot the numerically-solved bifurcation diagrams of the 2D Hopf-like bifurcation with R_s as the bifurcation parameter. We noticed that the critical value $R_s^* = 3258.00799 \Omega$ found by numerical calculations is about 3 % different than the analytical value of 3359.5 Ω (see figure 28), possibly due to rounding or truncation errors. Both $x_Q(R_s)$ and $v_Q(R_s)$ are smooth functions of R_s . For $R_s < R_s^*$ (with a difference as small as 10 $\mu\Omega$), there is a single fixed point (x_Q, v_Q) which is a stable spiral according to the linearization analysis. At $R_s \geq R_s^*$, instead of just switching its stability to an unstable spiral (dashed lines), the fixed point bifurcates to a limit cycle. Since a limit cycle is a collection of periodic points $(\tilde{x}(t), \tilde{v}(t))$, we use the maximum and minimum of $\tilde{x}(t)$ and $\tilde{v}(t)$ oscillations to represent their bifurcation branches, and the ranges between maximum and minimum as a measure of the bifurcation amplitude.

This definition is not unique. One can borrow the concepts from celestial mechanics and define the unstable spiral as a focus, then the periapsis (minimum) and apoapsis (maximum) distances between a point in the limit cycle orbit and the focus can also be used to represent the bifurcation amplitude.

A prominent feature about the Mott memristor PA oscillator model is the abrupt appearance or “hard transition” of a stable limit cycle that is completely unfolded over an extremely thin bifurcation parameter interval. The amplitude of a classical Hopf bifurcation for smooth systems grows like $\sqrt{|\mu - \mu_0|}$, i.e., the oscillation amplitude is infinitesimal as $\mu \rightarrow \mu_0$. However, in the present case the oscillations in $\tilde{x}(t)$ and $\tilde{v}(t)$ almost immediately switch to full swing as long as R_s surpasses R_s^* , then their amplitudes remain essentially unchanged as R_s further increases. Abrupt appearance of a stable limit cycle was observed in piecewise-linear systems that have a cut-off or saturation region, e.g., a Wien bridge oscillator [61,62]. For the present Mott memristor model, the fact that the kinetic function diverges toward negative infinity as x approaches 1.0 (see figure 3 inset) tells that there is an *implicit saturation* in the model. A sudden formation of relaxation oscillations, termed “Canard explosion”, has been observed in chemical and biological systems and analyzed thoroughly in the context of Liénard systems, e.g., a van der Pol oscillator [50,51]. The hard transition in relaxation oscillations forms the basis for understanding the all-or-nothing spike firings in biological neurons that can be considered as reaction-diffusion systems of coupled relaxation oscillators, which has been experimentally demonstrated in Mott memristor based neuromorphic neurons (for examples, see figure 3 in [28] and figure 5 in [21]).

Figure 31(c) shows the dependence of the limit cycle oscillation period T_{lc} on R_s . For $R_s < R_s^*$, T_{lc} is zero since there is no oscillation. At $R_s \geq R_s^*$, T_{lc} emerges like a step function and then grows almost linearly with R_s . For comparison, the $R_s C_p$ time constant as a function of R_s is also plotted (gray line). Figure 31(d) shows the ratio between T_{lc} and $R_s C_p$, which remains almost flat in the bifurcation region with an initial overshoot to 2.6 followed by a gradual descent toward 2.4. Generally, the oscillation period of a Hopf bifurcation approaches $2\pi/|\text{Im}(\lambda_{\pm})|$ as $\mu \rightarrow \mu_0$. However, in the present case the calculated $2\pi/|\text{Im}(\lambda_{\pm})|$ curve (green) is about 1.5 ns at $R_s \approx R_s^*$, which is much smaller than $T_{lc} \approx 8.5$ ns.

6.6. 2D supercritical Hopf-like bifurcation by varying C_p

From the tr-det plane analysis of a linearized VO₂ Mott memristor PA oscillator (see figure 24 and text), we know that C_p is possibly also a bifurcation parameter as the system’s fixed point becomes a non-hyperbolic center as C_p passes through a critical value. Now we apply the numerical phase portrait method to examine if C_p is indeed a bifurcation parameter that triggers a 2D local Hopf-like bifurcation.

We numerically solved phase portraits and the corresponding time series for the midsize VO₂ Mott memristor PA oscillator with $R_s = 5.0$ k Ω , $V_{dc} = 1.2$ V, and initial condition $(x_0, v_0) = (0.1, 0.39)$. C_p is varied from 0.1 pF to 1 pF. Figure 32(a) and

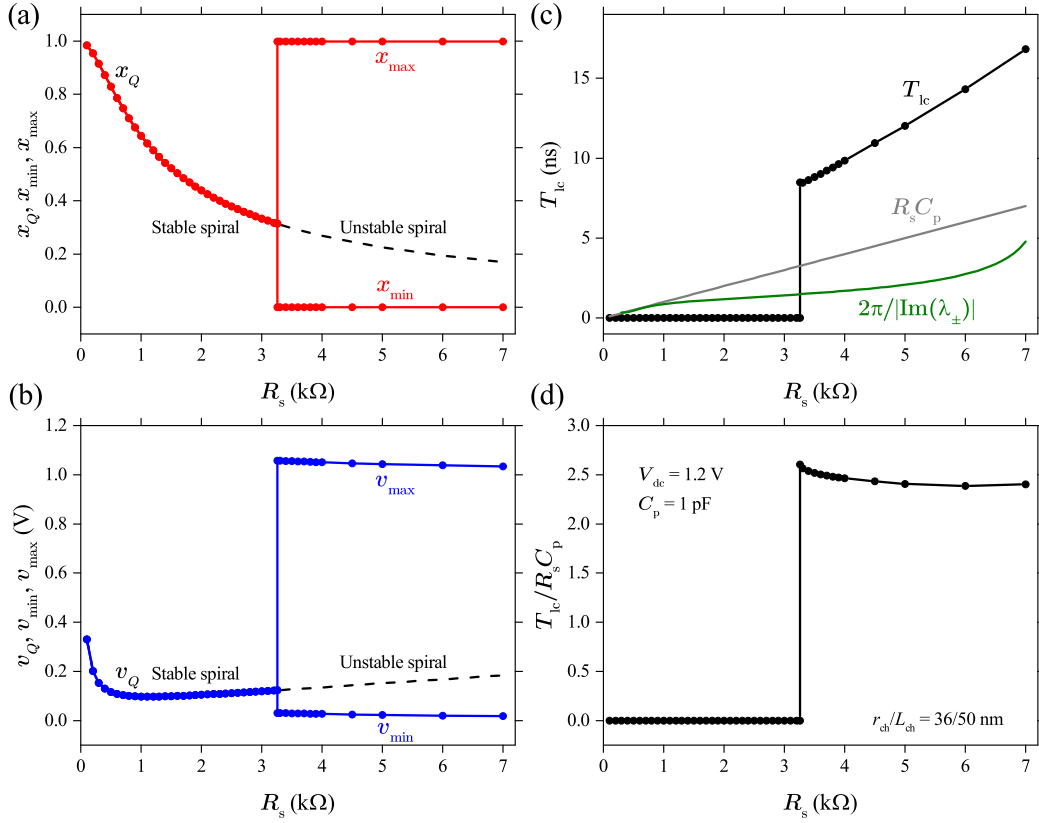


Figure 31: (a) and (b) Numerically-solved bifurcation diagrams of the 2D Hopf-like bifurcation with R_s as the bifurcation parameter for the midsize VO_2 Mott memristor PA oscillator with $C_p = 1.0$ pF and $V_{\text{dc}} = 1.2$ V. The maximum and minimum of $\tilde{x}(t)$ and $\tilde{v}(t)$ limit cycle oscillations are plotted as their bifurcation branches. Dashed lines show the coordinate (x_Q, v_Q) for an unstable spiral at $R_s \geq R_s^*$. (c) R_s dependence of the limit cycle oscillation period T_{lc} (black) plotted together with $R_s C_p$ (gray) and $2\pi/|\text{Im}(\lambda_{\pm})|$ (green). (d) R_s dependence of the ratio between T_{lc} and $R_s C_p$.

32(b) plot the numerically-solved bifurcation diagrams of the 2D Hopf-like bifurcation with C_p as the bifurcation parameter, which reveal a critical value $C_p^* = 0.380448$ pF to trigger the bifurcation. This value is about 0.3 % different than the analytical value of 0.381469 pF (see figure 24), possibly due to rounding or truncation errors. For $C_p < C_p^*$ (with a difference as small as 1 attoFarad), there is a single fixed point (x_Q, v_Q) which is a stable spiral according to the linearization analysis. Both $x_Q(R_s)$ and $v_Q(R_s)$ are independent of C_p as told by the nullcline analysis. At $C_p \geq C_p^*$, instead of just switching its stability to an unstable spiral (dashed lines), the fixed point bifurcates to a limit cycle. Compared with the case of R_s -induced Hopf-like bifurcation with a abrupt unfolding, there is a striking difference for C_p -induced Hopf-like bifurcation. Within a narrow range of C_p (between C_p^* and ~ 0.3832 pF), the bifurcation amplitude grows more gradually and resembles the general prediction of $\sqrt{|\mu - \mu_0|}$, albeit it still has a abrupt switch on, thus the oscillation amplitude is not infinitesimal as $\mu \rightarrow \mu_0$. To illustrate the gradual growth of the 2D Hopf-like bifurcation limit cycle, in figure 33, we plot the

numerically-solved phase portraits $(x(t), v(t))$ at points I, II, III, and IV, corresponding to C_p at 0.380449 pF, 0.382 pF, 0.3832 pF, and 0.38325 pF respectively. One can tell that the gradual growth of Hopf-like bifurcation gives way to abrupt unfolding upon further increase in C_p beyond 0.3832 pF.

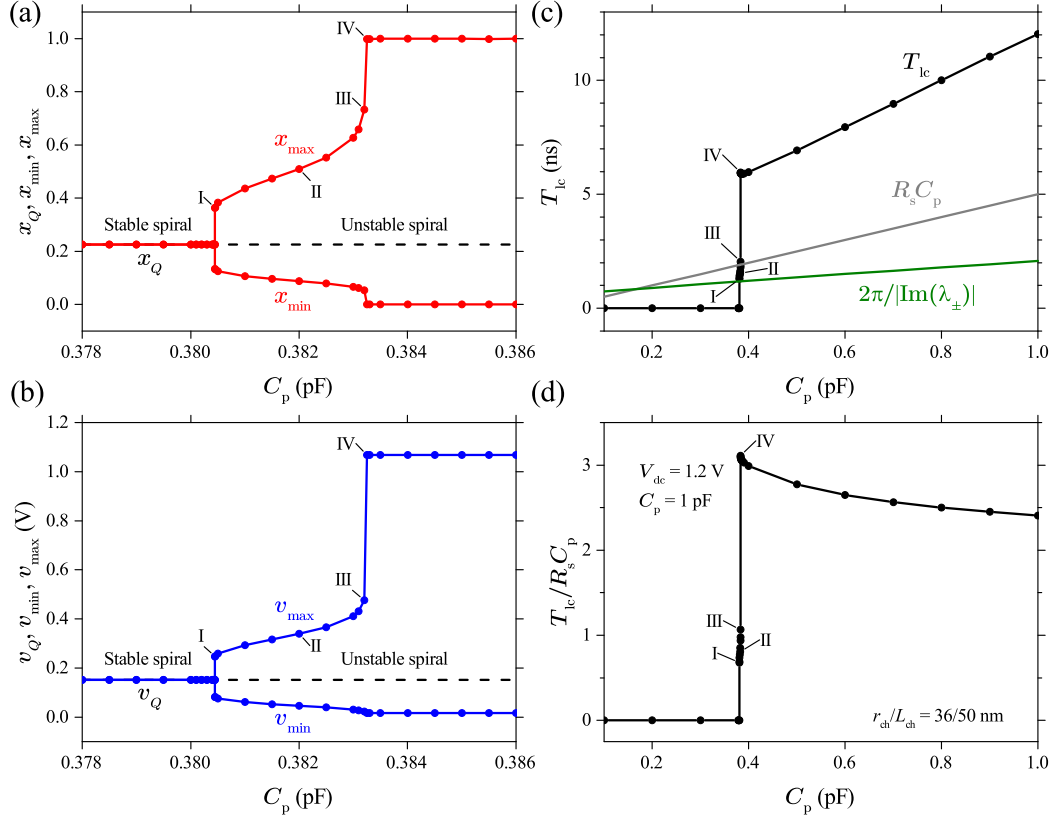


Figure 32: (a) and (b) Numerically-solved bifurcation diagrams of the 2D Hopf-like bifurcation with C_p as the bifurcation parameter for the midsize VO_2 Mott memristor PA oscillator with $R_s = 5.0 \text{ k}\Omega$ and $V_{\text{dc}} = 1.2 \text{ V}$. The maximum and minimum of $\tilde{x}(t)$ and $\tilde{v}(t)$ limit cycle oscillations are plotted as their bifurcation branches. Dashed lines show the coordinate (x_Q, v_Q) for an unstable spiral for C_p larger than $C_p^* = 0.380448 \text{ pF}$. From I to IV, C_p is 0.380449 pF, 0.382 pF, 0.3832 pF, and 0.38325 pF respectively. (c) C_p dependence of the limit cycle oscillation period T_{lc} (black) plotted together with $R_s C_p$ (gray) and $2\pi/|\text{Im}(\lambda_{\pm})|$ (green). (d) C_p dependence of the ratio between T_{lc} and $R_s C_p$.

Figure 32(c) shows the dependence of the limit cycle oscillation period T_{lc} on C_p . At $C_p \approx C_p^*$, the calculated $2\pi/|\text{Im}(\lambda_{\pm})|$ curve (green) is about 1.18 ns, which is very close to $T_{\text{lc}} \approx 1.28 \text{ ns}$ (point I). This confirms that the oscillation period of C_p -induced Hopf-like bifurcation approaches the general prediction of $2\pi/|\text{Im}(\lambda_{\pm})|$ as $\mu \rightarrow \mu_0$. At the upper limit of the gradual growth stage (point III), the oscillation period $T_{\text{lc}} \approx 2.0 \text{ ns}$ is close to the $R_s C_p$ time constant. Then it abruptly increases to 6 ns at point IV as the limit cycle expands to full swing. Figure 32(d) shows the ratio between T_{lc} and $R_s C_p$. In the initial gradual growth stage, this ratio hovers around unity (increases from 0.68 at point I to 1.07 at point III). In the full-swing bifurcation stage, the trend of this

ratio versus the bifurcation parameter is similar to the case of R_s , with a larger initial overshoot to 3.1 followed by a gradual descent toward 2.4.

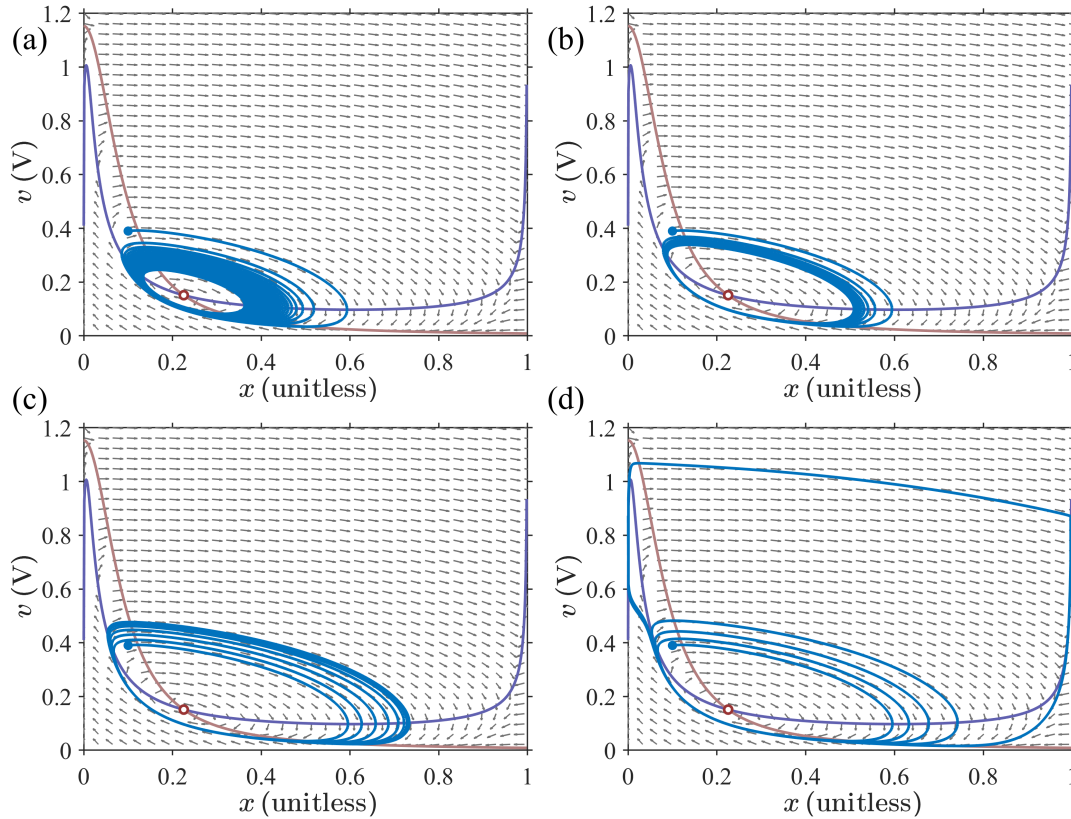


Figure 33: Growth of the 2D Hopf-like bifurcation limit cycle revealed by phase portraits $(x(t), v(t))$ numerically solved for the midsize VO₂ Mott memristor PA oscillator with $R_s = 5.0 \text{ k}\Omega$ and $V_{dc} = 1.2 \text{ V}$. From (a) to (d), the bifurcation parameter C_p is 0.380449 pF, 0.382 pF, 0.3832 pF, and 0.38325 pF respectively, corresponding to points I, II, III, and IV in figure 32. All the solutions start from the same initial condition $(x_0, v_0) = (0.1, 0.39)$.

6.7. 2D supercritical Hopf-like bifurcation by varying V_{dc}

Now we revisit the case of varying V_{dc} as the bifurcation parameter using the numerical phase portrait method. In subsection 6.2, we identified two saddle-node bifurcations using the analytical nullclines and linearized tr-det plane analyses. However, these techniques cannot tell if there exists a Hopf bifurcation or limit cycle around a non-hyperbolic fixed point, such as Q_c^* in figure 27. To clarify, numerical phase portrait calculations are needed.

We numerically solved the phase portraits and the corresponding time series for the midsize VO₂ Mott memristor PA oscillator with $R_s = 3.4 \text{ k}\Omega$, $C_p = 1.0 \text{ pF}$ and initial condition $(x_0, v_0) = (0.1, 0.39)$. Figures 34(a) and 34(b) plot the numerically-solved bifurcation diagrams (solid dots). The calculations reveal a stable limit cycle associated with a supercritical Hopf-like bifurcation if V_{dc} is within a range bounded by the two non-hyperbolic fixed points Q_a^* and Q_c^* , both identified by the analytical methods (see

figure 27). The numerically-determined critical V_{dc} at Q_a^* falls between 1.037 V and 1.038 V, which matches with the analytical result of 1.0379 V. For Q_c^* , it is between 1.248 V and 1.249 V, which is about 2.9 % higher than the analytical result of 1.21355 V. At $V_{dc} \leq 1.037$ V, the system is critically damped. After a fast transient response, $x(t)$ and $v(t)$ return to the stable steady state Q_3 without oscillation. See figure 35(a) for the case of $V_{dc} = 1.037$ V. The system never settles on either one of the unstable Q_1 or Q_2 fixed points (short dashed lines) which are identified by the nullclines. At $V_{dc} \geq 1.249$ V, the system is underdamped, with $x(t)$ and $v(t)$ oscillating with decaying amplitude to the stable steady state Q_1 . See figure 35(d) for the case of $V_{dc} = 1.249$ V. The system has persistent limit cycle oscillations for $1.038 \text{ V} \leq V_{dc} \leq 1.248 \text{ V}$ (see figure 35(b) and (c) for the cases of 1.038 V and 1.248 V, respectively). Similar to the case of varying R_s , there is a abrupt unfolding of the bifurcation amplitude at both Q_a^* and Q_c^* .

Figure 34(c) shows the V_{dc} dependence of the limit cycle oscillation period T_{lc} . As V_{dc} increases through the lower bound Q_a^* of the limit cycle region, the persistent oscillation is initially extremely slow, i.e., T_{lc} significantly overshoots. T_{lc} is 12.6 times as much as the $R_s C_p$ time constant (42.7 ns vs. 3.4 ns), or 25 times as much as $2\pi/|\text{Im}(\lambda_{\pm})|$ (42.7 ns vs. 1.7 ns). As V_{dc} increases, T_{lc} drops super-exponentially. Figure 34(d) shows that near the upper bound Q_c^* of the limit cycle region, the ratio between T_{lc} and $R_s C_p$ descends to 2.34 (7.95 ns vs. 3.4 ns), which is at the same level as the cases of varying R_s (figure 31(d)) or C_p (figure 32(d)).

We end this section with a comparison between experimental characteristics of a VO_2 PA oscillator circuit and SPICE model simulations built upon the model equations (1)–(2), using parameters listed in table 1 and table 2. Details on the implementation of the Mott memristor model in SPICE can be found in the supplementary materials of [43]. Figure 36(d) shows the circuit schematic labeled with the experimental values. The VO_2 nano-crossbar memristor (X_1) has a square junction area of $100 \times 100 \text{ nm}^2$ and oxide film thickness of 100 nm, equivalent to a circular channel radius $r_{ch} = 56 \text{ nm}$ and length $L_{ch} = 100 \text{ nm}$ in the model. $R_e = 370 \text{ } \Omega$ is the measured series resistance of metal electrodes. A parallel shunt resistance of 20 k Ω (not shown) is included in simulations to account for the parasitic insulating-phase conductance present in the VO_2 device. The oscillator output voltage V_{out} is probed by an input channel of an oscilloscope with high input impedance. The current flowing through X_1 is monitored by a second input channel with 50 Ω input impedance. Figure 36(a) compares the measured (red) and the simulated (blue) V_{out} waveforms, both showing the hallmark sawtooth relaxation oscillations. Figure 36(b) compares the measured and simulated current waveforms. In both (a) and (b), we found excellent agreements between measured and simulated results. Figure 36(c) shows the period T_n of 24 consecutive oscillation peaks. Measured oscillation period irregularly fluctuates within a range from 72.4 μs to 83.9 μs , while simulated period is nearly a constant at 76.3 μs . Inset of (c) is the recurrence plot (Poincaré plot or return map) of adjacent oscillation periods (T_n, T_{n+1}), showing the irregularities of experimental relaxation oscillations. The randomness in measured oscillation periods manifests that these nanoscaled Mott memristors are intrinsically

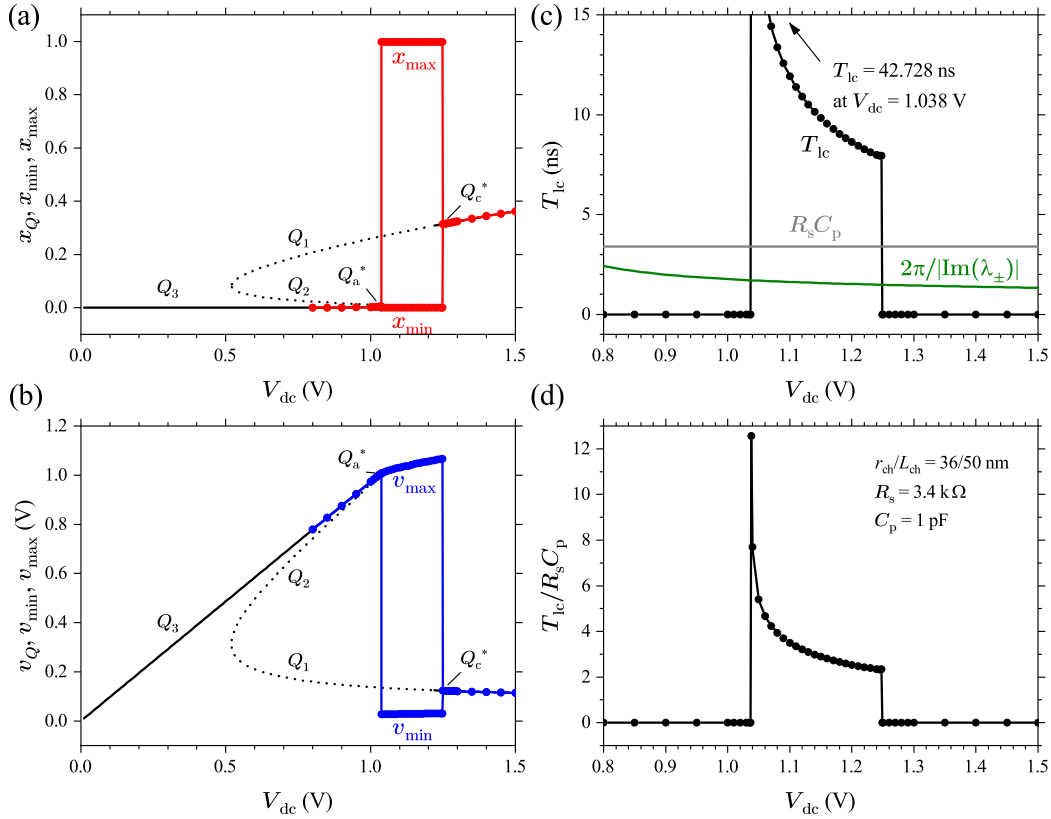


Figure 34: (a) and (b) Numerically-solved bifurcation diagrams of the 2D Hopf-like bifurcations with V_{dc} as the bifurcation parameter for the midsize VO_2 Mott memristor PA oscillator with $R_s = 3.4$ k Ω and $C_p = 1.0$ pF. The maximum and minimum of $\tilde{x}(t)$ and $\tilde{v}(t)$ limit cycle oscillations are plotted as their bifurcation branches. Numerical solutions show that a stable limit cycle exists between the non-hyperbolic fixed points Q_a^* and Q_c^* identified in the analytical nullclines and tr-det plane analyses (see figure 27). At $V_{dc} \leq 1.037$ V, the system settles on the stable fixed point Q_3 instead of the unstable Q_1 or Q_2 found by nullclines (short dashed lines). (c) V_{dc} dependence of the limit cycle oscillation period T_{lc} (black) plotted together with $R_s C_p$ (gray) and $2\pi/|\text{Im}(\lambda_{\pm})|$ (green). Maximum T_{lc} is 42.728 ns at $V_{dc} = 1.038$ V (above the plot area). (d) V_{dc} dependence of the ratio between T_{lc} and $R_s C_p$.

stochastic, which has been demonstrated in stochastic phase-locked firing (skipping) of neuromorphic neurons built with higher-dimensional VO_2 Mott memristor circuits [21].

7. Concluding Remarks

In our view, the implications of locally-active memristors far exceed signal amplification or biological nerve impulse emulation. These scalable nonlinear dynamical elements enable high degree of complexity at the network building block level. From the neuronal dynamics perspective, one can borrow the concept of logical depth and measure the degree of complexity for a neuron model by the approximate number of floating point operations needed to simulate its dynamics for one millisecond duration using a digital

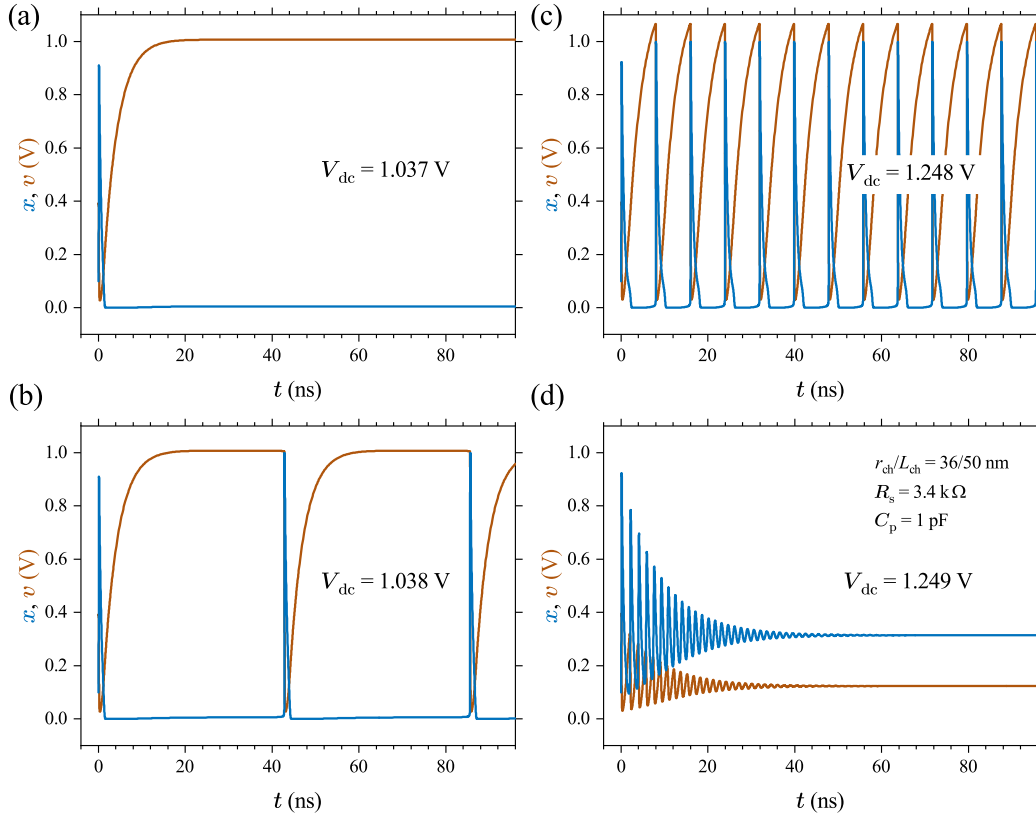


Figure 35: Time series $x(t)$ (blue) and $v(t)$ (brown) numerically solved at V_{dc} close to critical levels for the 2D Hopf-like bifurcations of the midsize VO_2 Mott memristor PA oscillator with $R_s = 3.4 \text{ k}\Omega$ and $C_p = 1.0 \text{ pF}$, showing (a) critical damping at $V_{dc} = 1.037 \text{ V}$, (b) slow limit cycle oscillations at $V_{dc} = 1.038 \text{ V}$, (c) fast limit cycle oscillations at $V_{dc} = 1.248 \text{ V}$ and (d) underdamping at $V_{dc} = 1.249 \text{ V}$. All the solutions start from the same initial condition $(x_0, v_0) = (0.1, 0.39)$.

computer [69]. The biologically plausible HH model takes 1200 FLOP/ms and has the highest degree of complexity among 11 neuron models [70]. The degree of complexity for a Mott memristor neuron is not less than the HH model given that both of them possess similar amount of neurocomputational properties. Architecturally simple yet dynamically rich neuron nodes may allow computationally efficient small adaptive neural networks that are suited for edge computing scenarios which requires real-time causal reasoning based on time series of unlabeled samples. Such use cases turned out to be rather challenging for today's artificial intelligence systems based on machine learning and computationally expensive offline training on the cloud. As the network scales up, more interesting complexity phenomena may emerge at mesoscopic level of neuron populations out of collective interactions of constituent nodes, such as chaotic attractor itinerancy, self-organization, and synchronization. Understanding these phenomena is crucial for replicating the perception and cognition capabilities of the brain.

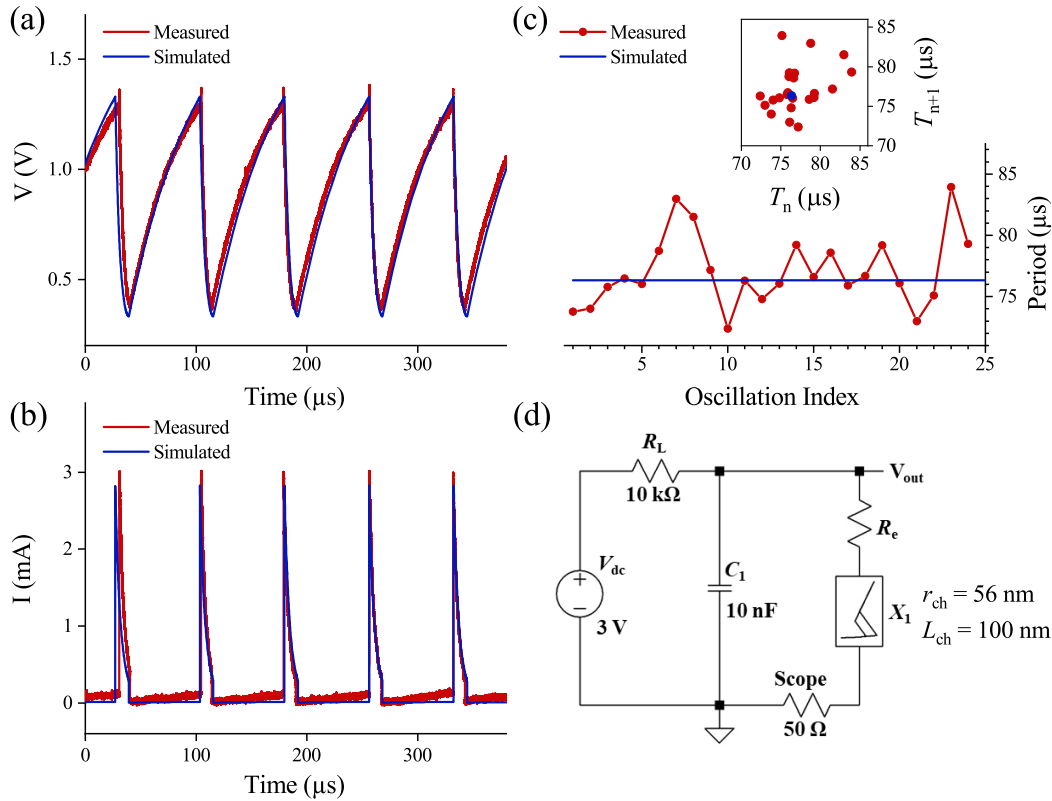


Figure 36: Experimental characteristics of a VO₂ PA oscillator compared with SPICE simulations. (a) Measured (red) and simulated (blue) waveforms of the output voltage (V_{out}). (b) Measured (red) and simulated (blue) waveforms of the current through the memristor (X_1). (c) Measured (red) and simulated oscillation period T_n ($n = 1-24$). Inset: recurrence plot (T_n, T_{n+1}) of the same data. (d) Circuit schematic labeled with the experimental values.

Acknowledgments

This work was funded by HRL Laboratories, LLC. The author is very grateful to the leaders and colleagues of Sensors and Electronics Laboratory for their unwavering support of this research. Kenneth K. Tsang, James M. Chappell, Stephen K. Lam, Xiwei Bai, Jack A. Crowell and Elias A. Flores are acknowledged for their contributions to the experimental data presented in this manuscript.

- [1] Strukov D B, Snider G S, Stewart D R and Williams R S 2008 The missing memristor found *Nature* **453** 80–83
- [2] Dittmann R and Strachan J P 2019 Redox-based memristive devices for new computing paradigm *APL Mater.* **7** 110903
- [3] Kim S, Du C, Sheridan P, Ma W, Choi S and Lu W D 2015 Experimental demonstration of a second-order memristor and its ability to biorealistically implement synaptic plasticity *Nano Lett.* **15** 2203–11
- [4] Wang, Z. et al. 2016 Memristors with diffusive dynamics as synaptic emulators for neuromorphic computing *Nat. Mater.* **16** 101–08
- [5] Covi E, George R, Frascaroli J, Brivio S, Mayr C, Mostafa H, Indiveri G and Spiga S 2018 Spike-driven threshold-based learning with memristive synapses and neuromorphic silicon neurons *J. Phys. D* **51** 344003

- [6] Brivio S, Ly D R B, Vianello E and Spiga S 2021 Non-linear memristive synaptic dynamics for efficient unsupervised learning in spiking neural networks *Front. Neurosci.* **15** 580909
- [7] Chua L O If it's pinched it's a memristor 2014 *Semicond. Sci. Technol.* **29** 104001
- [8] Waser R, Dittmann R, Staikov G and Szot K 2009 Redox-based resistive switching memories – nanoionic mechanisms, prospects, and challenges *Adv. Mater.* **21** 2632–63
- [9] Jeong D S, Thomas R, Katiyar R S, Scott J F, Kohlstedt H, Petraru A and Hwang C S 2012 Emerging memories: resistive switching mechanisms and current status *Rep. Prog. Phys.* **75** 076502
- [10] Ascoli A, Tetzlaff R, Chua L O, Strachan J P and Williams R S 2016 History erase effect in a non-volatile memristor *IEEE Trans. Circuits Syst. I* **63** 389–400
- [11] Pershin Y and Slipko V Bifurcation analysis of a TaO memristor model 2019 *J. Phys. D* **52** 505304
- [12] Yi W, Tsang K K, Lam S K, Bai X, Crowell J A and Flores E A 2019 Active memristor neurons for neuromorphic computing *Int. Electron Devices Meeting* (San Francisco, CA: IEEE)
- [13] Ovshinsky S R 1968 Reversible electrical switching phenomena in disordered structures *Phys. Rev. Lett.* **21** 1450
- [14] Noé P, Verdy A, d'Acapito F, Dory J-B, Bernard M, Navarro G, Jager J-B, Gaudin J and Raty J-Y 2020 Toward ultimate nonvolatile resistive memories: The mechanism behind ovonic threshold switching revealed *Sci. Adv.* **6** eaay2830
- [15] Amsinck C J, Di Spigna N H, Nackashi D P and Franzon P D 2005 Scaling constraints in nanoelectronic random-access memories *Nanotechnology* **16** 2251–60
- [16] Ridley B K 1963 Specific negative resistance in solids *Proc. Phys. Soc.* **82** 954
- [17] Esaki L 1958 New phenomenon in narrow germanium p-n Junctions *Phys. Rev.* **109** 603-04
- [18] Andrews J L, Santos D A, Meyyappan M, Williams R S and Banerjee S 2019 Building brain-inspired logic circuits from dynamically switchable transition-metal oxides *Trends Chem.* **1** 711–26
- [19] Prinz V Ya, Mutilin S V, Yakovkina L V, Gutakovskii A K and Komonov A I 2020 A new approach to the fabrication of VO₂ nanoswitches with ultra-low energy consumption *Nanoscale* **12** 3443–54
- [20] Jager M F, Ott C, Kraus P M, Kaplan C J, Pouse W, Marvel R E, Haglund R F, Neumark D M and Leone S R 2017 Tracking the insulator-to-metal phase transition in VO₂ with few-femtosecond extreme UV transient absorption spectroscopy *P. Natl. Acad. Sci. USA* **114** 9558–63
- [21] Yi W, Tsang K K, Lam S K, Bai X, Crowell J A and Flores E A 2018 Biological plausibility and stochasticity in scalable VO₂ active memristor neurons *Nat. Commun.* **9** 4661
- [22] Yi W and Cruz-Albrecht J 2019 Scalable, energy-efficient, and high-throughput all-memristor neuromorphic processor *DARPA ERI Summit* (Detroit, MI) (https://eri-summit.darpa.mil/docs/ERIPoster_Materials_FRANC_HRL.pdf)
- [23] Farhat N H and Eldefrawy M H 1993 Bifurcating neuron: characterization and dynamics *Proc. SPIE* **1773** 23–35
- [24] Moon K, Cha E, Park J, Gi S, Chu M, Baek K, Lee B, Oh S and Hwang H 2015 High density neuromorphic system with Mo/Pr_{0.7}Ca_{0.3}MnO₃ synapse and NbO₂ IMT oscillator neuron *Int. Electron Devices Meeting* (Washington, DC: IEEE)
- [25] Ignatov M, Ziegler M, Hansen M, Petraru A and Kohlstedt H 2015 A memristive spiking neuron with firing rate coding *Front. Neurosci.* **9** 376
- [26] Stoliar P, Tranchant J, Corraze B, Janod E, Besland M-P, Tesler F, Rozenberg M and Cario L 2017 A leaky-integrate-and-fire neuron analog realized with a Mott insulator *Adv. Funct. Mater.* **27** 1604740
- [27] Wang Z et al. 2018 Fully memristive neural networks for pattern classification with unsupervised learning *Nat. Electron.* **1** 137–45
- [28] Pickett M D, Medeiros-Ribeiro G and Williams R S 2013 A scalable neuristor built with Mott

- memristors *Nat. Mater.* **12** 114–17
- [29] Pickett M D and Williams R S 2013 Phase transitions enable computational universality in neuristor-based cellular automata *Nanotechnology* **24** 384002
- [30] Yi W Active memristor based spiking neuromorphic circuit for motion detection U.S. Patent No. 11,238,335 (1 February 2022)
- [31] Chua L O, Sbitnev V and Kim H 2012 Hodgkin–Huxley axon is made of memristors *Int. J. Bifurcat. Chaos* **22** 1230011
- [32] Crane H D 1960 The neuristor *IRE Trans. Elect. Comput.* **9** 370–71
- [33] Crane H D 1962 Neuristor — A novel device and system concept *Proc. IRE* **50** 2048–60
- [34] Nagumo J, Arimoto S and Yoshizawa S 1962 An active pulse transmission line simulating nerve axon *Proc. IRE* **50** 2061–70
- [35] Ilyashenko Yu 2002 Centennial history of Hilbert’s 16th problem *B Am. Math. Soc.* **39** 301–54
- [36] Perko L 1991 *Differential Equations and Dynamical Systems* (New York, NY: Springer-Verlag)
- [37] Chua L O Local activity is the origin of complexity 2005 *Int. J. Bifurcat. Chaos* **15** 3435–56
- [38] Mannan Z I, Choi H and Kim H 2016 Chua corsage memristor oscillator via Hopf bifurcation *Int. J. Bifurcat. Chaos* **26** 1630009
- [39] Mannan Z I, Choi H, Rajamani V, Kim H and Chua L O 2017 Chua corsage memristor: phase portraits, basin of attraction, and coexisting pinched hysteresis loops *Int. J. Bifurcat. Chaos* **27** 1730011
- [40] Brown T D, Kumar S and Williams R S 2022 Physics-based compact modeling of electro-thermal memristors: Negative differential resistance, local activity, and non-local dynamical bifurcations *Appl. Phys. Rev.* **9** 011308
- [41] Messaris I, Brown T D, Demirkol A S, Ascoli A, Chawa M M A, Williams R S, Tetzlaff R and Chua L O 2021 NbO₂-Mott Memristor: a circuit-theoretic investigation *IEEE T. Circuits-I* **68** 4979–92
- [42] Ascoli A, Demirkol A S, Tetzlaff R, Slesazek S, Mikolajick T and Chua L O 2021 On local activity and edge of chaos in a NaMLab memristor *Front Neurosci.* **15** 651452
- [43] Pickett M D and Williams R S 2012 Sub-100 fJ and sub-nanosecond thermally driven threshold switching in niobium oxide crosspoint nanodevices *Nanotechnology* **23** 215202
- [44] Oh D-W, Ko C, Ramanathan S and Cahill D G 2010 Thermal conductivity and dynamic heat capacity across the metal-insulator transition in thin film VO₂ *Appl. Phys. Lett.* **96** 151906
- [45] Berglund C N and Guggenheim H J 1969 Electronic properties of VO₂ near the semiconductor-metal transition *Phys. Rev.* **185** 1022–33
- [46] Pearson S O and Anson H St G 1921 The Neon tube as a means of producing intermittent currents *Proc. Phys. Soc. London* **34** 204
- [47] Hartman P 1960 A lemma in the theory of structural stability of differential equations *Proc. Amer. Math. Soc.* **11** 610–620
- [48] Grobman D 1959 Homeomorphisms of systems of differential equations *Dokl. Akad., Nauk.* **128** 880–881
- [49] Janninck R F and Whitmore D H 1966 Electrical conductivity and thermoelectric power of niobium dioxide *J. Phys. Chem. Solids* **27** 1183–87
- [50] Krupa M and Szmolyan P 2001 Relaxation oscillation and Canard explosion *J Differ. Equations* **174** 312–68
- [51] Rotstein H G, Coombes S and Gheorghe A M 2012 Canard-like explosion of limit cycles in two-dimensional piecewise-linear models of Fitzhugh-Nagumo type *SIAM J. Appl. Dyn. Syst.* **11** 135–80
- [52] Brown T D, Bohaichuk S M, Islam M, Kumar S, Pop E and Williams R S 2022 Electro-thermal characterization of dynamical VO₂ memristors via local activity modeling *Adv. Mater.* **34** 2205451
- [53] Shashkin Yu A 1991 *Fixed Points* (Mathematical World, vol 2) (Providence, RI: American Mathematical Society)

- [54] Chua L O 2015 Everything you wish to know about memristors but are afraid to ask *Radioengineering* **24** 319–68
- [55] Chua L O 1969 *Introduction to Nonlinear Network Theory* (New York, NY: McGraw-Hill)
- [56] Chua L O 2018 Five non-volatile memristor enigmas solved *Appl. Phys. A* **124** 563
- [57] Marsden J E and McCracken M 1976 *The Hopf Bifurcation and Its Applications* (New York, NY: Springer-Verlag)
- [58] Guckenheimer J and Holmes P 1983 *Nonlinear Oscillations, Dynamical Systems and Bifurcations of Vector Fields* (New York, NY: Springer-Verlag)
- [59] Hong B 2022 Phase Plane and Slope Field apps (<https://github.com/MathWorks-Teaching-Resources/Phase-Plane-and-Slope-Field/releases/tag/v1.1.1>)
- [60] Van Der Pol B and Van Der Mark J 1928 The heartbeat considered as a relaxation oscillator, and an electrical model of the heart *Phil. Mag.* **6** suppl. 763-75
- [61] Kriegsmann G A 1987 The rapid bifurcation of the Wien bridge oscillator *IEEE Trans. Circuits Syst.* **34** 1093–96
- [62] Freire E, Ponce E and Ros J 1999 Limit cycle bifurcation from center in symmetric piecewise-linear systems *Int. J. Bifurcation Chaos* **9** 895–907
- [63] Cole K 1941 Rectification and inductance in the giant squid axon *J. Gen. Physiol.* **25** 29–51
- [64] Liang Y, Zhu Q, Wang G, Nath S K, Iu H H-C, Nandi S K and Elliman R G 2022 Universal dynamics analysis of locally-active memristors and its applications *IEEE T. Circuits-I* **69** 1278–90
- [65] Hastings S P 1974 The existence of periodic solutions to Nagumo’s equation *Quart J. Math. Oxford Ser.* **25** 369-378
- [66] Troy, W. C. 1978 The bifurcation of periodic solutions in the Hodgkin-Huxley equations *Q. Appl. Math.* **36** 73-83
- [67] Rinzel J and Miller R N 1980 Numerical calculations of stable and unstable periodic solutions to the Hodgkin-Huxley equations *Math. Biosci.* **49** 27-59
- [68] Dogaru R and Chua L O 1998 Edge of chaos and local activity domain of FitzHugh-Nagumo equation *Int. J. Bifurcat. Chaos* **8** 211–57
- [69] Bennett C H 1988 Logical depth and physical complexity *The Universal Turing Machine, A Half-Century Survey* ed R Herken (New York, NY: Oxford University Press) 227–57
- [70] Izhikevich E M 2004 Which model to use for cortical spiking neurons? *IEEE Trans. Neural Netw.* **15** 1063–70